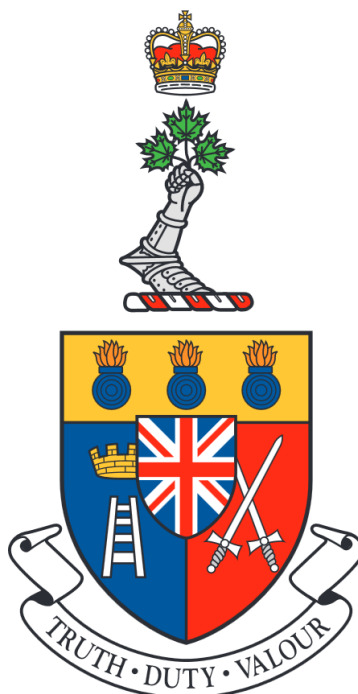


**Development and Implementation of The Royal Military College of
Canada's Geotechnical Beam Centrifuge for Physical Modelling**

**Développement et mise en œuvre de la centrifugeuse géotechnique du
Collège militaire royal du Canada pour la modélisation physique**



VÉRITÉ • DEVOIR • VAILLANCE

A Thesis Submitted to the Department of Graduate Studies
of the Royal Military College of Canada
by

John Samuel Kingswood
Captain

In Partial Fulfillment of the Requirements for the Degree of
Master of Applied Science

May, 2017

© This thesis may be used within the Department of National Defence but copyright for open
publication remains the property of the author.

Dedication

For William

Acknowledgements

Firstly, I would like to thank RMCC's Civil Engineering Department, all of its faculty and staff who provided their expertise, time, and resources to ensure the success of this research. I would specifically like to thank Dr. Greg Siemens for his constant support, guidance, and willingness to share his knowledge and experience, and Mr. Stephen LaPorte for his work with the centrifuge and many hours of help with its development and testing. I would also like to acknowledge the contributions of the Department of National Defence, specifically 1 Engineer Support Unit for allowing me to undertake this research, and the *Natural Sciences and Engineering Research Council* of Canada for providing funding.

I would also like to thank Thomas Broadbent & Sons Ltd., and their staff, Mr. Neil Baker and Mr. Mick Mulligan for their wonderful machine and my introduction to the ability to manipulate the fabric of space and time with it (as well as their ongoing technical support for it).

To my wife, Nadia, and my children, William, Rose, Clara, and Ransom, I want to apologise for my frequent absences as I parented the centrifuge through overnight tests and the numerous late nights spent plotting data and writing. But mostly I thank you for all of your faithful prayer for me, and your unfaltering encouragement throughout this research.

Lastly, I want to thank God, my Father, our Lord Jesus Christ, and his Holy Spirit, for providing me this opportunity, support through the people around me, and grace and ability to complete this work.

*non nobis Domine
non nobis
sed nomini
tuo da gloriam*

Abstract

The Royal Military College of Canada has recently acquired a 1.5m-diameter, 6 G-ton geotechnical beam centrifuge. Geotechnical centrifuges apply an elevated gravity field to permit physical modelling of geo-structures at significantly reduced spatial and temporal scales. In this thesis both confirmatory testing for development of the centrifuge is conducted and behaviour of expansive soils subjected to wetting-drying is examined. First the methodology, equipment, and apparatuses for the centrifuge are developed for use in physical modelling exercises. Two verification test programs are conducted, a slope stability model and a strip footing constructed on a remolded clay soil are modelled, varying scale, shear strength, and model geometry. Correlation between behaviour of the physical models at different scales and agreement with analytical solutions is shown. These results demonstrate the application of the centrifuge and the methods used to produce accurate modelling of geotechnical structures at various scales and provides a basis of theory and methodology for further research of more complex geotechnical problems. Secondly, expansive soils are a challenging engineering material that cause severe damage to light infrastructure when subjected to seasonal wetting and drying cycles. A paved road structure model is constructed in expansive soil and subjected to cyclic infiltration and evaporation. The results of wetting-drying cycles agree with theoretical failure mechanisms for pavements and published field data of similar structures and conditions. The strains observed through the soil profile, which are observable with centrifuge modelling, explain the behaviour of the surface predicted by the theory and observed in field studies, and replicated in the models. The results provide insight into the mechanism producing road failure and the impact of modifications to road designs. The success of centrifuge modelling of idealized and complex geotechnical structures and mechanisms is established, providing a valuable tool for teaching and research at the Royal Military College of Canada.

Résumé

Le Collège militaire royal du Canada a récemment acquis une centrifugeuse à faisceau géotechnique de 1,5 m de diamètre et 6 Gt. Les centrifugeuses géotechniques appliquent un champ de gravité élevé pour permettre la modélisation physique des géo-structures à des échelles spatiales et temporelles significativement réduites. Dans cette étude, des tests de confirmation du développement de la centrifugeuse sont effectués et le comportement des sols expansibles soumis à un séchage par voie humide est examiné. Tout d'abord, la méthodologie, l'équipement et les appareils de la centrifugeuse sont conçus pour être utilisés dans des exercices de modélisation physique. Deux programmes de test de vérification sont menés, un modèle de stabilité de pente et une semelle construite sur un sol d'argile remodelé sont modélisés, en variant l'échelle, la résistance au cisaillement et la géométrie du modèle. La corrélation entre le comportement des modèles physiques à différentes échelles et l'accord avec des solutions analytiques sont présentés. Ces résultats démontrent l'application de la centrifugeuse et les méthodes utilisées pour produire une modélisation précise des structures géotechniques à différentes échelles et fournit une base de théorie et de méthodologie pour une recherche approfondie de problèmes géotechniques plus complexes. Deuxièmement, les sols expansifs sont un matériau d'ingénierie difficile qui cause de graves dommages aux infrastructures légères lorsqu'ils sont soumis à des cycles environnementaux. Un modèle de structure de route pavée est construit dans un sol expansif et soumis à une infiltration cyclique et à une évaporation. Les résultats des cycles de mouillage-séchage concordent avec les mécanismes d'échec théorique pour les chaussées et les données de terrain publiées sur de structures et conditions similaires. Les efforts observés à travers le profil du sol qui sont observables par modélisation par centrifugation expliquent le comportement de la surface prédite par la théorie et observées dans les études sur le terrain et reproduites dans les modèles. Les résultats donnent un aperçu du mécanisme produisant la dégradation de la route et de l'impact de la modification de la conception. Le succès de la modélisation par centrifugation de structures et de mécanismes géotechniques idéalisés et complexes est établi, ce qui constitue un outil précieux pour l'enseignement et la recherche au Collège militaire royal du Canada.

Co-Authorship

The thesis “Development and Implementation of The Royal Military College of Canada’s Geotechnical Beam Centrifuge for Physical Modelling” is the product of research conducted by the author, John Samuel Kingswood. While scientific and editorial comments were made by Greg Siemens, the written content is solely that of the author. In-kind contribution in the form of test data has resulted in a conference publication that is acknowledged in the references section.

Table of Contents

| | |
|--|------|
| Dedication | ii |
| Acknowledgements | iii |
| Abstract | iv |
| Co-Authorship..... | vi |
| List of Figures | ix |
| List of Tables | xii |
| List of Symbols, Abbreviations, and Acronyms | xiii |
| Chapter 1 Introduction | 1 |
| Chapter 2 Geotechnical Centrifuge Development | 3 |
| 2.1 Introduction..... | 3 |
| 2.2 The Royal Military College of Canada Geotechnical Centrifuge | 6 |
| 2.2.1 Scaling Laws | 8 |
| 2.2.2 Gravity Field Considerations | 9 |
| 2.2.3 Balancing the Centrifuge..... | 10 |
| 2.2.4 Mechanical Boundary Conditions | 11 |
| 2.2.5 Data Acquisition an Analysis..... | 14 |
| 2.2.5.1 Onboard Computer..... | 14 |
| 2.2.5.2 Digital Cameras..... | 14 |
| 2.2.5.3 Particle Image Velocimetry..... | 15 |
| 2.3 Verification Exercises | 16 |
| 2.3.1 Undrained Slope Stability | 16 |
| 2.3.1.1 Undrained Slope Stability Modelling of Models Theory | 17 |
| 2.3.1.2 Materials and Methodology | 19 |
| 2.3.1.3 Results..... | 22 |
| 2.3.2 Undrained Bearing Capacity | 29 |
| 2.3.2.1 Undrained Bearing Capacity Modelling of Models Theory..... | 29 |
| 2.3.2.2 Methodology and Materials | 30 |
| 2.3.2.3 Results..... | 32 |
| 2.4 Summary | 38 |

| | |
|---|----|
| Chapter 3 Physical Modelling of Wetting-Drying Cycle Applied to Infrastructure Constructed in Expansive Soils | 39 |
| 3.1 Introduction | 39 |
| 3.2 Theory | 2 |
| 3.2.1 Centrifuge Scaling..... | 2 |
| 3.3 Material, Testing, and Data Analysis Methodology | 5 |
| 3.3.1 Model Design | 5 |
| 3.3.2 Soil Characterization | 7 |
| 3.3.3 Test Soil Preparation | 10 |
| 3.3.4 Model Construction..... | 11 |
| 3.3.5 Centrifuge Cradle Setup..... | 14 |
| 3.3.6 Testing Cycle | 19 |
| 3.3.7 Particle Image Velocimetry Analysis..... | 21 |
| 3.4 Results..... | 25 |
| 3.4.1 Test 1 Road Model Results | 26 |
| 3.4.2 Test 2 Road Model Results | 34 |
| 3.5 Discussion | 42 |
| 3.5.1 Surface Displacement..... | 42 |
| 3.5.2 Soil Profile Strains | 45 |
| 3.6 Summary | 48 |
| Chapter 4 Conclusion..... | 49 |
| References..... | 51 |
| Appendices..... | 55 |
| Appendix A Cradle Base Suction and Pressure Control | 56 |
| Appendix B Atmospheric Control and Monitoring..... | 59 |
| Appendix C Particle Image Velocimetry RG Analysis..... | 61 |
| Appendix D Shrinkage Curve for Soil Mixture | 68 |
| Appendix E Verification of physical modelling with a geotechnical centrifuge using physical models of slope stability and bearing capacity. <i>In: Proceedings of the 69th Annual Canadian Geotechnical Conference.</i> | 69 |

List of Figures

| | |
|---|----|
| Figure 1 Effects of Gravity Field as a Function of Radius (Schofield, 1970)..... | 4 |
| Figure 2 Image (A) and Diagram (B) of RMCC's Geotechnical Beam Centrifuge (Broadbent, 2015) | 7 |
| Figure 3 Scaling Relationships as a Function of N (Madabhushi, 2015)..... | 8 |
| Figure 4 Gravity Field as a Result of Changes in Radius | 10 |
| Figure 5 Effect of Base Friction Insert Plates from (A) Failure Plane without Plates, to (B) Failure Plane with Plates..... | 13 |
| Figure 6 3D Printed Frictional Plate | 14 |
| Figure 7 GoPro HERO 4 and ELP Webcam on Mounted on Cradle | 15 |
| Figure 8 Taylor Chart (Taylor, 1948) | 18 |
| Figure 9 Relationship between Water Content and Undrained Shear Strength with Location of Actual Test Parameters | 20 |
| Figure 10 (A) Slope Geometry within the Centrifuge Cradle for Both Slopes and (B) Image of a Typical 150mm Slope | 21 |
| Figure 11 Results from a Typical 150 mm Undrained Slope Test Showing: (A) Image of Model before Failure, (B) Image of Model after Failure, (C) N_{model} versus Time, and (D) geoPIV Vector Displacement Results | 24 |
| Figure 12 Stable and Failure Patch Displacement vs Time with Location of Failure..... | 25 |
| Figure 13 Slope Stability Modelling of Models Correlation..... | 27 |
| Figure 14 Observed Slope Stability Correlation with Theoretical Prediction..... | 28 |
| Figure 15 (A) Strip Footing Geometry within Centrifuge Cradle for Both Strip Footings and (B) Image of Typical 30mm Strip Footing | 31 |
| Figure 16 Results from a Typical 60 mm Undrained Slope Test Showing: (A) Image of Model before Failure, (B) Image of Model after Failure, (C) N_{model} versus Time, and (D) geoPIV Vector Displacement Results | 33 |
| Figure 17 Patch Displacement vs Time with Location of Failure..... | 34 |
| Figure 18 Bearing Capacity Modelling of Models Correlation | 36 |
| Figure 19 Observed Bearing Capacity Correlation with Theoretical Prediction | 37 |

| | |
|---|----|
| Figure 20 Seasonal Wetting and Drying Producing (A) Swelling and (B) Shrinking Behaviour in Expansive Clay with the Relationship between Matric Suction and Void Ratio Shown with Consideration of Compressive Stresses | 42 |
| Figure 21 Effect of Infiltration on Suction Profile | 0 |
| Figure 22 Failure Mechanism for Paved Road in Expansive Soil (after Zornberg et al., 2009)1 | |
| Figure 23 Road Damage Caused by Expansive Soil (Coating Industry News, 2016) | 1 |
| Figure 24 Stresses within Soil Profile in the Centrifuge | 3 |
| Figure 25 Prototype (A) and Model Design (B) | 6 |
| Figure 26 Typical Expansive Soil (black) (Fredlund et al., 2012) and 90% Kaolin and 10% Bentonite Soil Mixture (red) Properties | 7 |
| Figure 27 Proctor Compaction Curve for Expansive Soil (90% Kaolin and 10% Bentonite) .. | 9 |
| Figure 28 Grain Size Distribution for Expansive Soil (90% Kaolin and 10% Bentonite) | 9 |
| Figure 29 Mechanically Mixed Soil..... | 11 |
| Figure 30 Model Preparation | 12 |
| Figure 31 Typical Texture for Image Analysis | 13 |
| Figure 32 Model Construction | 13 |
| Figure 33 Impervious Road Surfacing with Paraffin Wax..... | 14 |
| Figure 34 Filter Stone Base..... | 15 |
| Figure 35 Air Control Apparatus on Centrifuge Cradle..... | 16 |
| Figure 36 Constructed Road Model in Centrifuge Cradle | 17 |
| Figure 37 Camera Layout..... | 18 |
| Figure 38 Atmospheric Control Apparatus | 19 |
| Figure 39 Typical RH for Wetting and Drying Cycles | 20 |
| Figure 40 Typical PIV Analysis Mesh (Modified Road) | 22 |
| Figure 41 Typical Correlation Coefficients Values with Patch Displacement Data | 24 |
| Figure 42 Test 1 Road – Total Suction Applied to Surface | 27 |
| Figure 43 Test 1 Road – Average Displacement for Top Patches Below the Far Field..... | 27 |
| Figure 44 Test 1 Road - Vertical Displacement of Model Surface at the End of Each Cycle (Swelling/Shrinking)..... | 29 |
| Figure 45 Test 1 Road – Surface and Zones with Image Dimensions | 30 |
| Figure 46 Test 1 Road – Swelling Strains for Cycles 1 (A), 2(B), and 3(C) | 31 |

| | |
|--|----|
| Figure 47 Test 1 Road – Shrinking Strains for Cycles 1 (A), 2(B), and 3(C)..... | 32 |
| Figure 48 Test 1 Road – Vertical Strains through Expansive Zone for Representative Profile | 33 |
| Figure 49 Test 1 Road – Water Contents with Depth at End of Drying Cycle 3..... | 34 |
| Figure 50 Test 2 Road – Total Suction Applied to Surface | 35 |
| Figure 51 Test 2 Road – Average Displacement of Top Patches Below the Far Field..... | 35 |
| Figure 52 Test 2 Road - Vertical Displacement of Model Surface at the End of Each Cycle (Swelling/Shrinking)..... | 36 |
| Figure 53 Test 2 Road – Surface and Zones with Image Dimensions | 37 |
| Figure 54 Test 2 Road – Swelling Strains for Cycles 1 (A), 2(B), and 3(C) | 38 |
| Figure 55 Test 2 Road – Shrinking Strains for Cycles 1 (A), 2(B), and 3(C)..... | 39 |
| Figure 56 Test 2 Road – Vertical Strains through Expansive Zone for Representative Profile | 40 |
| Figure 57 Test 2 Road – Water Contents with Depth at End of Drying Cycle 3 | 41 |
| Figure 58 Test 1 Road - Vertical Displacement of Pavement (Swelling/Shrinking) | 44 |
| Figure 59 Test 2 Road - Vertical Displacement of Pavement (Swelling/Shrinking) | 44 |
| Figure 60 Test 1 Road (Left) and Test 2 Road (Right) - Vertical Displacement of Pavement (Swelling/Shrinking) with Typical Case Study Values (Roodi et al., 2016) | 45 |
| Figure 61 Test 1 Road Swelling (A) and Shrinking (B) and Test 2 Road Swelling (C) and Shrinking (D) - Limit of Strains below Road Surface | 47 |
| Figure 62 (A) Standpipe and (B) Air Control Apparatus..... | 57 |
| Figure 63 Water Controlled Capillary Rise at (A) 10g and (B) 40g | 58 |
| Figure 64 Atmospheric Control Table with RH and Temperature Sensor in Cradle | 60 |
| Figure 65 Collection Tray Arrangement | 60 |
| Figure 66 Control Points | 62 |
| Figure 67 Region of Interest Selected by User with Control Points and Patch Centers | 63 |
| Figure 68 Region of Interest .jpg File Produced by the Subroutine..... | 64 |
| Figure 69 Typical geoLAUNCH_RG File | 65 |
| Figure 70 Shrinkage Curve for Soil Mixture | 68 |

List of Tables

| | |
|---|----|
| Table 1 Centrifuge Operating parameters (Broadbent, 2015)..... | 9 |
| Table 2 Summary of Slope Stability Tests Results | 25 |
| Table 3 Slope Stability Testing Parameters for 40° Slope | 28 |
| Table 4 Summary of Strip Footing Bearing Capacity Test Results | 34 |
| Table 5 Summary of Bearing Capacity Test Results | 37 |
| Table 6 Comparison of Stresses at Geometric Control Points in Model at 40g and Scaled Prototype | 4 |
| Table 7 Expansive Soil (90% Kaolin and 10% Bentonite) Material Properties Compared with Typical Values | 8 |
| Table 8 PIV Displacement Analysis (Leapfrog Analysis with 50 Iterations ¹)..... | 23 |
| Table 9 Testing Cycles for Test Serials | 25 |

List of Symbols, Abbreviations, and Acronyms

| | |
|-----------------------------|--|
| c | Undrained shear strength |
| g | Acceleration of gravity (9.81 m/s ²) |
| i | Slope angle |
| m | Mass of footing |
| m ₂ ^s | Coefficients change in suction |
| q | Bearing capacity |
| Q _{applied} | Applied foundation stress |
| r | Radius |
| u _a | Pore air pressure |
| u _w | Pore water pressure |
| w | Gravimetric water content |
| z | Depth |
| A | Area |
| B | Width of footing |
| CH | Clay of high plasticity |
| ℄ | Centerline of road |
| D _f | Depth of footing |
| H | Height of slope |
| LL | Liquid limit |
| N | Number of times the acceleration of gravity |
| N _c | Bearing capacity shear strength factor |

| | |
|----------------------|---------------------------------------|
| N_{failure} | Applied N at which failure occurs |
| N_o | Stability number |
| N_q | Bearing capacity factor |
| N_c | Bearing capacity hear strength factor |
| PI | Plasticity index (LL-PL) |
| PL | Plastic limit |
| RH | Relative humidity |
| T | Temperature |
| V | Volume of soil |
| V_o | Initial volume |
| V_v | Volume of voids |
| USCS | Unified Soil Classification System |
| ϵ_v | Volumetric strain |
| $\dot{\theta}$ | Angular velocity |
| ρ | Density |
| σ | Stress |
| ϕ_d | Friction angle |
| γ | Unit weight of soil |

| | |
|------|----------------------------------|
| PIV | Particle Image Velocimetry |
| PLA | Polylactic Acid |
| RMCC | Royal Military College of Canada |
| RoI | Region of Interest |
| RPM | Rotation per Minute |
| .stl | StereoLithography file format |

Chapter 1

Introduction

Geotechnical engineering is a field that affects the lives of every person. It is critical to large and small vertical construction, horizontal transportation and utilities corridors, and every gradient of structure in-between. The materials foisted upon geotechnical engineers by the environments they work in are as varied as the projects they affect. Soil composition, history, and current phase conditions combine to produce a myriad of effects, such as sensitivity, loss of strength under certain conditions, and expansive behaviour, often unlooked for and frequently undesired. Also working against the geotechnical engineer are the unique peculiarities of each individual geotechnical problem and the specialization the subsequent design solutions require. Rarely are any two geotechnical designs the same. This presents not only challenges in answering the problems in geotechnical engineering but also in understanding and defining them.

The necessities of constant improvement and enlarged understanding of the challenges presented by the materials and their responses to the work of engineers cultivates the conception and development of new tools and methods to achieve these ends. Geotechnical engineers have produced several tools to achieve this. The first and most easily employed tool is the battery of lab tests that have been developed to describe and quantify the physical properties of soils. These, coupled with the pioneering work of men like Karl von Terzaghi and Donald W. Taylor among many others in forging general descriptive theories and models, help geotechnical engineers interpret and predict behaviour of soil. Numerical modelling of soil mechanics predicated on the previously mentioned models further expands not only the understanding but also the ease of modelling more complex structures; adding another tool to the array available to geotechnical engineers. However, these methods require another tool in their support. Physical modelling of geotechnical structures can be used to validate the theories and confirm the numerical models that are being employed for a large range of soils and their associated properties. Small and full scale testing of soil structures and their discrete elements compliments the previously mentioned tools to anchor the theories and models to observed soil behaviour. Two hindrances to the employment of these methods is that discrete small scale testing may artificially prevent an integrated response from the soil and structure being studied and large scale testing is expensive, slow, and labour intensive. The discovery of centrifuge testing as an elegant tool for geotechnical engineers answers the need for rapid, accessible, integrated modelling of complex geotechnical problems.

Geotechnical centrifuge modelling of the problems and structures of soil mechanics provides a tool that can quickly and repeatedly load, and even destroy a geotechnical structure multiple times before the prototype is ever built. By applying a greater effective force of gravity to a geotechnical model through the constant application of rotationally generated acceleration, the stresses applied to the soil and therefore its behaviours can be replicated for much larger scales (Roscoe, 1970). This allows the description of large, slowly responsive structures with small models whose behaviour can be observed in much shorter

periods and in much greater detail. The use of this technique is ideally suited for teaching and research as well as engineering design because of these benefits and the high degree of observation that it permits. The civil engineering department at the Royal Military College of Canada (RMCC) recognized the asset a geotechnical centrifuge is to research and education related to soil behaviour and so has acquired a geotechnical centrifuge for these applications.

This thesis is an article based thesis and presents two papers describing the development of the centrifuge and its implementation in further research. The first paper (Chapter 2) describes the preliminary testing conducted with the centrifuge. Although the use of geotechnical centrifuge testing is decades old, the constant development of new techniques, equipment, and application necessitate that RMCC develop methodology and equipment for its centrifuge as well as verifying its use. The modelling of two types of structures, a soil slope and a strip footing, both constructed at two different scales allows for the evaluation of the methods and scaling theories application in the centrifuge. This endeavor provides a solid foundation upon which future research can be built with confidence in its results.

The second paper (Chapter 3) describes the application of the methods and confirmation established by the first paper. Expansive soils are a global natural phenomenon, embodying the unexpected and unlooked for behaviour that frequently frustrates, damages, and destroys the work of geotechnical engineers. These clay soils, which respond dramatically to infiltration and evaporation, produce severe effects on geotechnical structures. Modelling of the behaviour of these soils requires accurate application of stresses to the model and seasonal wetting and drying that are representative of those applied to actual constructions affected by them. These criteria need to be achieved while minimizing the incidental effects common to physical modelling as well as those unique to centrifuge testing. The expansive soil model of road behaviour is evaluated against accepted theoretical mechanisms and observed data from case studies. A physical model of simple road structures constructed on a designed swelling soil subgrade demonstrates the broad utility of RMCC's geotechnical centrifuge and its benefit to the College as a unique and valuable tool.

Chapter 2

Geotechnical Centrifuge Development

2.1 Introduction

Geotechnical structures are frequently large, respond to loading and climatic and seasonal weather effects over long periods of time, and are often unique designs, whether due to the multitude of possible material properties, geometry, desired application and engineering effects, or a complex interaction of all of these individual characteristics. In response to these design difficulties, geotechnical engineering practice have employed three tools, or types of tools, that can be used to attempt a better understanding of the behaviour of geotechnical structures. These tools are: full scale testing and case studies (eg. Roodi et al. 2016, Zornberg et al., 2009), numerical modelling (eg. Ito et al. 2014), and physical modelling, all of which are supported by element or laboratory testing (eg. Roscoe, 1970, Take et al., 2002). Full scale testing, while seemingly the ideal candidate to understand how a structure behaves, is expensive and time consuming for each individual structure, loading, and weather conditions (Lyndon et al., 1970). Case studies similarly take years to produce usable data and the cost and effort of long-term monitoring makes the availability of such data rare (Ito et al., 2014) and limit the data gathered to a small number of points, in poorly controlled environments (Take et al. 2002). Numerical methods for modelling geotechnical structures have been produced in order to answer some of these obstacles and can be used at significantly lesser cost. However, they requires input, often from field testing (Ito et al. 2014), in order to be confirmed (Roscoe, 1970). Scaled physical modelling has the advantage of being rapid and cost effective, modelling the behaviour of geotechnical structures in a matter of hours or days rather than months or years, providing greater control over stress history, materials, and weather conditions, and giving access to great depth of data provided through real observation of the structure's behaviour. These characteristics make integrated physical modelling of complex geotechnical materials, structures, and mechanisms an ideal tool for provision of data.

In order to employ such a useful tool, physical modelling requires the correct and scaled application of force, behaviour of materials, and gross structural mechanisms (Roscoe, 1970). In order for physical modelling to achieve these requirements the correct forces must be applied at geometric points within the model as those present at the same points in the prototype (Roscoe, 1970). A geotechnical centrifuge allows for examination of reduced scale geotechnical structures at elevated g-levels and subsequently elevated forces, either from self-weight of the soil or applied by some structure or mechanism (Madabhushi, 2015, Garnier et al., 2007). In his Rankine lecture, Roscoe (1970), discussed the need for centrifuge testing as a critical tool for advancement of the knowledge in the field of geotechnical engineering because for any structure in which self-weight and the resultant stresses play a significant role (which he notes as comprehending nearly the entire discipline of geotechnical engineering) the masses involved must be accurately scaled through an increase in gravity. Geotechnical modelling is unique in its ability to apply these forces to geotechnical materials across the dimensions of a physical model. Ten years later, in Schofield's Rankin lecture (Schofield, 1980), he summarized the advances and benefits of geotechnical modelling of

material behaviour, seepage and diffusion rates, and modelling of prototype structures that Cambridge University had been able to achieve in its first decade of physical modelling with its geotechnical centrifuge. One of the points Schofield makes is the benefit of the use of modelling models to verify scaling laws in contrast to the more advanced problem of modelling a real-world prototype. A second item presented as crucial to the understanding and application of centrifuge modelling techniques are the incidental issues of variations in the gravity field across the height of a model relative to its radius (Figure 1) and the Coriolis Effect that are produced in centrifuge testing. Figure 1 shows the relationship between vertical effective stress as a result of the applied forces of gravity (N_g) and the depth for a prototype and a model. In the prototype, effective stress increases linearly with depth due to the overburden material. In a centrifuge model gravity varies with radial distance (Equation 1) and therefore, effective stress increases non-linearly in a concave up shape. Often analyses equate gravity in the model and prototype at a depth of $2/3$ of the depth which is labelled as the 'correct stress' in Figure 1. At shallower depths, the model incurs an 'under stress' condition while below, the model is in an 'over stress' condition. This effect is magnified according to the increase in the ratio of the model height to the centrifuge radius. Two-thirds depth is convenient for equating the gravity scaling since the under stress area is equivalent to the over stress area. On average the stress in the model is equivalent to the prototype.

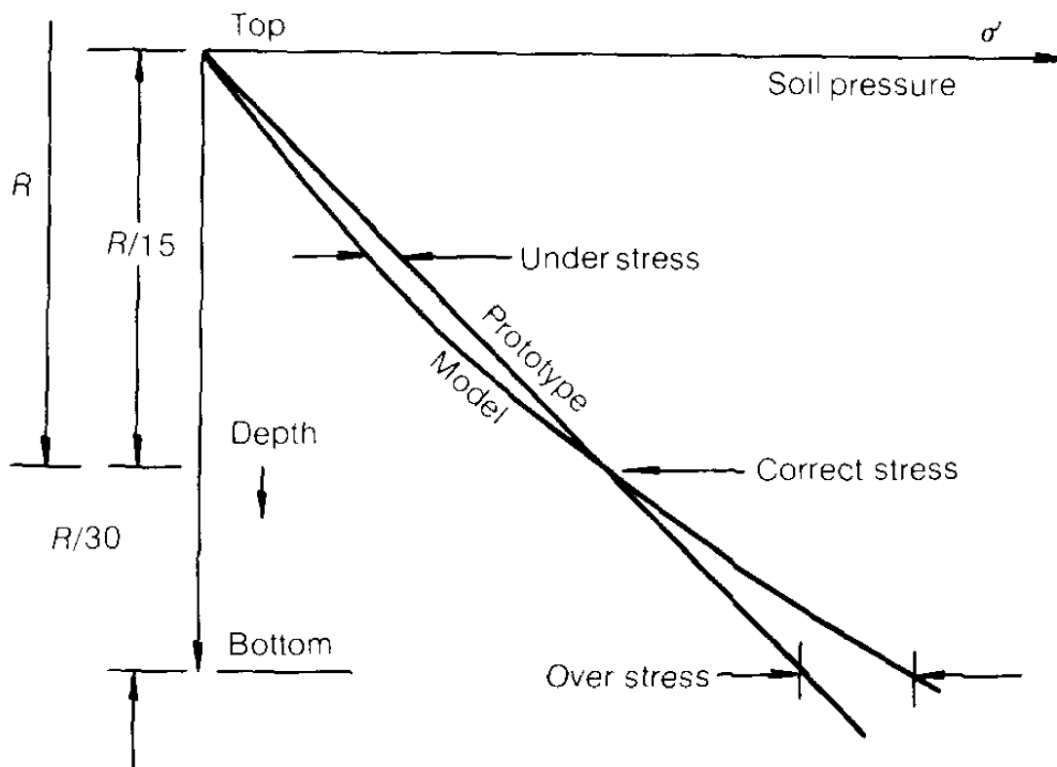


Figure 1 Effects of Gravity Field as a Function of Radius (Schofield, 1970)

Another factor that must be considered to ensure the impacts of scaling do not produce misrepresentative model behaviour is material selection. Schofield discusses a case study involving sensitive clays (provided by Queen's university in Kingston, Ontario by Professor Mitchell) which exemplifies the difficulties of using undisturbed samples in modelling. Because small variations or unique conditions in the fabric of the soil are magnified in centrifuge testing, these seemingly minor variables can have significant impacts on the total model behaviour and test results, especially with material like quick clays that have unique behaviours. He recommends the use of remolded soils for the study of soils with special properties due to their simpler and better defined material properties which improve the accuracy of the test and their repeatability, as well as removing the unwanted effects of any unique material properties or anomalous formations that may skew global results in a model.

Geotechnical centrifuge testing's utility is recognized globally and the use of geotechnical centrifuges has not been limited to the United Kingdom. In 1985 the Tokyo geotechnical institute recognized the benefits and need of the relatively easily procured "well-controlled experimental data" that geotechnical centrifuge modelling could provide and which would be invaluable for the calibration of numerical models (Kimura et al., 1985). The institute, using a bearing capacity problem, carried out a modelling of models scheme of tests with a newly constructed centrifuge and attempted to recreate behaviour of prototypes were also conducted with success in both methods. Modelling of models is a technique that tests a model of a geotechnical structure designed for one scale, to failure, and then tests a second model of the first model at another scale. The scales and the proportional applied scaling forces are then compared (Madabhushi, 2015). The effect of soil particle size scaling was also evaluated and shown to be negligible by the modelling of models among other methods. White presents an overview of the developments in the history of centrifuge geotechnical modelling and its improvement of modelling through advancements in the ability to interact with the models in flight as well as improved instrumentation and data acquisition, providing more opportunities to both produce effects and collect information on the models' behavior in flight (White, 2008). Recent work on progressive slope failure caused by cyclic weather effects (Take et al., 2002) is cited as a prime example of the invaluable detail of results that is uniquely obtainable through centrifuge testing. As a result of the benefits provided by this tool, geotechnical centrifuge modelling is being conducted around the globe by various institutions (White, 2008).

Centrifuge models are commonly used in geotechnical engineering research and teaching to model a broad variety of soil structures and behaviours, including shallow and deep foundations, slopes, retaining walls, tunnels, infrastructure corridors, and soil-structure interaction applications (White, 2008, Madabhushi 2015). These applications prompted the Geotechnical Engineering Group at the Royal Military College of Canada to acquire a geotechnical centrifuge. Prior to conducting further research and teaching exercises utilizing the centrifuge, it is necessary for the procedures, scaling, and results to be understood and verified to ensure accurate results that demonstrate the success of the application of the principles of physical modelling.

In this chapter, the RMCC Geotechnical Centrifuge's functionality is examined and the procedures for performing physical models are summarized. Functionality including data acquisition, image capture and analysis, and mechanical boundary conditions are examined. The capabilities of the RMCC Geotechnical Centrifuge are verified through physical models of undrained slopes and undrained bearing capacity. Results showed that the slope and

bearing capacity physical models agreed with equivalent theoretical solutions. A modelling of models exercise showed that models of different sizes gave equivalent results. These tests provide confidence in future use of the RMCC Geotechnical Centrifuge in research to examine the behaviour of geo-materials in elevated gravity environments.¹

2.2 The Royal Military College of Canada Geotechnical Centrifuge

The RMCC Geotechnical Centrifuge is pictured in Figure 2A and a diagram of the centrifuge at rest and in flight (B), showing the beam, cradles (both removed and installed within the centrifuge drum), stack and location of the onboard computer. The centrifuge is a 0.5m diameter, 6G-ton geotechnical beam centrifuge with the ability to apply 300g acceleration to two physical models simultaneously. The removable cradles are constructed of aluminum and contain two Perspex viewing windows for observation of models in flight. The maximum size of physical models are 300x180x100mm (width x height x depth) corresponding to a maximum prototype size of 90x54x30m. The beam contains an onboard computer for data acquisition and control of sensory equipment.

¹ This Chapter contains some of the results presented at the CYGEGC and the GeoVANCOUVER conferences (Appendix E) under the following citation:
Kingswood, J., LaPorte, S, Siemens, S., 2016. Verification of physical modelling with a geotechnical centrifuge using physical models of slope stability and bearing capacity, *In: Proceedings of the 69th Annual Canadian Geotechnical Conference*. Vancouver, Canada.

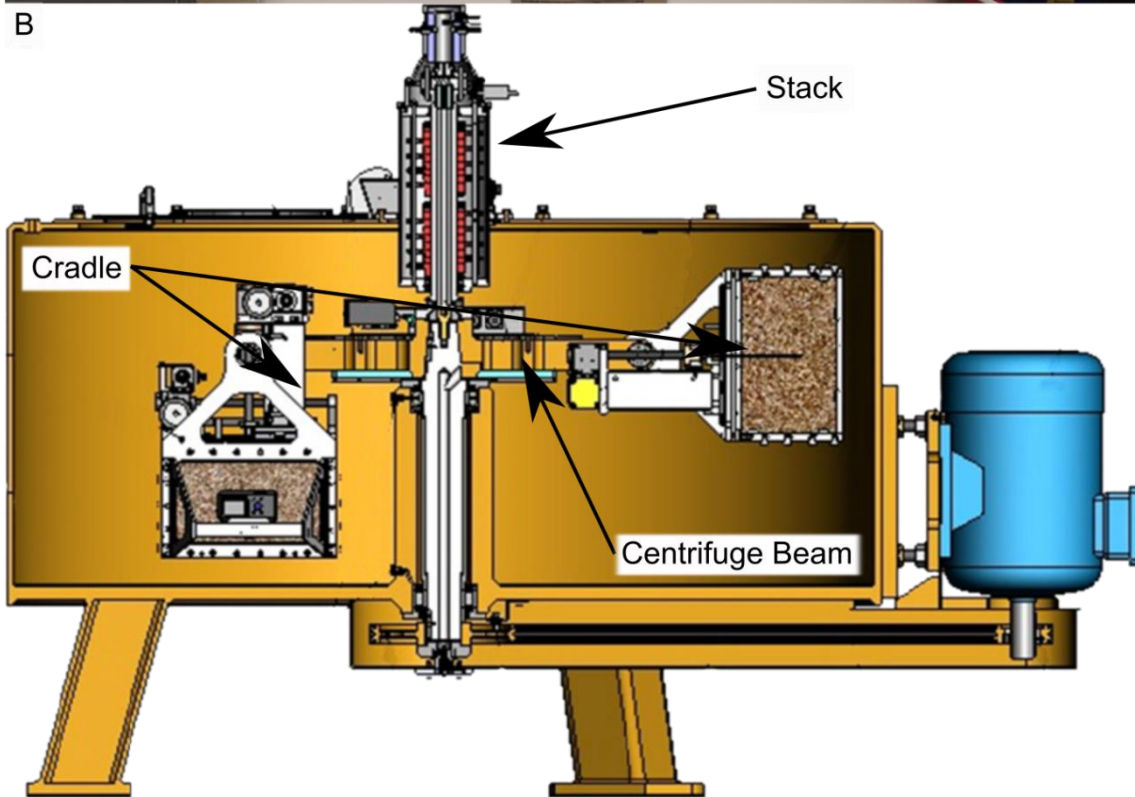
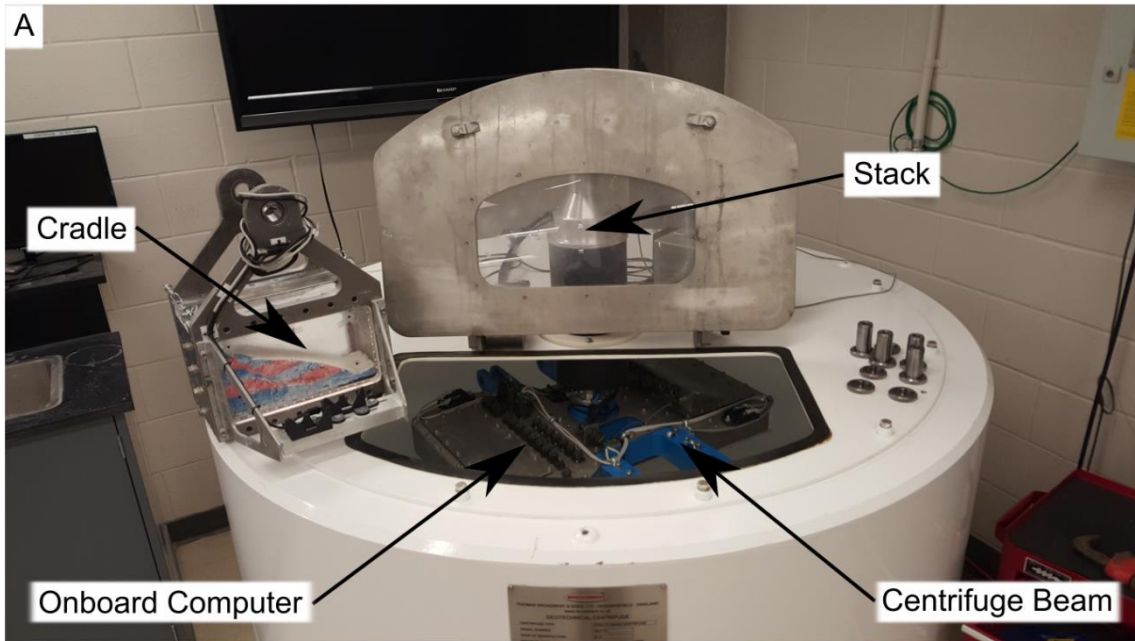


Figure 2 Image (A) and Diagram (B) of RMCC's Geotechnical Beam Centrifuge (Broadbent, 2015)

2.2.1 Scaling Laws

To produce useful data from centrifuge testing the relationship between the behaviour of the model and prototype must be carefully defined. Converting prototypes to physical models requires application and understanding of scaling laws (Garnier, 2007) and the gravity field. The gravity field varies both as a function of the rotational velocity of the centrifuge, and length of radius of the body in motion from the point of rotation. Equation 1 describes the relationship between the acceleration applied to the model in flight (Ng) as a function of the radius (r) and the angular velocity ($\dot{\theta}$) (Madabhushi, 2015).

$$Ng = r \dot{\theta}^2 \quad \text{[Equation 1]}$$

Figure 3 shows the relationships between the prototype and the model as a function of N . One dimensional properties such as length are modelled at Ng in relation to the prototype at $1g$ as $1/N$, two dimensional properties such as area are scaled as $1/N^2$, and the three-dimensional properties such as mass and volume as $1/N^3$ (Madabhushi, 2015).

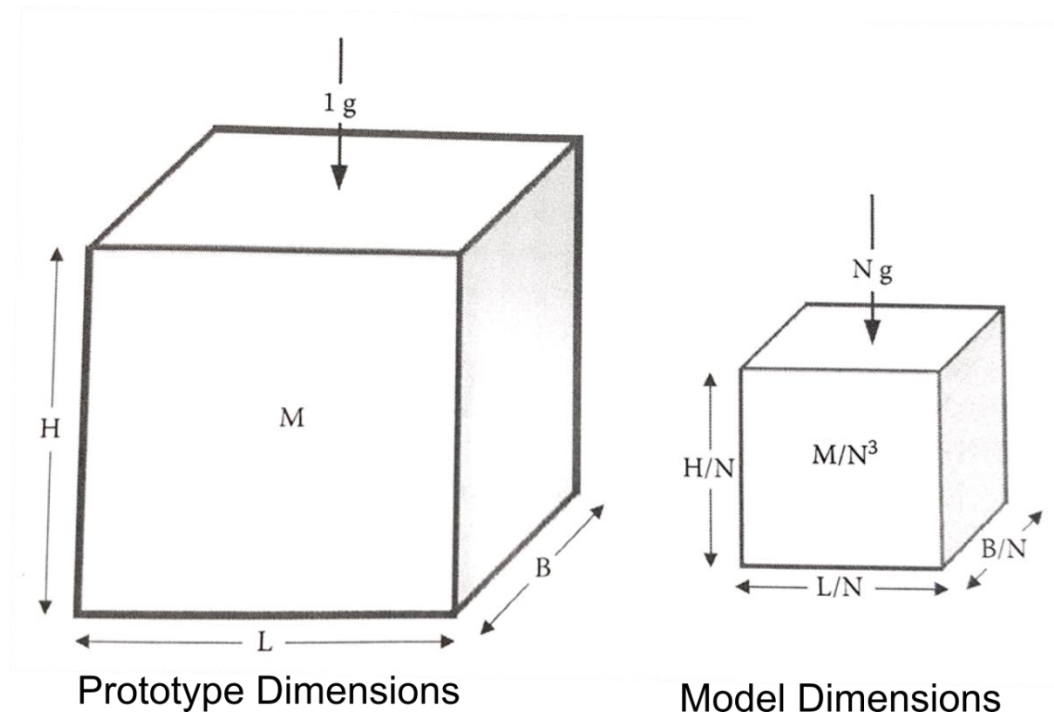


Figure 3 Scaling Relationships as a Function of N (Madabhushi, 2015)

If these scaling laws are applied to the centrifuge cradles the modelling ranges of the centrifuge can be seen. The centrifuge cradles which hold the models in the RMCC Geotechnical Centrifuge are $180 \times 300 \times 100 \text{mm}$ which, assuming a material unit weight of approximately 17kN/m^3 , allows the centrifuge to model prototypes of dimensions $54 \times 30 \times 90 \text{m}$, volume of $145,800 \text{m}^3$, and weight of over 250 tonnes. These values provide the

range of prototypes the centrifuge can be used to model. Despite its relatively small size (Figure 2) the centrifuge allows a variety of testing opportunities because of the high rotational velocity it can produce as well as its specialized control and observation features which permit a variety of interaction with the model and data acquisition during flight. Table 1 provides the basic operating limits of the centrifuge.

Table 1 Centrifuge Operating parameters (Broadbent, 2015)

| | |
|--------------------------|---------|
| Maximum rotational speed | 638 RPM |
| Maximum N ^{1,2} | 300 |
| Maximum payload | 90 kN |

¹N is the ratio of the acc. relative to the acc. of gravity (9.81m/s²)

²at 0.66 m radius

In addition to control of the applied forces, and control of data acquisition the centrifuge also has access through its point of rotation at the central stack that allows both water and air flow to the model to be permitted in flight by means of two conduits. This allows either the operation of pneumatic controls or wetting and drying control and effects (Appendix A, B) during flight. These features combine to produce an excellent tool for geotechnical modelling, testing and teaching for RMCC.

2.2.2 Gravity Field Considerations

Based on RMCC's centrifuge's physical dimensions, its large ratio of height of model to radius of rotation, experiments conducted within it require consideration of the variation in the gravity field over the depth of models. The implication of the variation in the gravity field is developed based on relations for scaling models previously discussed (Equation 1). The acceleration (Ng) is a function of the effective radius (r) and the angular velocity ($\dot{\theta}^2$), which is in turn a function of the radius and rotational speed (RPM) that the centrifuge is operating at. Due to the relatively short radius of the centrifuge beam, the sample's height is a significant proportion, 27%, of the nominal effective radius. This means that at any given rotational speed, significantly different radii are effective for any element with mass at different heights within centrifuge cradles, housing the model and counterweights (Schofield, 1980, Madabhushi, 2007). As a result the applied acceleration varies, at the maximum rotational speed, by 13% below and above the predicted value for the nominal effective radius (660mm) at the surface (570mm) and base (750mm) of a 180mm model. Figure 4 plots the centrifuges acceleration (N) for three radii at the base, effective radius, and surface of the model across the centrifuge's range of rotational speeds. This variation requires the calibration tests and any future use of the centrifuge to employ methodology that considers the radius's effect on stresses and behaviour in different portions of the model and the resultant effects on the tests' results. It must also be considered when balancing the centrifuge's cradles.

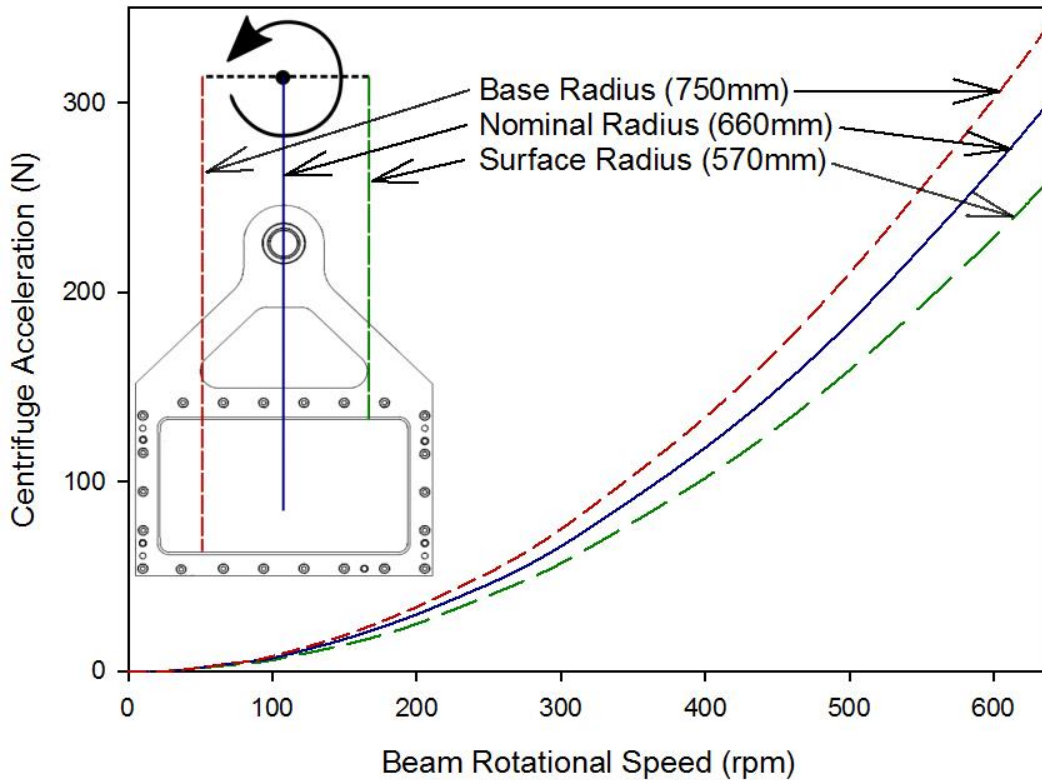


Figure 4 Gravity Field as a Result of Changes in Radius

2.2.3 Balancing the Centrifuge

The variation in gravity field impacts the balancing of the two cradles during flight in the centrifuge. When the centrifuge is in flight the difference between the forces acting on either side of the centrifuge beam must be minimized as much as possible in order to reduce vibrations and ensure the correct performance of the machine as well as the behaviour of the models. Because the two cradles and proportions of the beam are identical only the contents of the cradles and any additional apparatus attached to them (the difference between the two sides of the centrifuge) must be considered in the balance calculation. This is achieved by ensuring that Equation 2 is balanced where M_{PL} and N_{PL} are the mass of the payload (that is, the model cradle and any additional components) and the force of gravity acting on the center of mass of the payload, and M_{CW} and N_{CW} are the mass of the counterweight and the force of gravity acting on the center of mass of the counterweight. N_{PL} and N_{CW} are a function of their radius, the distance from the point of rotation to their center of gravity and the rotational velocity as described in Equation 2.

$$M_{PL}N_{PL} = M_{CW}N_{CW} \quad [\text{Equation 2}]$$

Although both cradles can be used to simultaneously conduct modelling tests it is often convenient to only conduct one test at a time in order to tailor g-path, wetting and drying, etc. to an individual model and to ensure that Equation 2 is properly satisfied. In this case, the remaining cradle is used simply as a counterweight and bags of iron filings placed inside the cradle provide the required mass to balance the payload. These are used because they can be quickly added or removed to achieve the requisite mass and provide a stable center of gravity with minimal movement during flight. If a counterweight shifts during flight it can change its center of gravity and cause the centrifuge to become out of balance. Because the counterweights are relatively dense they tend to sit with a lower center of gravity compared with a soil model; as a result, the length of their effective radius (and subsequently N_{CW}) is larger than that of the model; therefore, M_{CW} is required to be less than M_{PL} in order to balance Equation 2.

The centrifuge can safely tolerate approximately a 1kg variation between the payload and the counterweight at 300g. However, the greater this imbalance the greater the vibrations in the centrifuge and there is an increased likelihood of this impacting the test results. For tests in which the mass of the model changes (for example due to the addition or removal of water) or the radius of the center of gravity changes (as a result of consolidation or failure of a structure) this tolerance can be employed to minimize the change in balance which keeps vibrations minimized. This is done by calculating the starting mass and acceleration (M_{PL1} and N_{PL1}) and the final mass and acceleration (M_{PL2} and N_{PL2}) and then solving for M_{CW} with the average of the starting and final M_{PL} and N_{PL} (Equation 3).

$$\left(\frac{M_{PL1}+M_{PL2}}{2}\right)\left(\frac{N_{PL1}+N_{PL2}}{2}\right) = M_{CW}N_{CW} \quad \text{[Equation 3]}$$

As a result of using this method the centrifuge is out of balance by half of the over or under-balancing that would occur if the equation was solved using the starting or final values alone. This produces significant reduction in vibrations which ensures the equipment and test perform optimally.

2.2.4 Mechanical Boundary Conditions

In order to design models, correctly interpret results, and relate them to real world prototypes and theoretical behaviour, the boundary conditions for the models must be well understood, monitored, and controlled when required. The boundary conditions of the plane-strain model placed within the cradle are fixed in all directions by the aluminium side walls and Perspex observation windows of the cradle. On the normal axis, the models are free at the surface and bound at the base of the cradle. For the undrained slope and bearing capacity experiments presented in this chapter, the mechanical boundary conditions, in particular, friction treatment of the windows and model base were developed.

The internal vertical faces of the cradle are treated to limit friction developed between the sides of the models. This ensures that the model acts uniformly across its width, producing plane strain behaviour. Dow Corning high vacuum silicon grease is used to reduce friction along the acrylic Perspex to allow the soil to move freely along these surfaces. This grease was used because it is resistant to water and nonreactive. Its translucent white/gray colour also minimized its interference with the images taken through the Perspex that are used for analysis. The silicon grease is applied manually in a uniform, thin layer along any

boundary where shear is expected to occur between the model and the walls of the cradle. It is also placed along faces of regions where the failure of the model is expected to occur to minimize resistance during failure. This minimized the artificial impact of the immobile boundaries where, in prototype models, symmetrical movement would be experienced by soil or structural elements.

The converse case to a boundary condition that is required to allow movement is one where the interface should be fixed in order to be representative of prototype conditions. In slope experiments, the artificial potential for slippage along the interface of the model and aluminium cradle was observed in early tests. Figure 5A shows a shear plane descending through the profile and intersection the base of the model. The low interface friction developed between the base of the model and the aluminium cradle caused the slopes to fail prematurely and incongruently with the theoretical models where the location of this interface would, in a prototype, have the same frictional strength as the surrounding soil. Friction treatment was applied to the base of models with 3D printed serrated and perforated plates. Figure 6 shows a rendering of the .stl file used to print the PLA plastic plates that provide the friction treatment. The treatment was printed in two 150mmx100mm plates because of the limits of the dimensions the 3D printer can achieve. Alternating triangular peaks of 1mm/1mm/2mm provide a surface that does not allow clay particles to ride over the profile while perforations reduce plastic, increase friction, and for drained tests, allow conduction of fluid through the plate. The serrated plates increased the interface friction and caused the slopes to fail within the soil profile. Figure 6B shows the effectiveness of using the friction plates for a slope failure for two identical slope models. The slope without the frictional plates shows the failure plane descending to the base of the profile. The slope model, which incorporates the frictional interface (Figure 6B) shows the failure surface located 2-3 cm above the base. Thus, the negative effects of this boundary are removed from impacting the physical model results. Both slope stability and bearing capacity experiments reported in this chapter use the frictional inserts to correct this incidental effect of the cradle construction and boundary.

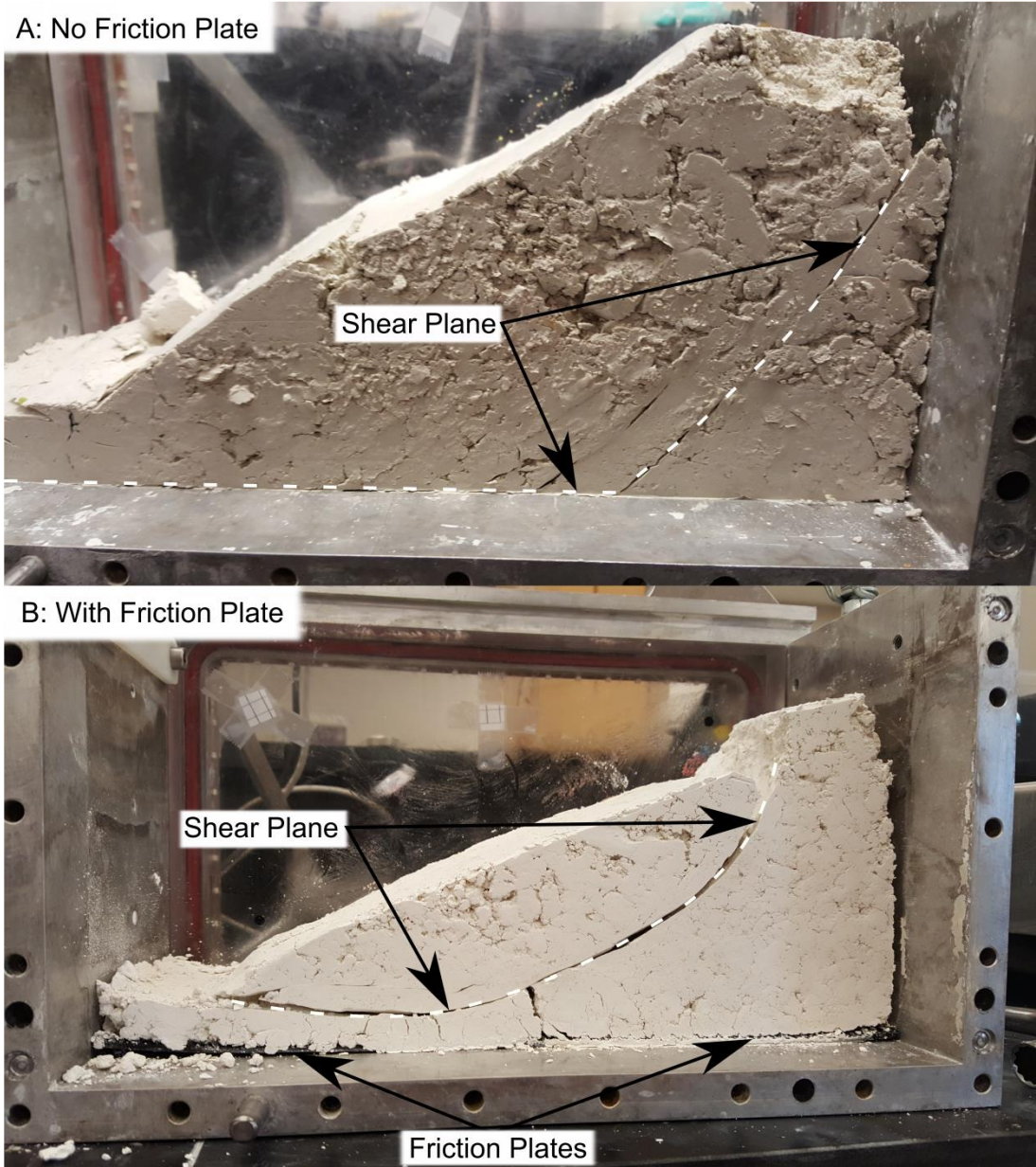


Figure 5 Effect of Base Friction Insert Plates from (A) Failure Plane without Plates, to (B) Failure Plane with Plates

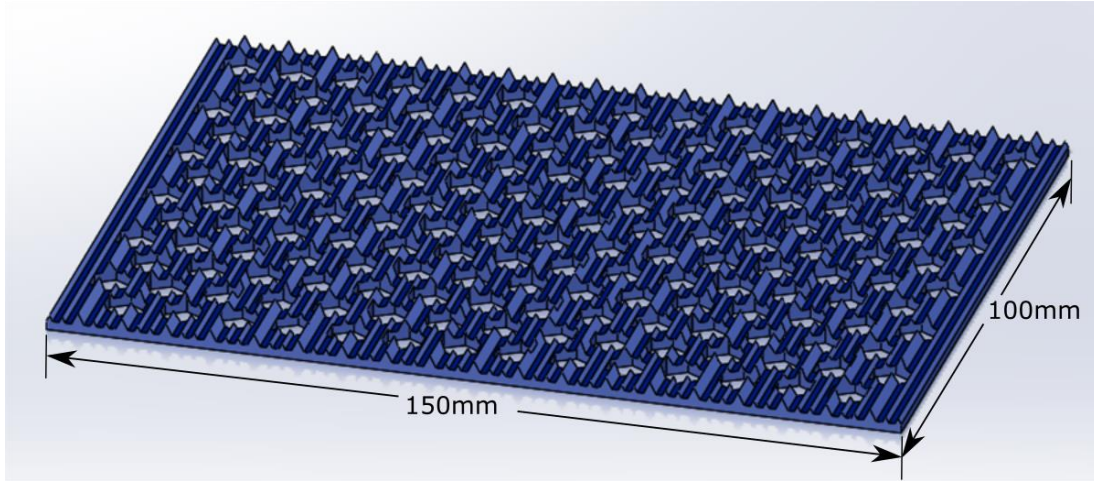


Figure 6 3D Printed Frictional Plate

2.2.5 Data Acquisition and Analysis

In order to maximize the use of the centrifuge the model must be observed through various instruments and measurements conducted during flight to properly understand and quantify the models' behaviours throughout its life. The centrifuge uses two primary methods of data acquisition: the onboard computer and data acquisition system (DAS) with associated sensors, and digital photo collection.

2.2.5.1 Onboard Computer

The centrifuge has a ruggedized solid state onboard flight computer with 16 hardware channels feeding an Aclipse DAS (Broadbent, 2015) that is designed to withstand the high forces produced in flight. This computer has a fiber optic connection that allows it to be remotely controlled by another computer outside the centrifuge drum during flight. The Aclipse DAS can display multiple channels to give current sensor readings of model behaviour and conditions within the centrifuge. This allows for monitoring of testing as well as acquisition in flight. The acquired data can be exported into a variety of formats, primarily spreadsheets, for further analysis.

2.2.5.2 Digital Cameras

The second method used for data acquisition and observation of the model in flight within the centrifuge is digital image gathering. Two cameras (HERO 4, and HERO 3 or 5MP ELP) are mounted on the equipment rail (approximately 80-130mm) from the Perspex viewing window in the cradle (Figure 7). A GoPro camera is used to gather data while the second camera, either GoPro or ELP is used for confirmation and observation during testing. The cameras are affixed to the rail with 3D printed mounts bolted to the rail that allow the cameras to be easily installed or removed and to be charged for long duration tests while minimizing error caused by movement in the lenses during acquisition.

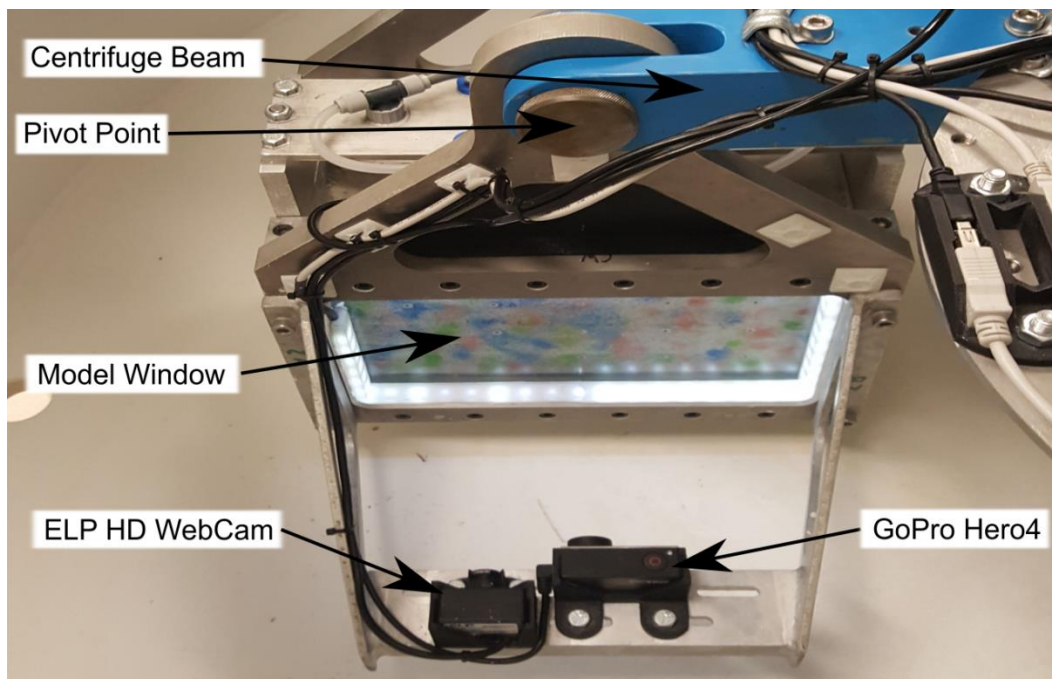


Figure 7 GoPro HERO 4 and ELP Webcam on Mounted on Cradle

The GoPro cameras were used because their fixed lenses, wide angle of view, and remote WIFI control options permit them to operate at the high forces experienced within the centrifuge and allow monitoring and control in flight. The ELP camera can provide a live feed to the onboard computer by USB. This is useful for ensuring models are behaving as required so that adjustments can be made if required and also for teaching demonstrations. Distance to the window can be adjusted to maximize pixel density through the use of the extended camera support. The GoPro cameras can take video, time lapse, or single or burst photos. Time lapse photo (ranging from 0.5 to 60 second periods) is primarily used to ensure even spacing between collection of images and simplify further data analysis. The HERO 4 camera has a 12MP resolution while the HERO 3 (which is used only for observation or video) has a 10MP resolution, and the ELP provides a 5MP live video stream from which stills can be captured. Both GoPro cameras are equipped with Micro SD cards for storage of photos while the captures from the ELP are stored on the on-board computer's hard drive and can be accessed through the remote computer.

2.2.5.3 Particle Image Velocimetry

White (et. al, 2003) produced a particle image velocimetry (PIV) for use in geotechnical modelling. PIV is a method of digital image analysis that tracks movements of model elements and produces displacement vectors for the model, describing its movement and distortion. It defines a grid of patches of pixels on a digital image. The program then compares subsequent photos and identifies the location of each of the patches in the mesh. The output from the PIV gives displacement of each patch in digital pixels as values which can be converted to vectors, or contours as well as a correlation coefficient to determine the

degree of accuracy the analysis is producing. The displacement of the pixels can be correlated to known control points and the displacement in real world units can also be calculated and displayed. The control points are placed on the centrifuge cradle's window not only to calibrate the scale but also to correct for minor movements in the camera mount and distortion from the camera lens. PIV allows for high resolution displacement data any number of points, throughout the depth of a model's cross section, to be gathered quickly and easily by the cameras in the centrifuge. Further details on the use of PIV can be found in Appendix C.

2.3 Verification Exercises

The initial requirement with a new piece of equipment like the RMCC Geotechnical Centrifuge is to verify its use and the associated scaling laws and equipment. Modelling of models is a technique for testing two (or more) physical models for a common prototype. The models are constructed at different scales and tested at proportional scaling forces that model the same structure prototype (Schofield 1980, Madabhushi, 2015). If the behaviour of the two models correspond to one another as well as to the expected behaviour of the prototype the results substantiate the scaling laws and methods used. Once they have been confirmed and tested in this way they can then be applied to new areas of research and testing. Modelling of models is typically performed in new physical modelling exercises to confirm the scaling laws are applied correctly and modelled behaviour agrees with accepted theory. In beam centrifuges of relatively small diameter modelling of models presents the opportunity to evaluate not only the ability to employ scaling laws but also the effects of incidental phenomena unique to this method of Modelling such as the impacts of variation in the gravity field, which must be considered during interpretation of results and mitigated in construction of testing schemes.

For the modelling of models testing for development of the RMCC Geotechnical Centrifuge, two types of prototype structures are considered; firstly, a remolded clay slope designed using a limit equilibrium analysis to a factor of safety (FoS) of 1.0 under undrained conditions and secondly a shallow foundation also loaded under undrained conditions constructed of the same clay to the same FoS. The prototype structures' expected behaviours are compared with accepted, simple analytical models. The slope stability models are compared with Taylor charts (Taylor, 1948) stability numbers. The shallow foundation models are compared with Terzaghi's (1967) bearing capacity values. The data for each model is analyzed to determine when failure occurs and the corresponding scaling forces applied to the model. This in turn is compared with the predicted prototype behaviour corresponding to the scaling forces at failure and with the behaviour of other scaled models. The degree of agreement is then evaluated for the agreement with the expected results from each of the methods and to evaluate the influences of incidental effects, boundary conditions, and material behaviours.

2.3.1 Undrained Slope Stability

Slope failure is a common and well known problem in geotechnical engineering and modelling of undrained slopes produces dramatic, easily observable, results (Schofield, 1970, Take et al., 2004). As a result, the mechanics of slope failure are well defined and well constrained problem, with controlled shear strength and geometry, allows for accurate

prediction of behaviour. This, coupled with the relative simplicity of instrumentation and analysis provide an ideal starting structure to employ the modelling of models. The modelling is done using a simple slope of known composition, and subjected to rapid loading to produce an undrained failure as described for the theoretical prototype structure.

2.3.1.1 Undrained Slope Stability Modelling of Models Theory

Taylor Charts are a method of determining the factor of safety for undrained slopes of homogenous composition (Taylor, 1948). Figure 8 is Taylor's chart for prediction of stability of a variety of slopes. The stability number (N_o) is related to the slope angle (i) through various curves corresponding to cases of failure and for a range of friction angles (ϕ_d). For an undrained toe failure, the method assumes that ϕ_d is equal to zero and a circular failures that start at the top of the slope and exit along the slope, at the toe or along the base of the slope corresponding to Case 3 the appropriate line is chosen. By equating the driving and resisting moments along the failure surface, Taylor developed stability charts that calculate a stability number for uniform unit weight and strength profiles.

A stability number (N_o) (Equation 4) is a function of the unit weight (γ), height of slope (H), and undrained shear strength (c). The primacy of the unit weight in the theoretically predicted behaviour of the model ensures that the effects of the centrifuge, both in its benefits and possible associated errors, will be easily discerned in the testing (Roscoe, 1970).

$$N_o = \frac{c}{\gamma H} \quad \text{[Equation 4]}$$

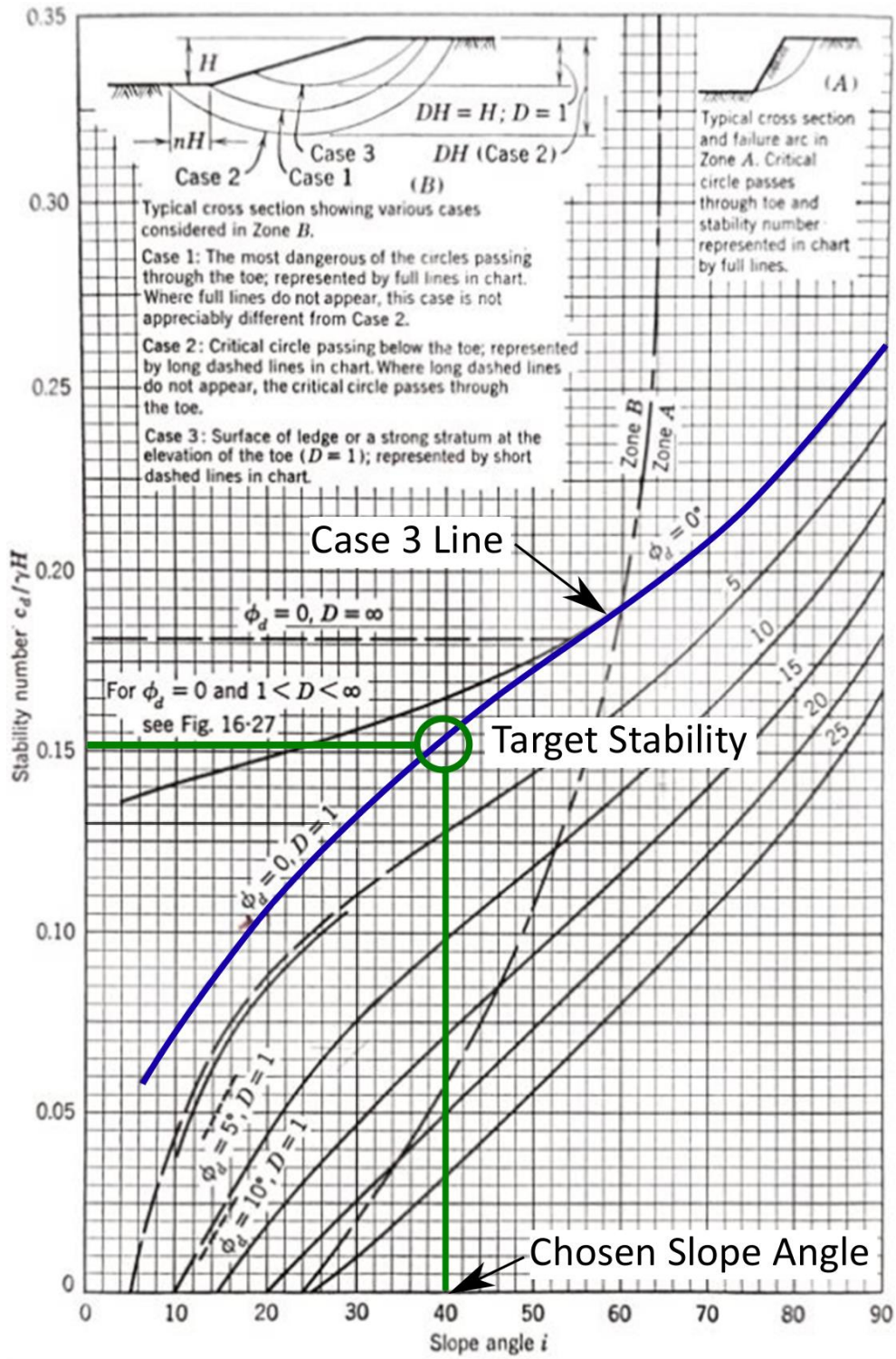


Figure 8 Taylor Chart (Taylor, 1948)

The corresponding N_o , for the chosen slope angle (i) at a FoS of 1.0 can then be determined from the chart for the appropriate slope failure geometry line, whether toe, deep, or slope. From this and a known unit weight and undrained shear strength, the maximum height at which the slope will be stable can be calculated.

For the modelling of models exercise, the models are designed such that c , γ (at 1g), i , and N_o are identical between the models. As a result, the scaling forces that will correspond to a scaled height of the model to the height at which a prototype will become unstable can be determined. In order to achieve that scaled height (and corresponding scaled γ) of the unstable slope an applied N at which the model is representing an unstable prototype is required; this is called the $N_{failure}$. Because the height of each model ($H_{model\ 1,2}$) is different the $N_{failure}$ for each model ($N_{failure\ 1,2}$) will differ. Equation 5 shows that for two slopes of identical model design (c , γ , i , and N_o) constructed at different heights ($H_{model\ 1,2}$) relative to the height of the unstable prototype ($H_{failure}$) the $N_{failure}$ for each model is proportional. Therefore, the proportion between $H_{model\ 1}$ and $H_{model\ 2}$ relative to their $N_{failure}$ is an inverse ratio.

$$\frac{\frac{H_{failure}}{H_{model\ 1}}}{\frac{H_{failure}}{H_{model\ 2}}} = \frac{H_{model\ 2}}{H_{model\ 1}} = \frac{N_{failure\ model\ 1}}{N_{failure\ model\ 2}} \quad \text{[Equation 5]}$$

2.3.1.2 Materials and Methodology

In this exercise, the slopes are tested for an undrained failure. By selecting a consistent material and carefully controlling the geometry and boundary conditions of the slope the behaviour of the prototype structure can be accurately predicted using a limit equilibrium analysis presented above with Taylor's chart. Because the slopes are required to have identical c , γ , i , and N_o , the soil preparation, model construction and testing scheme, must be as consistent as possible between tests. This is achieved by mixing to known water content, compacting using a consistent methodology, and applying forces with the geotechnical centrifuge along similar paths appropriate to the model design.

To prepare the soil with consistent material and state properties that would behave in an undrained way, a remolded, compacted clay soil was chosen. By using remolded Speswhite kaolin clay and controlling the water content a prediction of soil behaviour and similar material properties is achieved. Figure 9 shows the relationship between gravimetric water content (w) and undrained shear strength (c) determined using a shear vane on compacted kaolin clay samples at various water contents. Over the range used the relationship was estimated as linear. Using this relationship, a clay block with a predicted c can be constructed.

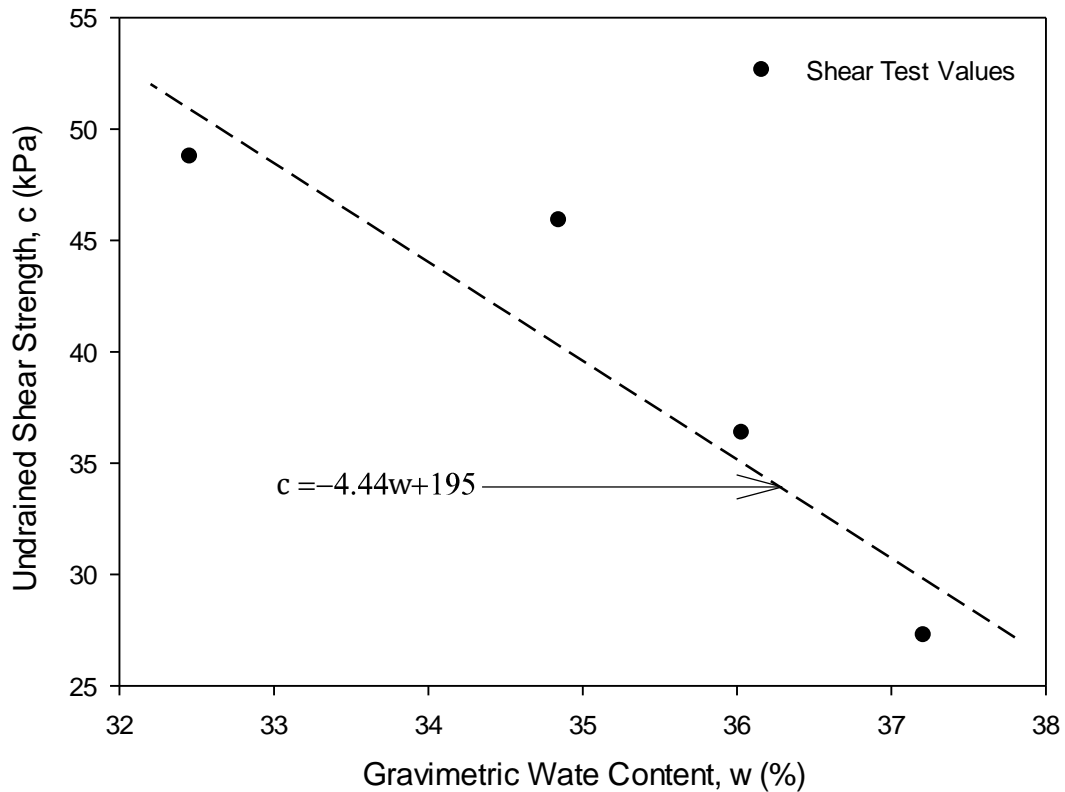


Figure 9 Relationship between Water Content and Undrained Shear Strength with Location of Actual Test Parameters

A typical clay block for construction of a slope is compacted to Standard Proctor density (ASTM D698-12e2, 2012). Approximately 8000g by dry mass of kaolin clay is measured out into a mixing bowl depending on the final volume required for construction of the model. The appropriate amount of water by mass is added to the bowl to achieve the target w for the test. This mixture is then combined using a metal spreader knife until it begins to come together. It is then mechanically mixed in a large stand mixer, using either the whisk or paddle attachment depending on consistency. For wetter soil mixes the paddle produces better mixing results and for dryer mixes the whisk is used. Once the soil is uniform, approximately five minutes of mixing with periodic scraping of the sides and bottom of the mixing bowl, it is ready for compaction.

A wooden form of the same dimensions as the centrifuge cradle is used for compaction. The sides are lubricated with silicon spray lubricant and the friction plate inserts are placed on the bottom of the form. Soil is compacted in three or five lifts of approximately 60 blows per lift to approximate the energy from a Proctor test and to provide consistency between models. The target height for the three lift model is 120mm and the target height of the five lift block is 170mm to accommodate the construction of models (Figure 10A) of two

different heights. The soil block is then removed from the forms and a coloured sand texture (Figure 10B) is applied to the face for the benefit of the PIV image analysis.

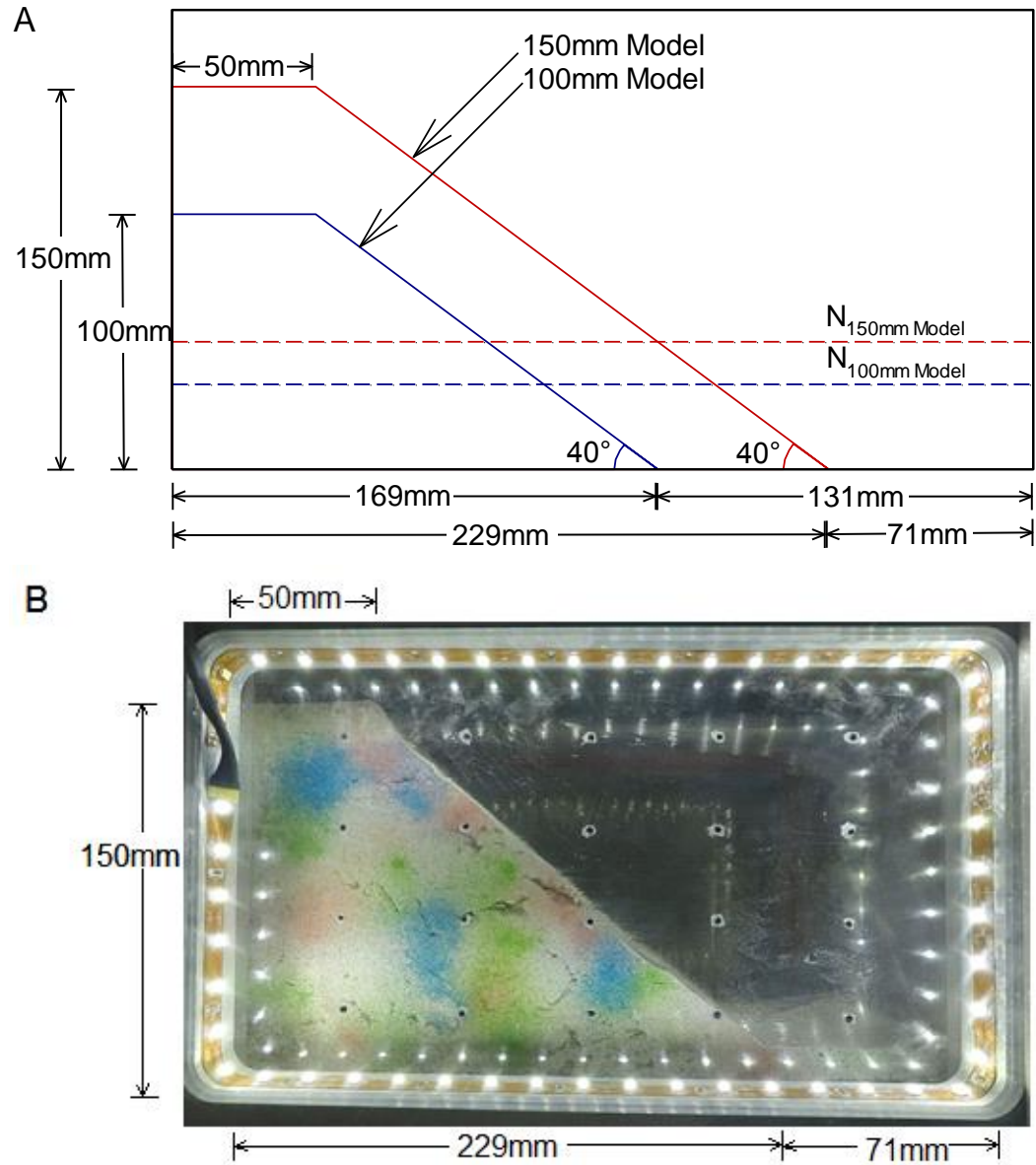


Figure 10 (A) Slope Geometry within the Centrifuge Cradle for Both Slopes and (B) Image of a Typical 150mm Slope

Once the soil block is removed and textured, the profile of each slope is cut into the block using a wire saw. Water contents are taken from the removed material. Figure 10 shows the

two 40° slope cross-sections with an image of a typical 150mm tall slope. The first model is constructed with a 150mm height, a 50mm standoff from the cradle's right boundary, and a 71mm run-out distance left for the failure. The second of the two models was selected at 1:1.5 proportion at 100mm height, 50mm standoff, and 131mm run-out. A typical (150mm) model prior to testing is shown in Figure 10. The target failure type is controlled by minimizing the depth below the model and employing boundary controls at the base of the model. Once the slope has been constructed the entire model is weighed. With the known geometry, the volume is determined and the average density of the soil is calculated. This is used to determine the unit weight of the soil.

With the model constructed it is placed inside the centrifuge cradle, taking care to lubricate all the surfaces that might interfere with the desired mechanism of failure. This is primarily the two Perspex viewing windows. The side of the cradle is reattached and the centrifuge cradle, with the GoPro HERO 4 and GoPro HERO 3 cameras for data collection and observation, is then weighed and the appropriate counterweight calculated using Equation 2. The cradle is then installed within the centrifuge (Figure 7) with the lighting and camera power. The GoPro HERO 4 camera is set to take a time-lapse of one frame per second for the duration of the test and the HERO 3 streams live images of the model so that the failure could be confirmed to have occurred before the test was stopped.

The predicted behaviour, that is, failure beyond the identified scaled model size at which the FoS of the prototype is equal to 1.0, sets the parameters for the scaling forces that are applied to the model. By applying forces with the geotechnical centrifuge along similar paths appropriate to the model design a consistent response is achieved. Owing to the variation in the gravity field, the nominal N value for the centrifuge was adjusted to apply the actual N_{failure} value to the center of mass of the slope. This was done to minimize the differences in applied gravity across the failure mass, averaging the "heavier" soil below the center of gravity with the "lighter" soil below. The values of gravity presented for the slope failures are the applied forces calculated for the slopes' centers of gravity.

The centrifuge is accelerated at three RPM/second to 20g. This allows any small settlements due to variations in compaction results to be largely removed. The model is then accelerated taking note of elapsed time and photo number, using a rapid stepped increase of N to ensure an undrained failure and provide data points throughout the scaling increase, to the predicted N_{failure} and past to approximately 120% of N_{failure} to ensure a full failure mechanism occurs. Data from self-weight consolidation tests and calculations of pore water pressure dissipation showed that less than 4% consolidation would take place throughout the duration of a 180sec test. This confirmed that the loading and failure took place under undrained conditions.

Once the model has been observed to fail, the test is stopped and the centrifuge decelerated. The model is then removed and the corresponding model is constructed and tested in the same manner.

2.3.1.3 Results

The results from a typical test are first presented followed by evaluating the whole exercise. The data obtained was evaluated in two ways. Firstly, the correlation between the two models and the ability to conduct the modelling of models was determined, and secondly the correlation with the analytical predictions for the behaviour of the theoretical prototype, using Taylor's limit equilibrium method was ascertained.

The tests are analyzed with PIV (GEOPIV8 version) to establish the N_{failure} . Time-lapse digital imagery of the models gathered during testing with a GoPro HERO 4 camera was processed to identify the formation of shear surfaces with respect to time and then correlated with the acceleration applied to the model at that time.

Figure 11 shows four figures. The first two images, A and B, show the slope at the beginning and end of the test, before and after failure respectively with the PIV patches overlaid over the images. The third shows the N applied to the model with respect to time during the test and the fourth shows the displacement vectors for the entire slope with the patches used for the analysis indicated.

A typical test is analyzed using the following method. Firstly, for a 150mm slope, a mesh of several patches (yellow boxes on Figure 11A, B, D) is selected, ensuring that the mesh includes some patches in the stable portion of the slope and others which will be in the active segment of the slope once it has failed. This mesh is applied to images taken throughout the test up to and past the point where failure was observed during the testing procedure. The PIV analysis shows resultant vector displacements (Figure 11D) for various elements in the analysis. The vectors are products of the vertical (v) and horizontal (u) displacements between the images for each step, summed together for net displacements from the beginning to the end of the test.

This displacement data can be used to more accurately identify when the slope fails. By plotting the vertical displacement of patches versus applied N the conditions at failure are interpreted.

Figure 12 shows the correlated N -path (Figure 11C) plotted with vertical patch displacement versus the stable and failure patches (Figure 11). During centrifuge spin-up, minor movements in the soil occur as small voids collapse with the increase of applied N . This can be observed in the pixel displacement of the data before failure. By placing some of the patches of the mesh in the stable portion of the slope a baseline displacement attributable to settlement can be distinguished from failure (Figure 11). At incipient failure, the landslide is formed and the failure zone accelerates and displaces relative to soil within the stable zone. Displacement of two of the patches, one in the stable and one in the failed portion of the slope, is plotted in Figure 12. At values of N less than 100, both patches move downward due to the increasing gravity field and subsequent minor displacements previously mentioned. As N is raised to greater than 100, the patch inside the failure zone displaces at an increasing rate. By fitting a line to the linear portion of the displacement versus N graph, the point of failure is interpreted as $N=100$ (

Figure 12). Thus, the gravity level at failure is interpreted as 100 for this test. Recalling that the values recorded are those calculated from the nominal effective radius (0.66m), the value of N must be corrected for the center of gravity of the slope. This value was chosen to be $1/3^{\text{rd}}$ the height of each slope; once the gravity field correction is applied to it, it is given the notation N_{failure} .

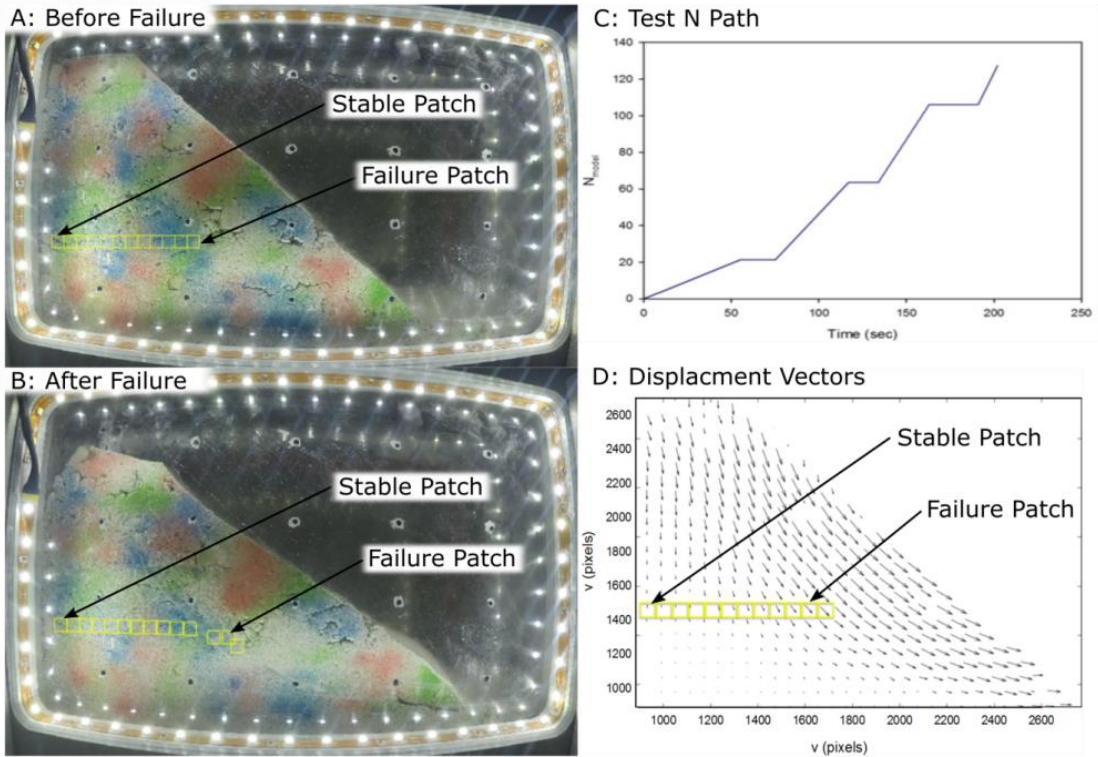


Figure 11 Results from a Typical 150 mm Undrained Slope Test Showing: (A) Image of Model before Failure, (B) Image of Model after Failure, (C) N_{model} versus Time, and (D) geoPIV Vector Displacement Results

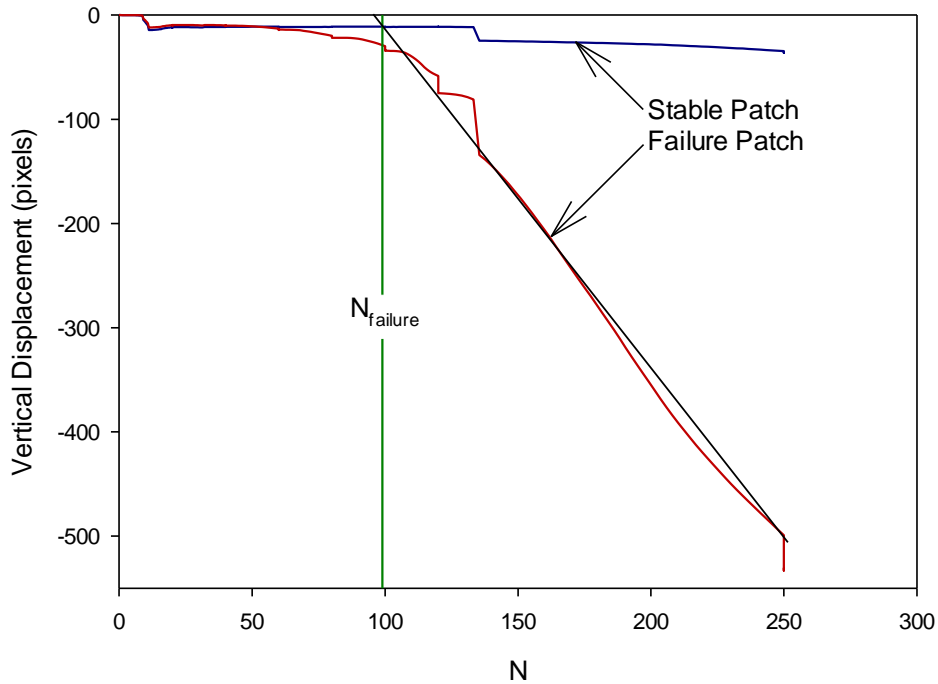


Figure 12 Stable and Failure Patch Displacement vs Time with Location of Failure

Each test was evaluated using this method and an observed $N_{failure}$ was established for each. A summary of the testing results is shown in Table 2 for a total of six undrained slope failure experiments, performed with pairs of tests consisting of a 150mm high slope and a 100mm slope and varied water contents. Experiments were analyzed in a similar manner as described above and Table 2 lists the observed gravity level at failure ($N_{failure}$) for each test.

The tests were conducted with three ranges of w (37-38%, 36-37%, and 35-36%) for each pair of slopes. Although the water content ranges are relatively narrow, the relationship between w and c (Figure 9 Relationship between Water Content and Undrained Shear Strength with Location of Actual Test Parameters) allows this range to provide a large span of testing (70-160g).

Table 2 Summary of Slope Stability Tests Results

| H_{model} (mm) | w (%) | Observed $N_{failure}$ |
|------------------|---------|------------------------|
| 150 | 37.7 | 73 |
| 100 | 37.4 | 108 |
| 150 | 36.5 | 83 |
| 100 | 36.8 | 115 |
| 150 | 35.3 | 111 |
| 100 | 35.0 | 154 |

Equation 6 produces the theoretical ratio of 1:1.5 ratio between the $N_{failures}$ for the 150mm and 100mm slopes for two models constructed at the same water content.

$$\frac{\frac{H_{failure}}{150mm}}{\frac{H_{failure}}{100mm}} = \frac{100mm}{150mm} = \frac{1}{1.5} \approx \frac{73}{108} \quad \text{[Equation 6]}$$

The correlation of $N_{failure}$ between the pairs of tests for each range of w is shown in Figure 13. The horizontal axis gives the $N_{failure}$ of the 150mm slopes and the vertical axis gives the $N_{failure}$ for the 100mm slopes. Also plotted on the figure is the theoretical ratio (1:1.5) which is predicted for the results. The observed relationship between the pairs of models produced ratios that fall within an average of 6% of the theoretical ratio predicted by Equation 6.

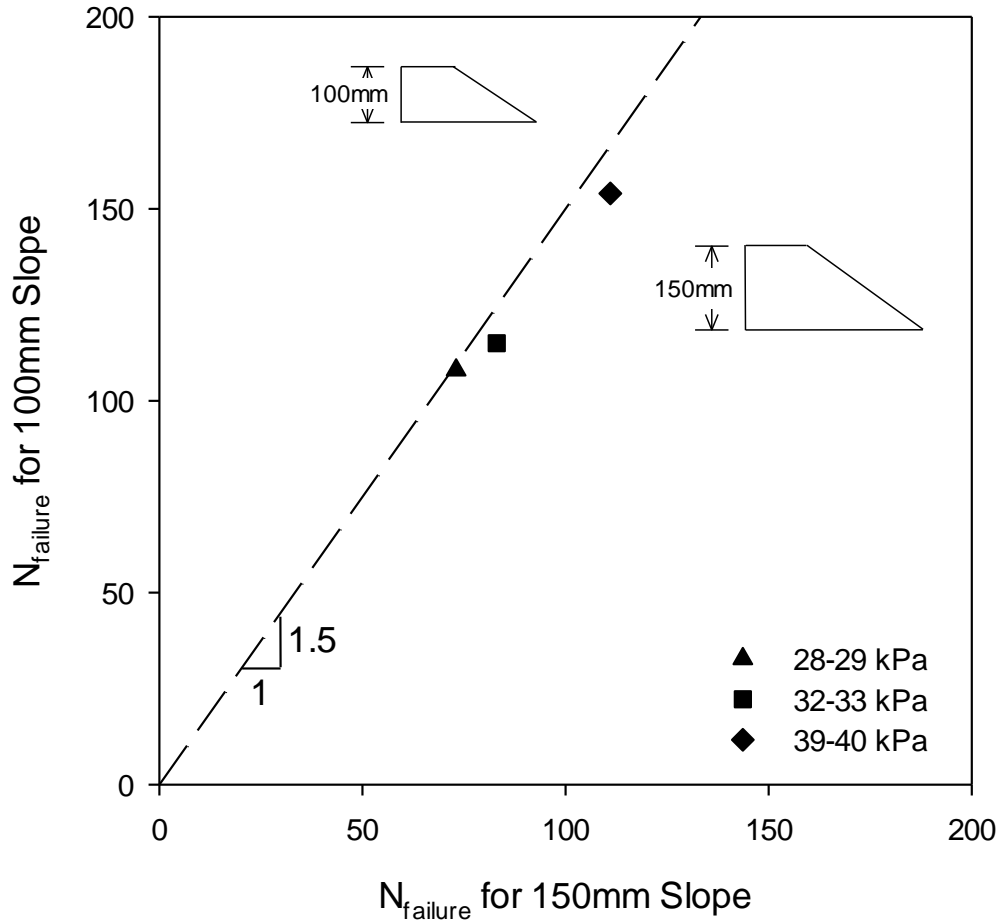


Figure 13 Slope Stability Modelling of Models Correlation

The second evaluation of the tests is performed by comparing the observed N_{failures} to the N_{failure} predicted for theoretical prototype, analyzed with the Taylor chart. Table 3 gives a summary of the testing scheme including w , associated c , and predicted H_{failure} calculated using Equation 4. The required N to achieve the instability calculated by the Taylor chart and Equation 4 is also given as predicted N_{failure} .

Figure 14 plots the observed N_{failure} from Table 2 with the predicted N_{failure} from Table 3. The figure also presents a 1:1 line on which all data points should plot for good agreement between the observation N_{failures} from the model and the predicted N_{failures} for the prototype. The closed symbols are the 150mm slopes and the open symbols are the corresponding 100 mm tall slopes. Comparing the data to the 1:1 line shows the failures corresponded within an average range of 4% of the predicted values.

Table 3 Slope Stability Testing Parameters for 40° Slope

| H_{model} (mm) | w (%) | Predicted c (kPa) | Predicted H_{failure} | Predicted N_{failure} |
|----------------------------|----------|----------------------|-----------------------------------|-----------------------------------|
| 150 | 37.7 | 28 | 10.4 | 69 |
| 100 | 37.4 | 29 | 10.8 | 108 |
| 150 | 36.5 | 33 | 12.3 | 82 |
| 100 | 36.8 | 32 | 11.9 | 119 |
| 150 | 35.3 | 39 | 14.6 | 97 |
| 100 | 35.0 | 40 | 14.9 | 149 |

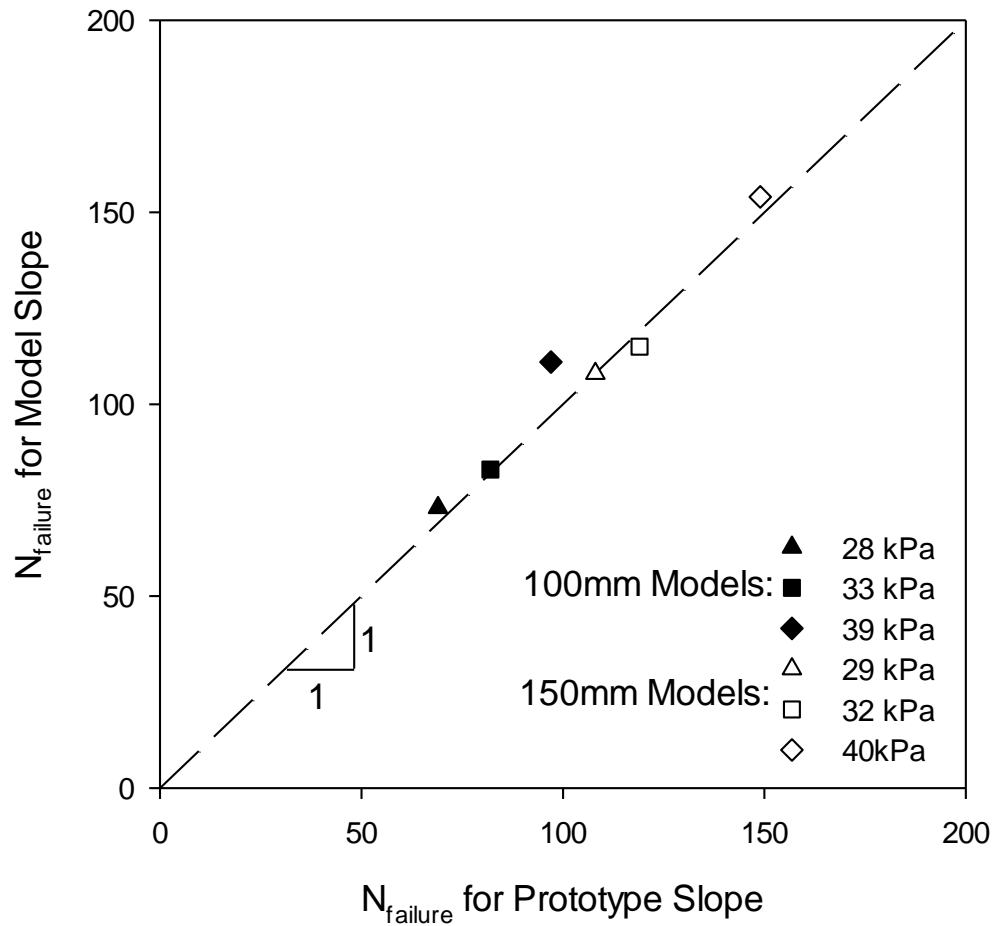


Figure 14 Observed Slope Stability Correlation with Theoretical Prediction

2.3.2 Undrained Bearing Capacity

The second type of structure selected to be modelled was a shallow foundation. This geotechnical structure is also well studied and its mechanics have been described by Terzaghi's (1967) bearing capacity equation. However, because the mechanism of failure is more complex and the test involves applied loads to the soil rather than simply self-weight it presents greater challenges for modelling (Kimura, et al., 1985). In order to be able to best observe the behaviour in the centrifuge, a strip footing with a theoretically infinite length was chosen for the verification tests.

2.3.2.1 Undrained Bearing Capacity Modelling of Models Theory

Terzaghi's strip footing bearing capacity equation (Equation 7A) describes the three components that contribute to the bearing capacity (q) of a footing. The first term is related to the soil's cohesion, its undrained shear strength (c), and its ability to resist shearing failure, where, the second is related to the stress from depth of the overburden material adjacent to and above the level of the foundation's applied load (D_f), and the third is related to the mass of the soil as a function of unit weight (γ).

$$q = cN_c + \gamma D_f N_q + \frac{1}{2} \gamma B N_\gamma \quad [\text{Equation 7A}]$$

By loading the soil rapidly and placing the applied load at the surface of the soil the equation's second and third terms equal zero as N_γ equals zero when the friction angle of the soil is zero (which the undrained condition produces) and the second term goes to zero as D_f equals zero because the foundation is placed on the surface of the soil and no overburden is present. This simplifies the bearing capacity for undrained loading to a function of c and the factor N_c which is constant at $2+\pi$ (Equation 7B).

$$q = cN_c \quad [\text{Equation 7B}]$$

For analysis of centrifuge physical modeling of models, Equation 7B can be used to determine the maximum width (and corresponding mass) at which the ultimate bearing capacity of the soil is reached, that is, a FoS equal to 1.0, and will fail. If the models are designed such that the undrained shear strength for both the models is the same, the scaling forces that applies a greater applied stress from the footing than the ultimate bearing capacity can be determined. This gives a predicted N applied at which the model is scaled to behave as footing with insufficient bearing capacity for the applied stress; this is called the N_{failure} .

The representative dimension of the footing that is used to compare the scale of the models is the width of the strip footing. Both the bearing capacity and the applied loading stress are functions of this dimension. Equation 8 shows that for strip footings of identical shear strengths constructed with different footing widths $B_{\text{model } 1,2}$ relative to the footing width of the unstable prototype $B_{\text{prototype}}$, the N_{failure} for each model ($N_{\text{failure } 1,2}$) is proportional. Therefore, the relationship between the width of the models and between the respective N_{failures} is an inverse ratio.

$$\frac{\frac{B_{failure}}{B_{model 1}}}{\frac{B_{failure}}{B_{model 2}}} = \frac{B_{model 2}}{B_{model 1}} = \frac{N_{failure model 1}}{N_{failure model 2}} \quad [\text{Equation 8}]$$

2.3.2.2 Methodology and Materials

For this test, the strip footing model construction and testing methodology is designed for an undrained failure of a strip footing. By using the same consistent material as the previous exercise and carefully controlling the geometry, loading, and boundary conditions of the footing, the behaviour of the prototype structure can be predicted using Terzaghi's theory with the simplifications producing Equation 7B. A similar method of soil preparation and testing scheme was employed with adjustments made for the differences in model design and mechanism of failure.

A typical test is conducted with the following methodology. Using a remolded Speswhite kaolin clay and controlling the water and the relationship described in Figure 9 a clay block with a predicted c can be constructed. The block was created using the same technique as was done for the blocks used for the slopes. Once the block has been constructed to approximately 150mm (or 80mm) tall it is removed from the mold and the coloured sand texture is applied (Figure 15) for the PIV analysis.

Once the soil block is removed and textured a flat uniform surface at the required depth is cut into the block using a wire saw. The geometry was chosen in order to achieve a depth of at least two times the width of the strip footing. The first model is constructed with 120 mm depth and a second smaller model at the footing with at 60mm. Figure 15 shows the two footing designs with the depth of soil below the strip footings. Once the soil depth has been achieved, the soil is placed inside the cradle, lubricating the required faces that will be in contact with the Perspex viewing window and the side of the cradle is reattached.

The strip footings are then installed on the surface of the clay blocks (Figure 15). The strip footings are constructed from steel blocks with dimensions of approximately 56x56x100mm and 28x28x100mm respectively. The steel blocks were fitted into PLA 3D printed plastic footings with widths of 60mm and 30mm respectively and lengths of 100mm. The plastic portion of the footing is designed with a .75mm groove around the base into which a 1mm rubber o-ring is placed. This well-greased o-ring reduces the soil which would be forced between the Perspex and the footing during failure and minimize friction with the window. These combined foundations have masses of 500g and 2000g respectively. The strip footing is bounded perpendicular to its running length by the Perspex windows of the cradle and allow the footing to be observed in failure in cross section. Figure 15 shows an image of a typical 30mm footing used for the undrained bearing capacity test.

The constructed model and the centrifuge cradle, with the GoPro HERO 4 and GoPro HERO 3, is then weighed and the appropriate counterweight calculated using Equation 2. The cradle is then installed within the centrifuge (Figure 7) with the lighting and camera power. The GoPro HERO 4 camera is set to the same time-lapse of one frame per second as is used in the slope failure tests.

The predicted behaviour, that is, failure beyond the identified scaled model size at which the FoS for the bearing capacity of the prototype is equal to 1.0, sets the parameters for the scaling forces that are applied to the model. The centrifugal forces are applied along similar paths appropriate to the model design. Owing to the variation in the gravity field, the nominal

N value for the centrifuge was adjusted to apply the actual $N_{failure}$ value at the surface of the soil and base of the block where the width of the footing, the driving proportional dimension, is in contact with the soil. This was done to minimize the differences in applied gravity between the mass of the footing and the soil it is placed on. The values of gravity presented for the bearing capacity failures are the applied forces calculated for this interface between the soil and foundation.

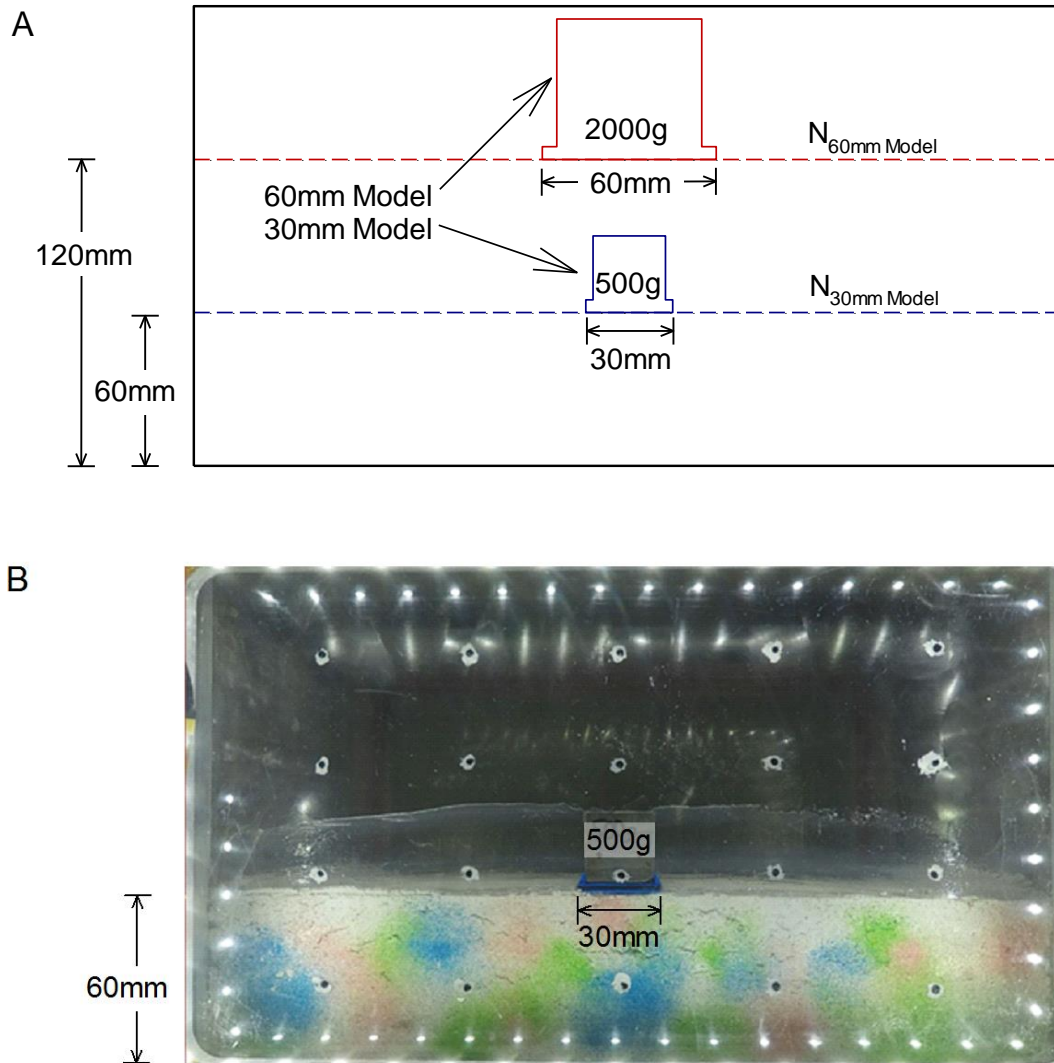


Figure 15 (A) Strip Footing Geometry within Centrifuge Cradle for Both Strip Footings and (B) Image of Typical 30mm Strip Footing

The centrifuge is first accelerated at three RPM /second to 20g. The model is then accelerated taking note of elapsed time and photo number, using a rapid stepped increase of

N to ensure an undrained failure and provide data points throughout the scaling increase, to the predicted N_{failure} and past to approximately 120% of N_{failure} to ensure a full failure mechanism occurs.

Once the model has been observed to fail, the test is stopped and the centrifuge decelerated. The model is then removed, water contents are taken from the middle of the soil block and the corresponding strip footing model is constructed and tested in the same manner.

2.3.2.3 Results

The results from a typical bearing capacity test are first presented followed by evaluating the whole exercise. The data obtained was evaluated in two ways. Firstly, the correlation between the pairs of models and the ability to conduct the modelling of models was determined, and secondly the correlation with the analytical predictions for the behaviour of the theoretical prototype, using the simplified version of Terzaghi's equation was ascertained.

The tests are analyzed with PIV (GEOPIV8 version) to establish the N_{failure} . The time-lapse digital imagery of the models gathered during testing was processed to identify the formation of shear surfaces using a similar method to the slope failure analysis with some variation to accommodate the differences in the anticipated failure mechanism.

Figure 16 shows four figures. The first two images, A and B, show the strip footing at the beginning and end of the test, before and after failure respectively with the PIV patches overlaid over the images of a typical 60mm width footing. The third shows the N applied to the model with respect to time during the test and the fourth shows the displacement vectors for the entire soil block with the patches used for the analysis indicated.

A similar method of relative movement in the model was employed but the more complex failure mechanism required a different selection of criteria. A typical test is analyzed using the following method. Firstly, for a 60mm strip footing, a mesh of several patches (yellow boxes on Figure 16A, B, D) is selected, ensuring that the mesh includes some patches below the footing and others that are adjacent to the footing but encompassed within segment of the soil. This mesh is applied to images taken throughout the test up to and past the point where failure was observed during the testing procedure. The PIV analysis shows resultant vector displacements (Figure 16D) for various elements in the analysis. The vectors are products of the vertical (v) and horizontal (u) displacements between the images for each step, summed together for net displacements from the beginning to the end of the test.

This displacement data can be used to more accurately identify when the foundation fails. By plotting the vertical displacement of patches versus applied N the conditions at failure are interpreted. Figure 17 shows the correlated N-path (Figure 16C) plotted with vertical patch displacements for two representative patches; one under the footing and another in the adjacent shear zone (Figure 16). These patches were selected as they were anticipated to show similar movements during the initial increase in gravity but obviously disparate behaviour during failure. During spin-up the patch underneath the footing shows minor settlement at a steady rate under the constant increase in acceleration applied by the centrifuge and the patch adjacent to the failure remains relatively stable; however, the movements are in the same direction at values of N less than 110. As the centrifuge continues to increase N past 110, the rate of vertical displacement of the patch below the foundation increases and a clear bilinear behaviour is seen. The patch adjacent to the footing stops its gradual vertical displacement and begins to move rapidly upwards. The change in rate of

vertical displacement below the footing and the reverse of direction adjacent to the footing were attributed to failure of the footing forcing the soil below it downwards rapidly and the uplift caused by the displaced soil under the footing for the respective patches. Both these changes in the behaviour of each patch occur at the same N , $N=100$. The patches' relative displacements as a function of the applied N (Figure 17) allowed for the identification of the bearing capacity failure where these two changes occur. By fitting a line to the linear portions of the displacement versus N graph, the point of failure is interpreted as $N=110$ (Figure 17). Recalling that the values recorded are those calculated from the nominal effective radius (0.66m), the value of N must be corrected for the interface between the footing and soil; once the gravity field correction is applied to it, it is given the notation $N_{failure}$.

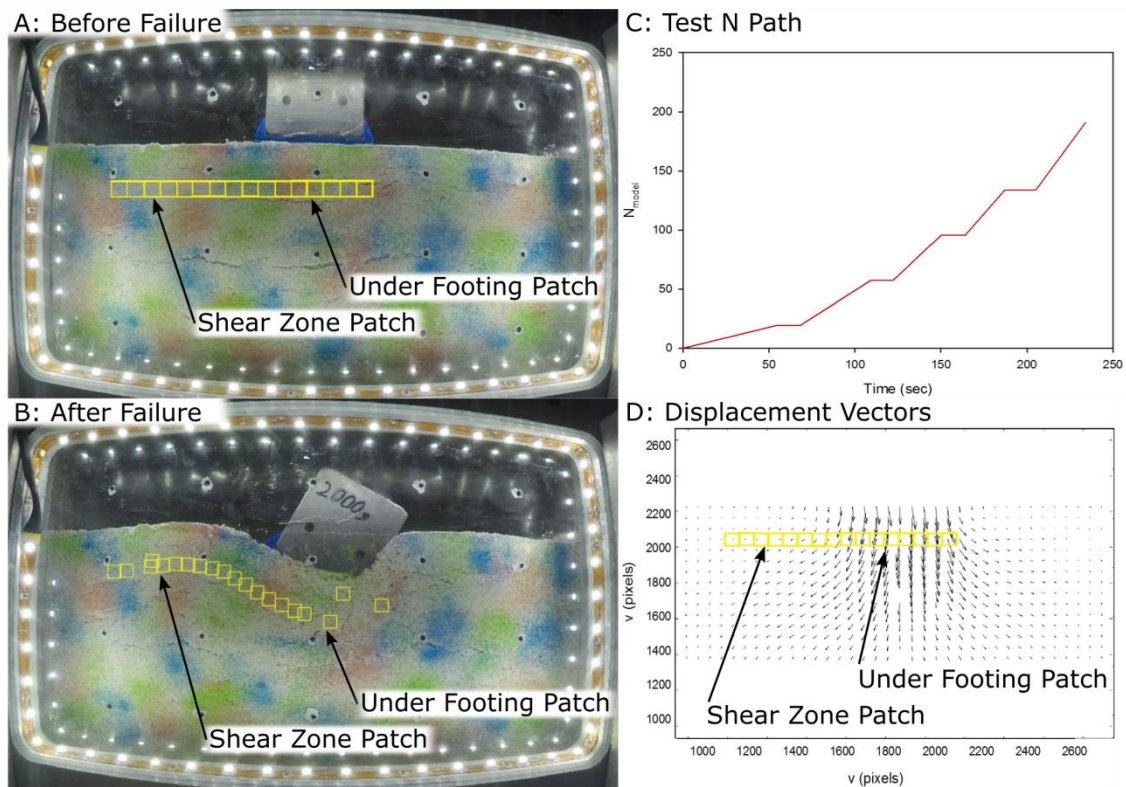


Figure 16 Results from a Typical 60 mm Undrained Slope Test Showing: (A) Image of Model before Failure, (B) Image of Model after Failure, (C) N_{model} versus Time, and (D) geoPIV Vector Displacement Results

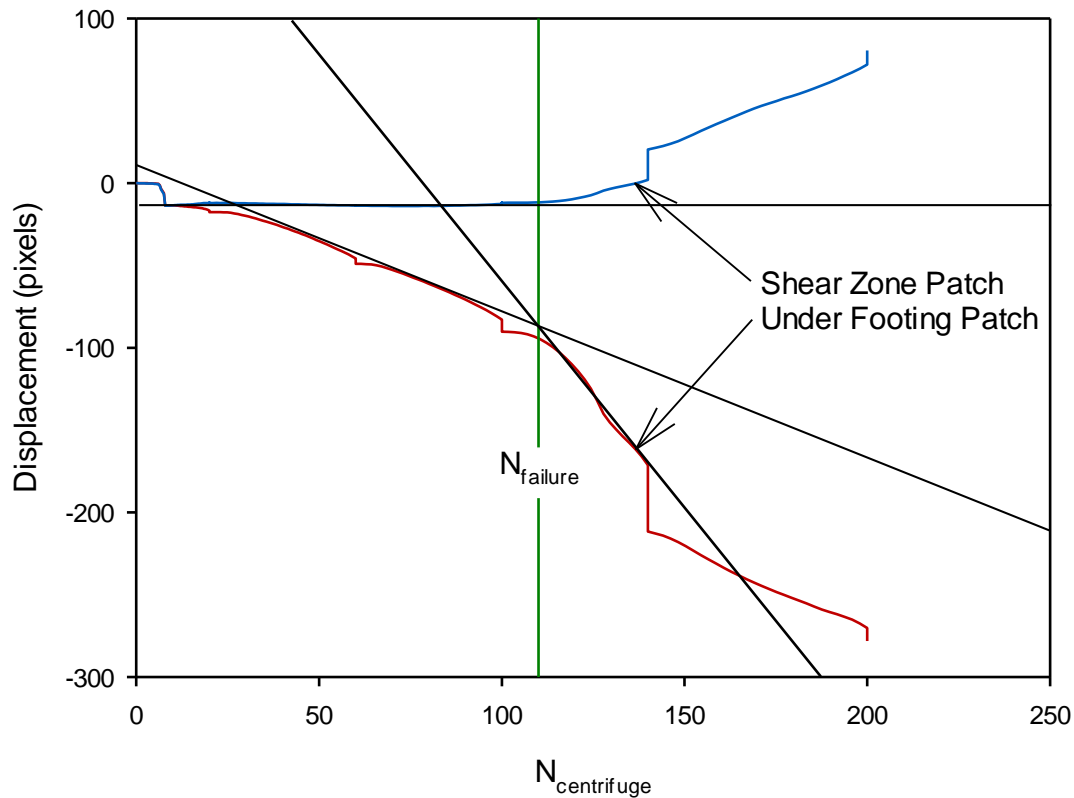


Figure 17 Patch Displacement vs Time with Location of Failure

These criteria for $N_{failure}$, the change in the rate of vertical displacement for the first patch and the change in the direction of displacement for the second patch were used to evaluate all of the strip footing models' observed $N_{failure}$. A summary of the testing results is shown in Table 4 for a total of six undrained bearing capacity failure experiments, performed with pairs of tests consisting of a 60mm and 30mm base width footings with varied water contents.

Table 4 Summary of Strip Footing Bearing Capacity Test Results

| B_{model} (mm) | w (%) | Observed $N_{failure}$ |
|---------------------|----------|---------------------------|
| 60 | 33.9 | 78 |
| 30 | 34.9 | 164 |
| 60 | 32.6 | 110 |
| 30 | 32.9 | 176 |
| 60 | 34.5 | 67 |
| 30 | 34.6 | 177 |

The ratio between the footing widths is 1:2 and the ratio between the masses of the strip footings is 4:1. This is a result of the scaling laws previously discussed; while the linear width of the footing is scaled as $1/N$ from model to prototype the cross section presents an area, with a scale of $1/N^2$ for the steel mass. Applied stress (q_{applied}) is a function of the mass and area (Equation 9) and so the ratio of the mass of the footing must always increase at the square of the ratio of the footing area. The area (A) of the footing and the mass (m) of the footing are then scaled at $1/N^2$ and $1/N^3$ respectively. For a unit length of an infinite footing, width (B) of the footing and the mass (m) of the footing are then scaled at $1/N$ and $1/N^2$ respectively (Equation 9). The scaling relationship between the model and prototype (or model and scaled model) is then $1/N$ (Equation 10). Because of this scaling relationship (Equation 10) and the relationship between applied stress and footing width, the ratio of the footing widths between models is description of the relationship between the behaviour of the two models. Equation 11 produces the following ratio of 1:2 ratio between the 60mm and 30mm footings for two models constructed at the same water content.

$$q_{\text{applied}} = \frac{mN^3}{AN^2} = \frac{mN^2}{BN^1} = \frac{mN}{A} \quad [\text{Equation 9}]$$

$$\frac{q_{\text{applied model}}}{q_{\text{applied prototype}}} = \frac{B_{\text{model}}}{B_{\text{prototype}}} = \frac{1}{N} \quad [\text{Equation 10}]$$

$$\frac{\frac{B_{\text{failure}}}{60\text{mm}}}{\frac{B_{\text{failure}}}{30\text{mm}}} = \frac{30\text{mm}}{60\text{mm}} = \frac{1}{2} \approx \frac{78}{164} \quad [\text{Equation 11}]$$

The correlation of N_{failure} between the pairs of tests for each range of w is shown in Figure 18. The horizontal axis gives the N_{failure} of the 60mm slopes and the vertical axis gives the N_{failure} for the 30mm slopes. Also plotted on the figure is the theoretical ratio (1:2) which is predicted for the results. The observed relationship between the pairs of models differ from the theoretical ratio predicted by Equation 9 by an average of 16% for the bearing capacity test series, however, much of the variance can be attributed to the greater range of water contents (Table 4). Kaolin's undrained shear strength changes 4.4 kPa (Figure 9) for every 1% of moisture content. Because of this, differing moisture contents is likely a contributing factor to this variance.

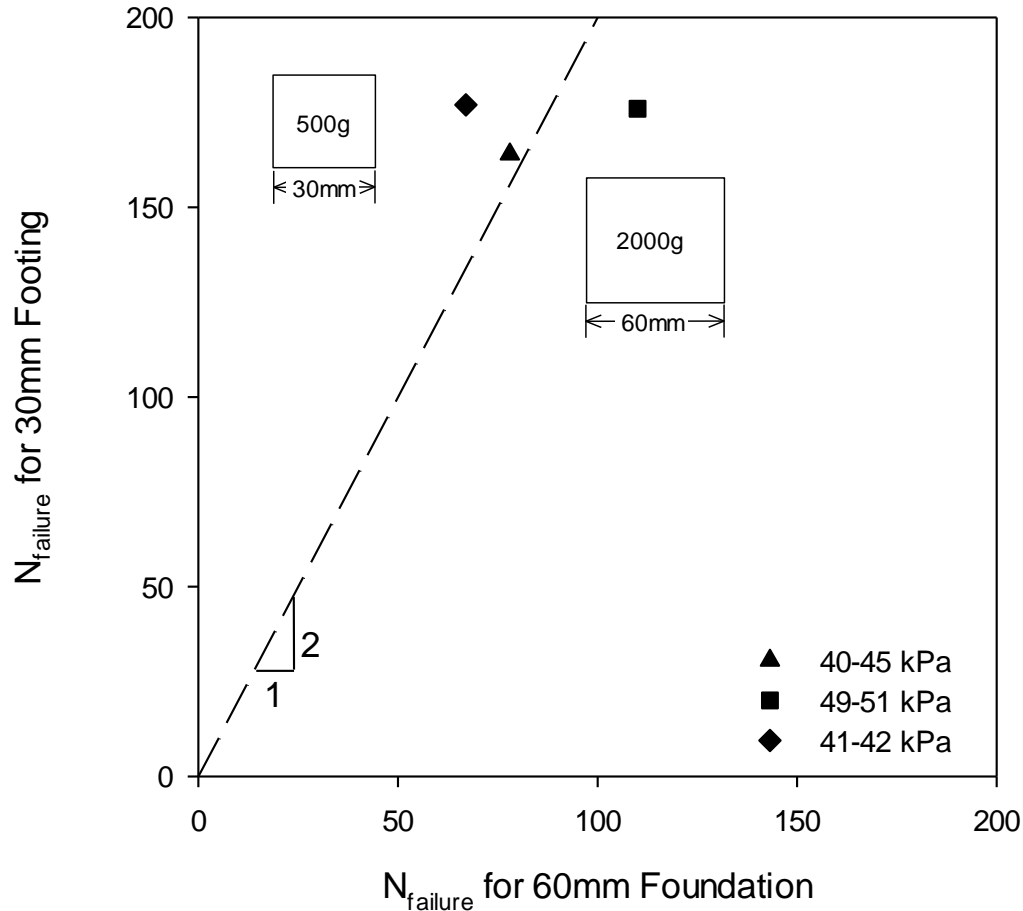


Figure 18 Bearing Capacity Modelling of Models Correlation

As a result of this variance in shear strength between pairs of models, a better comparison in this case is the second method of evaluation. This evaluation is performed by comparing the $N_{failure}$ predicted by Terzaghi's equation (Equation 7B), modified for the conditions of the test. Table 5 gives a summary of the testing scheme including w , associated c , and q . The maximum applied uniformly distributed load along the length of the footing is known from the mass of the footing and the area of the footing as a function $B_{failure}$ for a FoS equal to 1.0. The required N to achieve the instability calculated by the Terzaghi's equation is also given as predicted $N_{failure}$.

Figure 19 plots the observed $N_{failure}$ from Table 4 with the predicted $N_{failure}$ from Table 5. The figure also presents a 1:1 line on which all data points should plot for good agreement between the observation $N_{failures}$ from the model and the predicted $N_{failures}$ for the prototype. The closed symbols are the 60mm footings and the open symbols are the corresponding 30mm footings. Comparing the data to the 1:1 line shows the failures corresponded within an average range of 10% of the predicted values.

Table 5 Summary of Bearing Capacity Test Results

| B_{model} (mm) | w (%) | Predicted c (kPa) | Predicted q (kPa) | Predicted $B_{failure}$ | Predicted $N_{failure}$ |
|---------------------|----------|----------------------|----------------------|----------------------------|----------------------------|
| 60 | 33.9 | 45 | 231.4 | 4.7 | 79 |
| 30 | 34.9 | 41 | 210.8 | 4.3 | 144 |
| 60 | 32.6 | 51 | 262.2 | 5.3 | 89 |
| 30 | 32.9 | 49 | 251.9 | 5.2 | 172 |
| 60 | 34.5 | 42 | 215.9 | 4.4 | 74 |
| 30 | 34.6 | 42 | 215.9 | 4.4 | 148 |

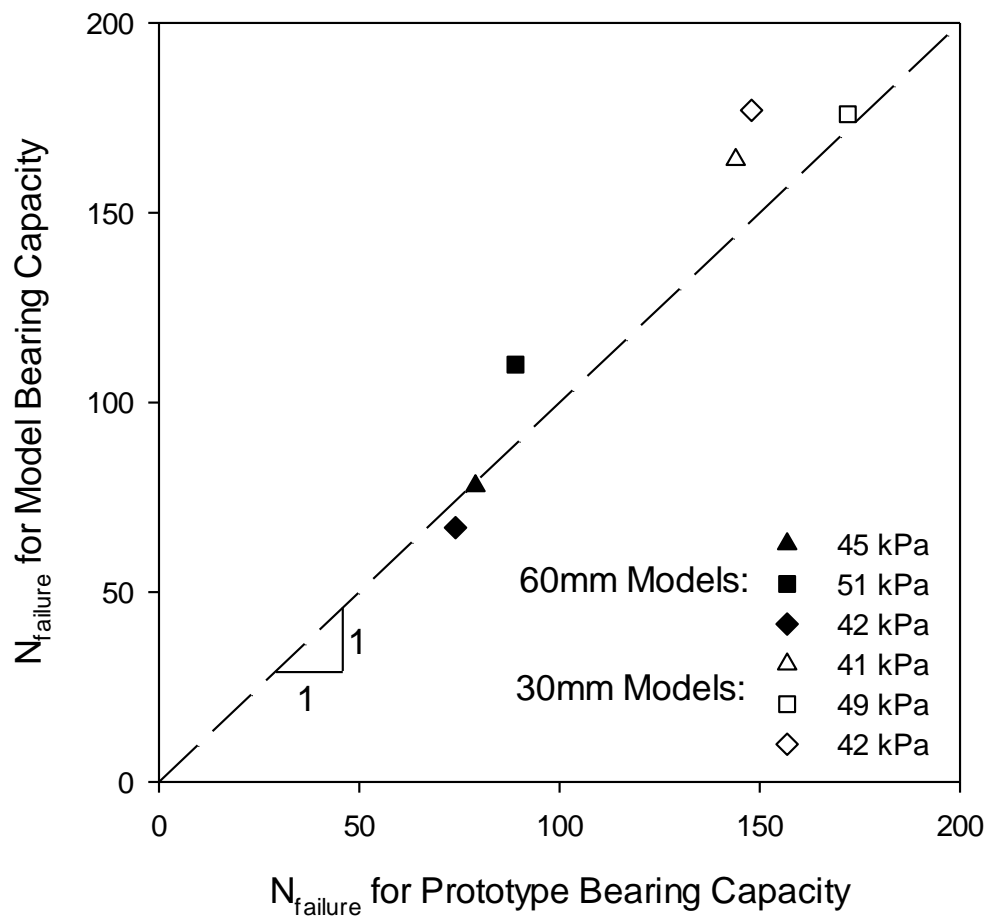


Figure 19 Observed Bearing Capacity Correlation with Theoretical Prediction

The variation in the observed N at failure is likely a result in inconsistent behaviour of the foundations during failure (Kimura et al., 1985). Variable rotation of the footing during the failure mechanism produced some variation in the expected results.

2.4 Summary

The results obtained by testing models with two different scales obtained proportional results and demonstrate the desired result of a modelling of models scheme of tests. The simpler couplets of slope models gave very good agreement while the more complex bearing capacity problem presented more variation in failure. Both models were scaled using the techniques described and produced consistent data in accordance with the scaling laws. The ability to properly scale models using these scaling laws and the methodology and analysis employed produces confidence in their future use. The models' behaviours were also consistent with the predicted limit equilibrium solutions determined from both Taylor's slope stability charts and Terzaghi's bearing capacity equation. This success demonstrates that the more difficult task of producing the behaviour of prototype structures was also achievable in the centrifuge. The success of the tests to produce proportionate and accurate model behaviour confirms the application of these scaling laws for further research.

These results produced confidence in the ability to not only scale between models but also to model prototypes using known analytical methods. The behaviour of the slopes models clearly indicates the success of the scaling of idealized geotechnical structures with close agreement, at various scales, with analytical solutions. Variations in the bearing capacity tests indicate that a new method for tests with similar mechanisms should be employed. For tests that are sensitive to variations in modes of failure the use of actuators to apply loads and improve repeatability of failure mechanics and results should be employed in the future.

The described methods and results confirm RMCC's ability to employ this centrifuge in both teaching and for future, and more complex research; either to produce data to calibrate numerical models, determine the behaviour of prototype structures, or to observe and describe mechanisms in general soil structure behaviour. Knowledge gained in methodology and development of processes for analysis of the results will continue to improve the accuracy of the testing methods to produce high quality modelling of a variety of geotechnical prototypes and detailed data describing their behaviour. This ensures the development of RMCC's educational scope and range, and value of future research projects.

Chapter 3

Physical Modelling of Wetting-Drying Cycle Applied to Infrastructure Constructed in Expansive Soils

3.1 Introduction

Expansive soils add another layer of complexity to the already complex problems presented in engineering geotechnical structures. These fine grained soils respond to changes in moisture content with significant volumetric strain. Swelling and shrinking behaviour occurs because they are composed of certain minerals (such as illite and montmorillonite) whose chemistry and physical geometry renders them susceptible to weak bonding with water molecules and gives them large surface areas relative to their volume, creating greater opportunity for this bonding to occur (Lin, et al 2013, Puppala, et al., 2013). The resultant indicative soil characteristics are that fine grained soils have high plasticity and their volumes are very reactive to the presence of water (Muntohar, 2003). Expansive soils are commonly found in arid climates in numerous regions around the globe. They are also associated with the unsaturated zone (Fredlund, 1996, Ito et al., 2014) which provides conditions for large cyclic changes in water content to occur. These cycles, ranging from near saturation to dry soil are produced as a result of infiltration, and evaporation and evapotranspiration caused by extreme individual weather events such as intense rainfalls and droughts or normal seasonal periods of cumulative weather effects. Expansive soils responding to moisture fluxes can produce significant volume changes which, in turn, can fail geotechnical structures constructed in such clays (Gadre., et al 1994, Fredlund, 1996).

The effects of weather and climate are the main driving force that causes moisture variation leading to shrink/swell behaviour in expansive soils (Fredlund, 1996). Infiltration, evaporation or evapotranspiration acting at the surface and variations in the water table at depth lead to moisture migration within the unsaturated zone as shown in Figure 20 (Fredlund et al., 2012, Ito et al., 2014 Wilson et al., 1997). Figure 20 shows a column of expansive soil undergoing swelling as a result of infiltration (left) and shrinking as a result of evaporation (right). Two soil elements, one near the surface and another deep within the soil, show the impact of confining stress on the degree of volume change produced. These changes in volume can be understood as the volumetric strain (ϵ_v) changing as a function of matric suction ($u_w - u_a$) which varies with infiltration or evaporation of moisture in soil. The relationship between volumetric strain and suction (m^2_s) is a function of the depth and confining stress from the overlying soil (Fredlund et al., 2012). Figure 21 shows how the infiltration of water into the voids within the soil changes the soil suction. When infiltration occurs, the wetting front moves down through the soil the suction is decreased to zero as the voids become completely saturated, and the maximum change in volume occurs for that depth. Conversely, if evaporation of moisture from the soil into the air occurs the voids become less saturated. The resultant change in the degree of saturation produces an increase in suction, $u_a - u_w$ and subsequently the volume decreases. The rate and depth of infiltration, and evaporation or evapotranspiration are controlled by a combination of weather

conditions, primarily, rainfall intensity and duration, wind speed, humidity, and temperature, and soil and surface conditions. These aspects must be considered to quantify their effects on the soil and subsequently the associated structures (Puppala et al., 2011).

If infrastructure constructed in expansive soils is subjected to differential displacements as a result of these volumetric strains, the results can be devastating. The catastrophic damage of swelling soils is frequently seen on lightly loaded geotechnical structures such as shallow foundations for houses and other small buildings, embankments and slopes, roadways (Figure 23), pipelines, and other utility and transportation corridors (Gadre et al., 2004, Ito et al., 2016, Lin et al., 2013, Roodi et al., 2014, Take et al., 2002). Although seemingly insignificant on their own, cumulatively, they are comparable to natural disasters. While the subsequent failures are usually only striking to those directly involved (McCudden, 2001) the enormous cumulative cost, effort, and safety problems caused by these soils (Fredlund, 1996) makes understanding their characteristics, and the effects and mechanisms they produce in geotechnical structures a critical area of knowledge for geotechnical engineers who work in these environments (Chowdhury et al., 2016, Plaisted et al., 2013, Zornberg et al., 2009).

In order to account for shrink/swell behaviour in geotechnical design, the swelling potential of a soil is characterized. Various methods of quantifying the behaviour of swelling soils exist, including free swell, confined swell, and shrinkage limit tests (Gadre et al., 1994, Fredlund, 1996, Fredlund et al 2012). The benefit of these tests is that they quantify certain behaviours and provide indices for soil classification. Limitations of these tests include their inherent artificiality (Lin et al., 2003) and the limited sample dimensions, representing only a small portion of a soil profile (Plaisted et al., 2013). More advanced swelling tests allow for quantification of the swelling potential over the range of expected stress and boundary conditions using element tests (Siemens et al., 2007, Powell et al., 2013, Lim et al., 2013, Lim et al., 2016). Use of index or advanced testing methods is limited by the elemental nature of the experiments. Thus, the results only provide a small portion of the information required to study and understand the larger mechanics at work in soil-structure interaction problems. Numerical models (Ito et al., 2016) and analytical methods (Fredlund, 1996) can be used to predict the behaviour of larger structures but rely heavily on input from field data. Field studies are rarely produced due to the cost of equipment and the duration of monitoring required for the often long timescales associated with seasonal or annual weather cycles. Following monitoring, the results can be used in numerical models, however, the few measurements available may or may not be enough to calibrate and validate swelling behaviour (Ito et al., 2016, Roodi et al., 2016, Take et al., 2002). Thus, another method of producing information on the behaviour of these geotechnical problems is required.

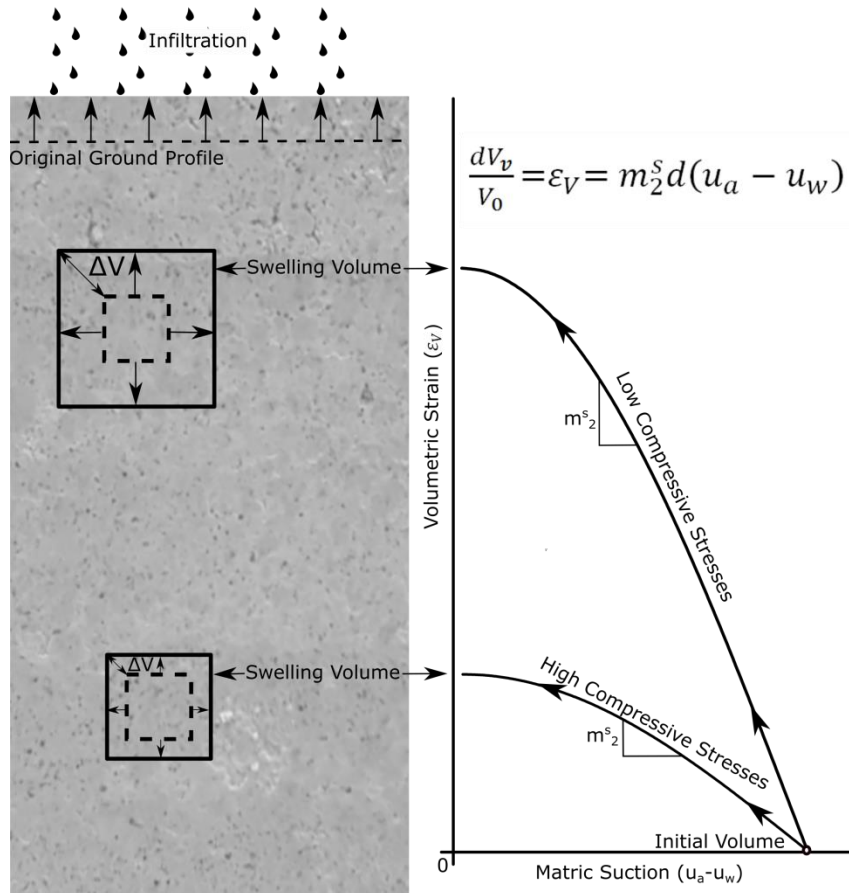
Physical modelling in a geotechnical centrifuge is less demanding on resources, faster, and can produce more comprehensive data than the previously mentioned methods. Physical modelling of swelling soils can be done relatively rapidly with significantly lower costs while providing a larger bank of data and a more detailed understanding of soil-structure interaction behaviour and material effects (Take et al., 2002, White, 2008). Centrifuge modeling of swelling soils by Gadre and Chandrasekaran (1994) as well as by Plaisted and Zornberg (2013) demonstrate that the use of the centrifuge scaling laws is valid for an expansive soil. The salient benefit of using a centrifuge is that it includes an increase in the soils' self-weight, proportional to a much greater depth of soil, which is critical to the understanding of its behaviour (**Figure 20**). By scaling gravity, physical models apply identical stresses on the scaled geometric points in the sample as those that the prototype soil would be experiencing

(Roscoe, 1970). This is critical because the behaviour of expansive soils, as with other geomaterials, is influenced by two stress state variables, confining stress as well as the aforementioned suction. Confining stress is directly impacted by the applied stresses from self-weight of overlying soil (Fredlund, 1996, Ito et al., 2014). The ability of this method to produce the same results in a single test and sample as are produced by multiple tests at normal gravity with various surcharges provides a confident basis for the practice modelling of more complex models comprehensively rather than in multiple uncoupled tests. These benefits make the development of physical modelling methods for swelling soil influenced structures an important field of study.

An idealized model is given to understand the problem of modelling these structures and develop analysis and design methods. A two-lane, paved road constructed over a swelling soil subgrade (Figure 22) is a representative structure that demonstrates the common failure mechanism (Plaisted et al., 2013, Puppala et al., 2011, Roodi et al., 2016) of differential expansion and shrinkage as a result of swelling soils' changes in volume as they interact with the changing atmospheric conditions. Figure 22 shows how this differential volume change produces compressive strains in the road surface during infiltration and tensile strains during evaporation. Continued wetting-drying cycles have resulted in linear cracking of road surfaces (Figure 23) and desiccation of the soil fabric, resulting in further damage to the structures (Roodi et al., 2016, Zornberg et al., 2009, Puppala et al., 2011). The mechanism of failure has been regularly observed and studied in roadways in Texas (Zornberg et al., 2009) as well as in Oklahoma (Lin et al., 2013) and Saskatchewan (Chowdhury et al., 2016), as well as many regions associated with expansive soils. Several case studies of roads suffering from these failures as a result of the expansive soils they are constructed of and on have been conducted (Zornberg et al., 2009, Puppala et al., 2011, Puppala et al., 2013); however, cost, difficulty with instrumentation, need for repeatability to confirm observations, as well as variability from road design, soil composition, and incidental effects from vegetation conspire against using case studies exclusively to examine this failure mechanism. Physical modelling is the ideal candidate to fill this gap in the study of roads constructed on swelling soils.

By combining the success of centrifugal modelling in examining the behaviour of swelling soil across various stratum with well controlled and representative models of road designs, and employing wetting and drying controls and monitoring within a centrifuge, useful methods can be developed and valuable data can be produced. These results can provide further understanding of the behaviour and mechanisms associated with these structures. This chapter lays a framework for methods and procedures to be used in expansive soil centrifuge models at RMCC as well as presents a series of paved road structures constructed on expansive soil and subjected to cyclic wetting and drying. The results demonstrate the ability to replicate the phenomenon observed in the field, provide data to better understand the failure mechanism (Roodi, et al., 2016, Puppala et al., 2011, Zornberg et al., 2009) and provide a basis for further research areas by producing successful methods to model and measure the effects of expansive soils subjected to wetting and drying.

A: Swelling of Expansive Clay



B: Shrinking of Expansive Clay

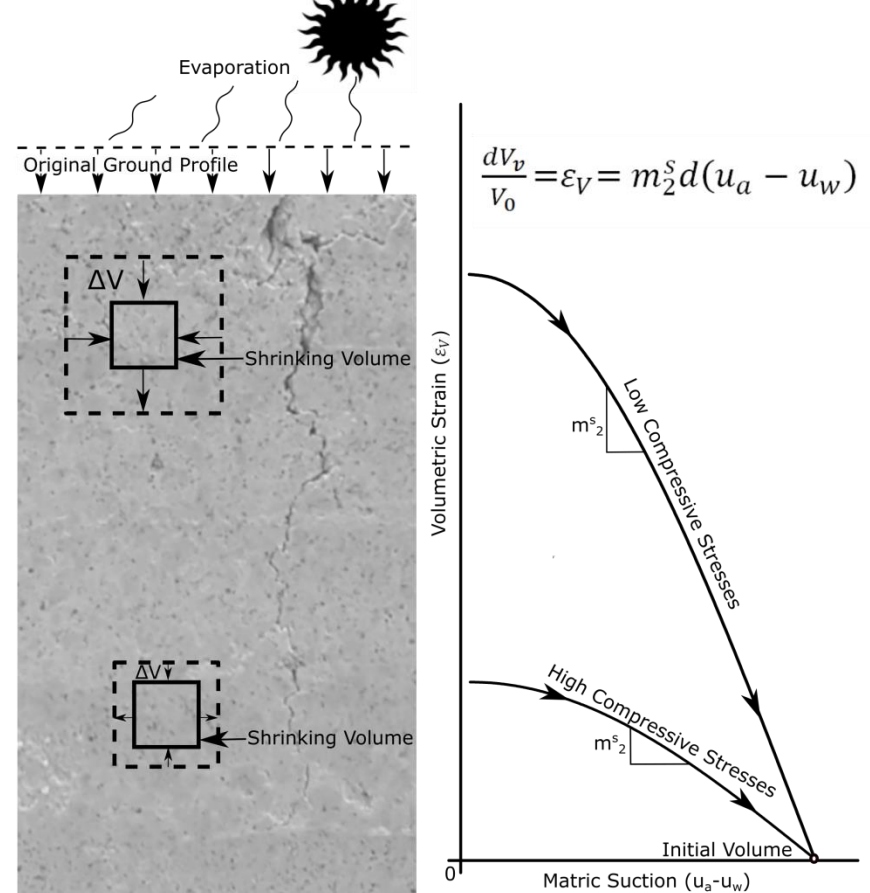


Figure 20 Seasonal Wetting and Drying Producing (A) Swelling and (B) Shrinking Behaviour in Expansive Clay with the Relationship between Matric Suction and Void Ratio Shown with Consideration of Compressive Stresses

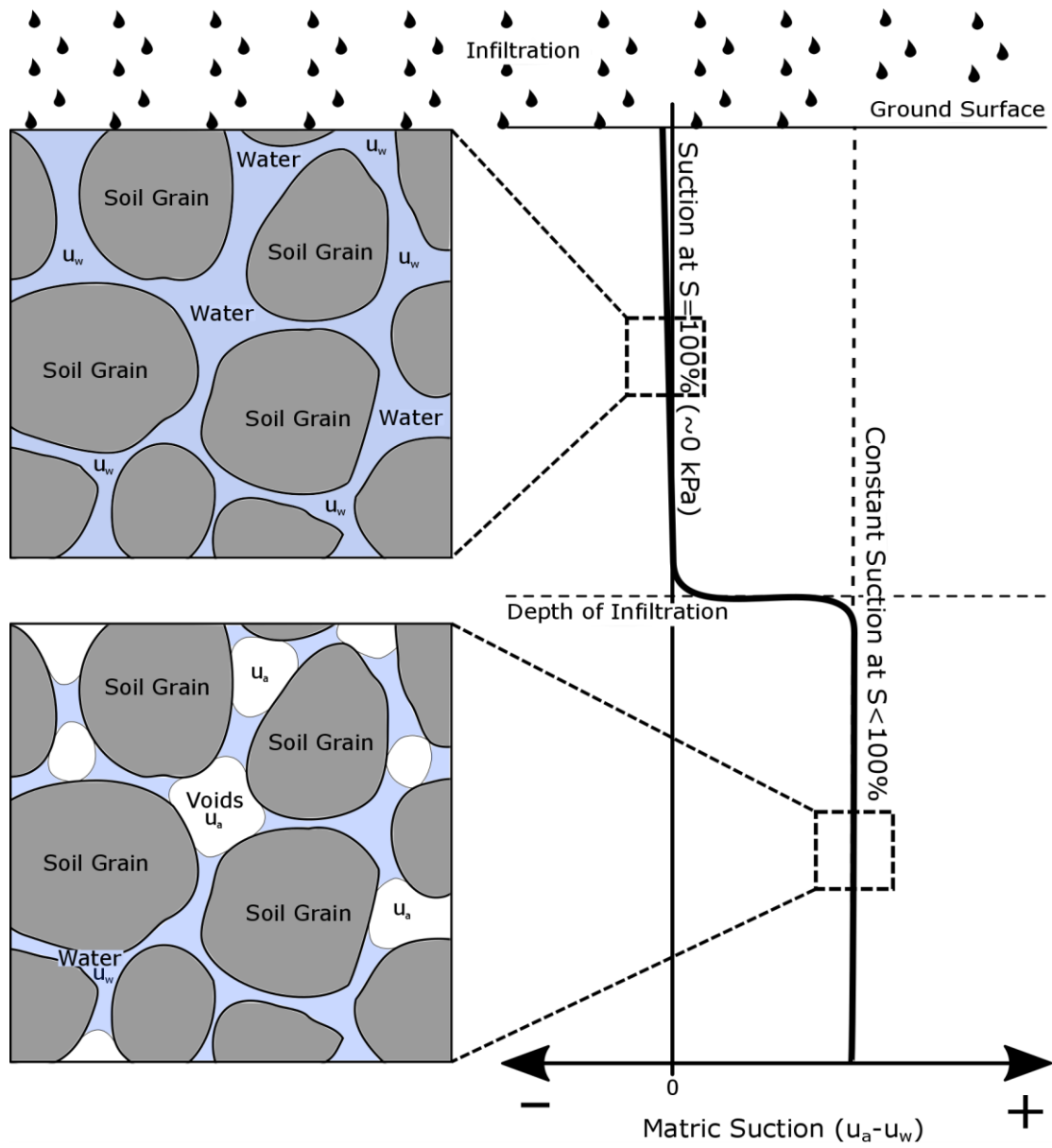
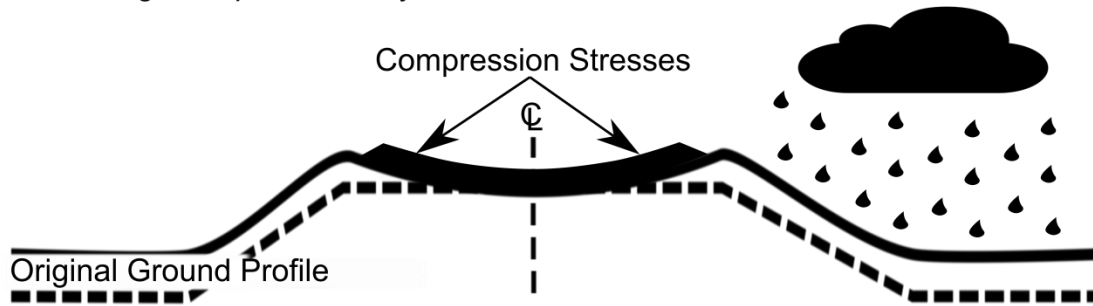


Figure 21 Effect of Infiltration on Suction Profile

A: Swelling of Expansive Clay Road Profile



B: Shrinking of Expansive Clay Road Profile

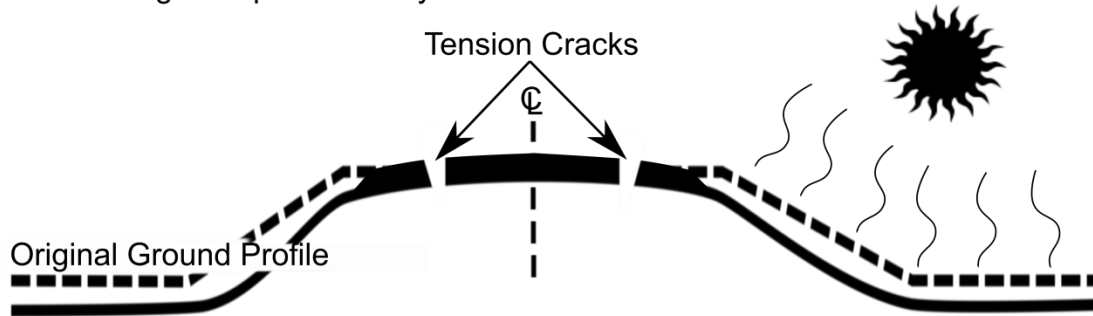


Figure 22 Failure Mechanism for Paved Road in Expansive Soil (after Zornberg et al., 2009)



Figure 23 Road Damage Caused by Expansive Soil (Coating Industry News, 2016)

3.2 Theory

Physical modelling of a structure constructed on swelling soil in a geotechnical centrifuge requires considerations of not only the soil and mechanisms associated with its behaviour but also an understanding of the application of scaling laws in the centrifuge. By understanding the theory of centrifuge testing, useful modelling methodology and reliable results are produced

3.2.1 Centrifuge Scaling

The effects of stress on expansive soils are shown in in **Figure 20** and as such, physical modelling attempt must carefully take confining stresses into account. To generate the required stresses in the model to simulate prototype behaviour the force of gravity (N_g) is increased in proportion to the reduced scale of the model (Madabhushi, 2015, Roscoe, 1970).

A geotechnical beam centrifuge is employed to apply a stress gradient to a soil model. The centrifuge achieves this by employing centripetal force produced by rapid rotation. Equation 12 describes the relationship between the force of gravity (N_g) as a result of acceleration on a body due to the angular velocity ($\dot{\theta}$) produced by the rotation of centrifuge, and the distance from the point of rotation (r). By increasing the rotational speed and therefore angular velocity, an increase in the force of gravity is applied to the model across its depth.

$$N_g = r \dot{\theta}^2 \quad \text{[Equation 12]}$$

By applying more acceleration with the centrifuge (according to Equation 12), stress is increased proportionally throughout the model depth. Figure 24 shows the effect of increasing the force of gravity (N_g) on the stresses from density (ρ) of the soil mass within the model using Equation 13. Using Equation 13, a stress produced by the overburden of soil can be calculated.

$$\sigma = \rho N_g z \quad \text{[Equation 13]}$$

By scaling the force of gravity with this technique, the forces in the model increase proportionally with depth. Increasing the acceleration and therefore increasing the body forces throughout the depth of the model (Figure 24) achieves stresses within a scaled model to the desired prototype dimensions. The model can now be used to represent the prototype by applying the requisite stresses in the model at the same geometric points in the prototype. This means that the behaviour of the mechanisms in the model that are governed by stresses in the soil as a result of soil weight and depth are correctly reproduced.

Scaling must be done with a good understanding of the mechanisms being used to create the requisite effects. Because the effective radius for each soil element across the depth of the model changes as the element's distance to the center of rotation changes, the applied N increases slightly with depth through the model (Figure 24) in accordance with Equation 12. This produces some small artificial distortions in the stresses, which are a function of N (Equation 13), especially at the lower portions of the model. However, in the upper zone of interest of the model this distortion is minimal and even at the extremes it varies no more than 5%. Fredlund (1996) and Lin (et al., 2016) observe that the overburden stress and degree

of infiltration typically limit the depth at which volumetric strains as a result of infiltration/evaporation are observed to 2.5m. The expansive zone of the soil profile (Figure 24), that is, the region of the model where the largest responses to infiltration and evaporation are expected to occur, is the portion of the model which has the most consistent scaling stresses. The lower portion of the model where the differences are greater is not expected to experience significant suction changes and associated volume changes and so the impact on the whole model's behaviour caused by the variation in that portion of the model will be minimized. Table 6 shows a comparison between the stresses (assuming a soil with a density of 1.72 g/cm^3 at 1g) at like geometric points (a., b., and c in Figure 24) in the model and prototype as well as the nominal N for the centrifuge where the model stresses exactly match the prototype stresses. Similar stresses with some minor distortion from the gravity field variation are produced in both the model and the prototype. Above the depth of the centrifuge's nominal N the stresses are slightly reduced and below they are slightly increased (Table 6). Because the stresses are equivalent for like geometric points at key locations (a., b.) behaviour of the model is anticipated to behave as a prototype would under similar applied seasonal wetting and drying cycles without the distortions indicated by the corrected values having any impact.

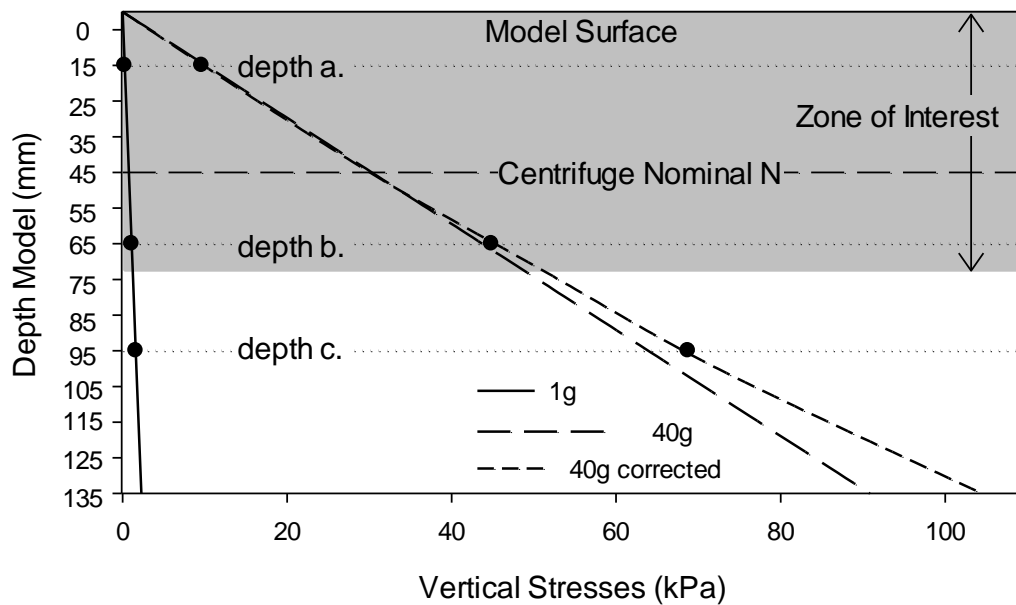


Figure 24 Stresses within Soil Profile in the Centrifuge

Table 6 Comparison of Stresses at Geometric Control Points in Model at 40g and Scaled Prototype

| Geometric Control Point | Depth _{Model} (mm) | Depth _{Prototype} (m) | σ_{Model} ¹ (kPa) | $\sigma_{\text{Prototype}}$ ² (kPa) | Difference (%) | $\Delta\sigma$ (kPa) |
|-------------------------|-----------------------------|--------------------------------|--|--|----------------|----------------------|
| a. | 15 | 0.6 | 10.1 | 9.6 | -5.0 | 0.5 |
| Nominal | 45 | 1.8 | 30.3 | 30.3 | 0 | 0 |
| b. | 65 | 2.6 | 43.7 | 44.8 | 2.5 | 1.1 |
| c. | 95 | 3.8 | 63.9 | 68.9 | 7.5 | 4.8 |

¹At 40g

²Corrected for distortion from gravity field

A further benefit of centrifuge testing is reduced time scaling (Garnier et al., 2007). For tests involving infiltration, which is a squared function of distance, time of the model scales at N^2 times that of the prototype. As a result, modelling conducted at 40g behaves at a rate comparable to 40^2 (1600) times faster than that of a prototype. The resultant process allowed for a two-lane paved road symmetrical along its centreline, with geometrical modifications employed to observe the effects of changes to the road's construction.

3.3 Material, Testing, and Data Analysis Methodology

Construction and testing of a model was conducted in such a way as to be able to achieve repeatability in tests and ensure that a simplified and characteristic model of a typical prototype light geotechnical structure was achieved. The resultant process allows for modelling of a road based off of a simple, two lane, road design, symmetrical along its centerline, with some modification options employed to observe the effects of changes to the road's construction.

3.3.1 Model Design

In order to model a typical road structure and design, the scale of the model is first determined. Figure 25A and B show the prototype and model road used in physical models reported in this chapter. The dimensions of the road are based of typical geometry of a two-lane paved road, which are mirrored about its centerline (⊥). By applying 40g to a model it can represent the prototype design at 1/40th scale. The travelling surface of the road, 3.7m from the centerline in prototype and 92.5mm in the model, is typical of a roadway with paved lane and paved shoulder. The road has a sloped embankment which descends down to the ground surface. Two modifications to the road design are considered, which are an unpaved shoulder and a ditch. The exposed shoulder reduces the paved portion of the road to 3.3m (82.5mm) from the centreline with a 0.4m unpaved shoulder and ditch with a depth of 0.4m below the ground surface at the base of the slope. This allows observation of the effects of variation in surfacing and pooling water in ditches on the road's behaviour.

The model is of a road of typical construction, symmetrical along its centerline, mirrored on the fixed left boundary of the cradle. The 300mm width of the cradle is divided into approximate thirds with the first zone being comprised of the permeable far field portion of the model bounded by the fixed wall of the cradle on the right, the second zone containing the shoulder, slope, and ditch which transitions to the third, the impermeable surfaced road bounded on the left by the wall of the cradle. This allows the behaviours of the three zones to be roughly categorized as the far field of the ground on the right which provides a "normal" behaviour of the soil profile without the influence of the road, the road portion which does not directly interact with the applied wetting and drying fluxes on the left, and the transition zone between the two. The transition zone is in the middle where the differential movements which are expected to impact the structure can be observed. Discussion of the results and interpretation will use these general zones as reference for characteristic behaviour.

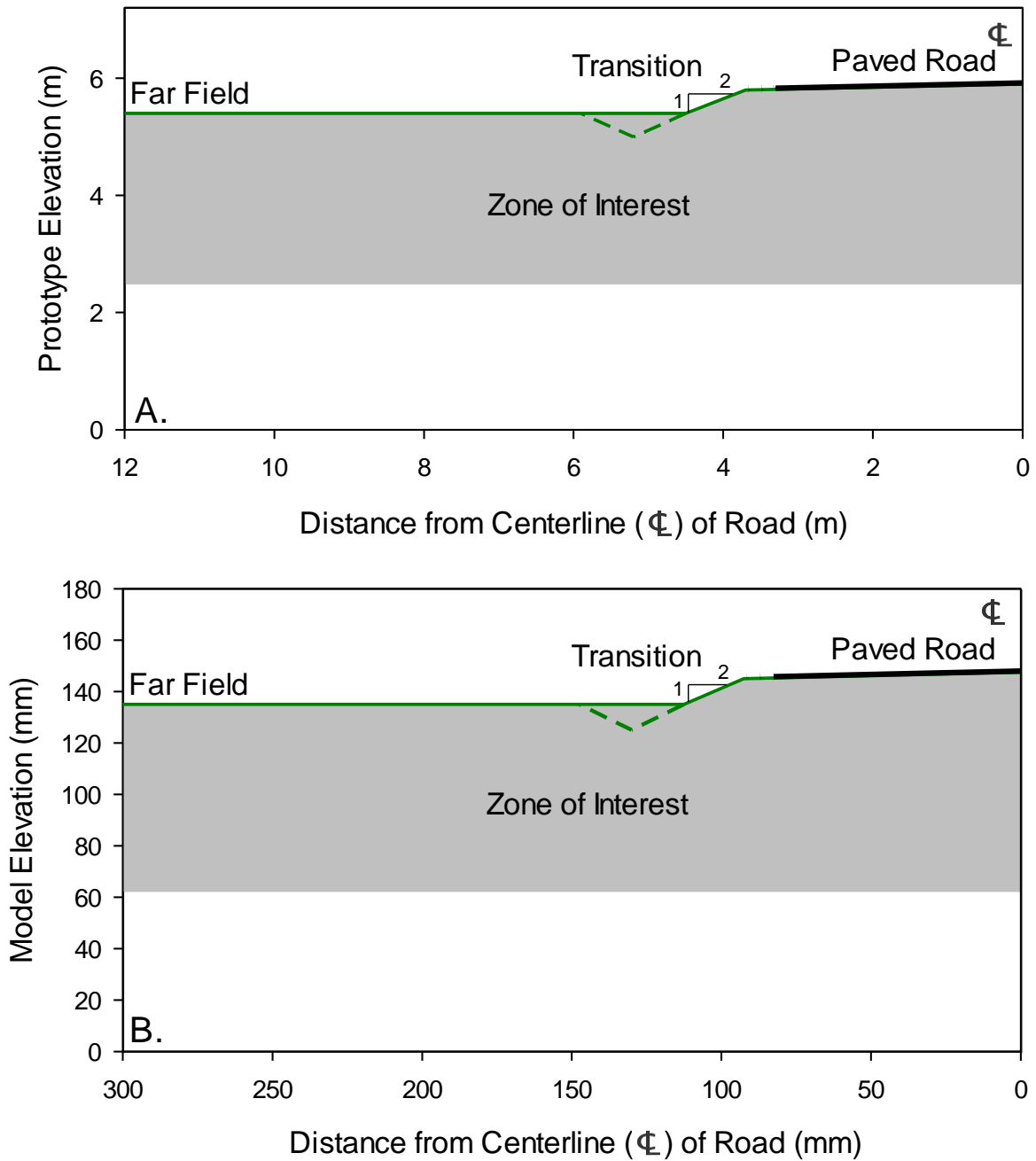


Figure 25 Prototype (A) and Model Design (B)

3.3.2 Soil Characterization

Expansive soils' properties vary greatly, even within small regions (Puppala et al., 2013) which contributes to the difficulty of repeatability in testing (Roscoe, 1970, Schofield, 1980) and can lead to results that are only applicable to unique locations or material properties (Fredlund, 1996). Because of these challenges, a remolded soil composed of a combination of readily available and standardized materials, mirroring expansive material properties, is used for the construction of the models in this chapter.

The model encompasses the upper portion of the unsaturated zone of soil profile including the entire expansive zone. To ensure that the soil mixture design and properties was characteristic of expansive soil profiles it was compared to a typical profile of a known expansive soil (Fredlund et al., 2012). Figure 26 shows a soil profile composed of Regina Clay (Fredlund et al., 2012). The profile shows a relatively uniform profile to 6m depth in what would be typically expected to be the expansive zone. Expansive soils are usually found in arid regions and it is not uncommon for the water table to be far below the expansive zone. Because of this, and the high capillary rise associated with fine-grained clays, a water table was not constructed within the model.

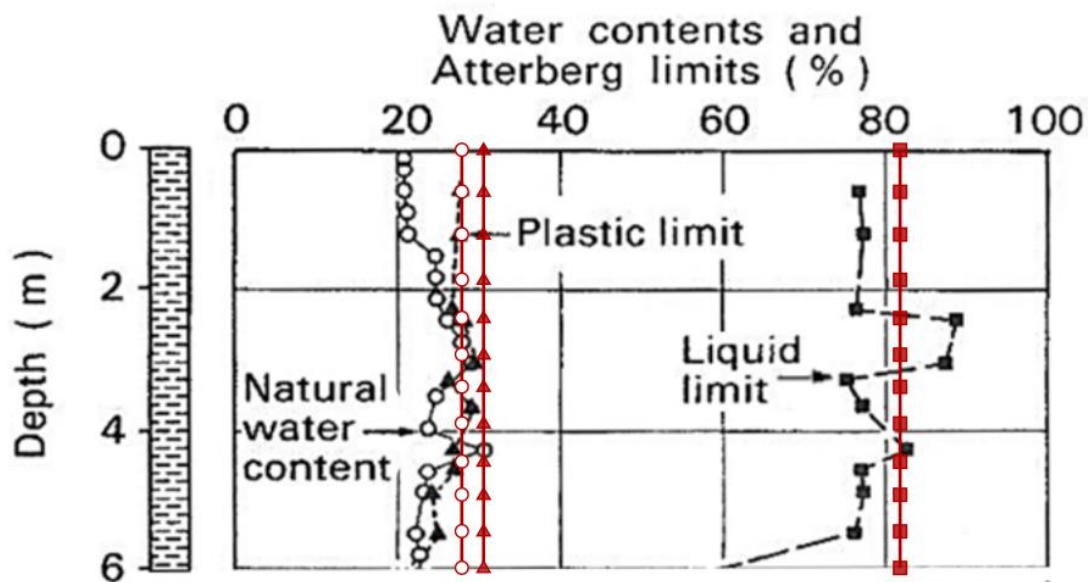


Figure 26 Typical Expansive Soil (black) (Fredlund et al., 2012) and 90% Kaolin and 10% Bentonite Soil Mixture (red) Properties

The remolded soil design chosen was composed of Speswhite Kaolin clay, a relatively non-expansive soil, is combined with MX-80 bentonite clay, a very expansive soil, at ratios of 90:10 Kaolin:Bentonite by mass. The resultant soil has material properties and in-situ values representative (Figure 26) of expansive soils found around the world as listed in Table 7. From the grain size distribution (Figure 28) and consistency limits the soil is classified as a high-plasticity clay (CH) soil according to the Unified Soil Classification System (ASTM D2487, 2011). These material property values are also consistent with those observed by

Muntohar (2003) in a comparable Kaolin and Bentonite mixture. The composite clay provides significant swelling potential (42%) with a plasticity index (PI) of 52%. The other values also all fall within the ranges expected to be found in expansive soils. This provides confidence not only that the soil will produce measurable results within a model but that those results will be comparable to those of a real-world prototype. Simultaneously, the soil mixture will allow for repeatability of the tests conducted without interference from variability associated with naturally occurring soils.

Table 7 Expansive Soil (90% Kaolin and 10% Bentonite) Material Properties Compared with Typical Values

| Material Property | 90/10 Kaolin Bentonite | Typical Range ⁵ |
|--|------------------------|-----------------------------|
| Plastic Limit | 30.3% | 15-45% |
| Liquid Limit | 81.9% | 30-95% |
| Plasticity Index | 51.6% | 20-60% |
| Optimum Moisture Content ¹ | 30.6% | 15-30% |
| Maximum Dry Density ¹ | 1.35 g/cm ³ | 1.30-2.00 g/cm ³ |
| Shrinkage Limit Water Content ² | 28.8% | NA |
| Volumetric Strain ³ | 42% | 10-55% |
| Free Swell ⁴ | 6 ml\2g | N/A |

¹Proctor test conducted in accordance with ASTM D698-12e2 (Figure 2.5)

²Shrinkage test (Appendix D) conducted in accordance with Fredlund et al., 2012

³Volume strain observed from liquid limit to air dry volume (Lin et al., 2013)

⁴Test conducted in accordance with Prakash et al. 2004

⁵As reported by Chowdhury et al., 2016, Puppala et al., 2013, Lin et al., 2013, Fredlund et al., 2012

To achieve consistent model behaviour, the mineral composition not only has to be consistent but also its physical and mechanical preparation. The target water content and density was chosen to produce high swell potential (Puppala et al., 2011, Puppala et al., 2013) while still remaining moist enough to be practically workable. For all models, the test soil was mixed to a target gravimetric water content of 28% and compacted to a target dry density of approximately 1.34 g/cm³ (as described in section 3.3.4). This is approximately 92% of the optimum moisture content (OMC) (Figure 27) of 30.6%. The water content is also below the shrinkage limit which reduces the amount of shrinkage which might take place as a result of moisture loss during sample preparation, model construction, and installation within the centrifuge cradle. The dry density and water content of the compacted soil mixture give a total density of 1.70 g/cm³ with a degree of saturation of 77%. With this well-defined soil, consistent models can be constructed for testing.

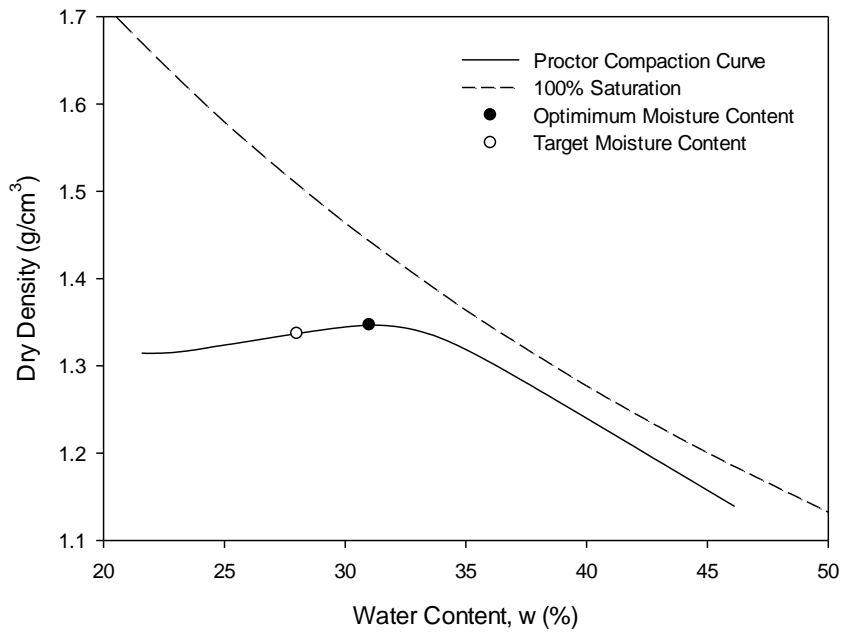


Figure 27 Proctor Compaction Curve for Expansive Soil (90% Kaolin and 10% Bentonite)

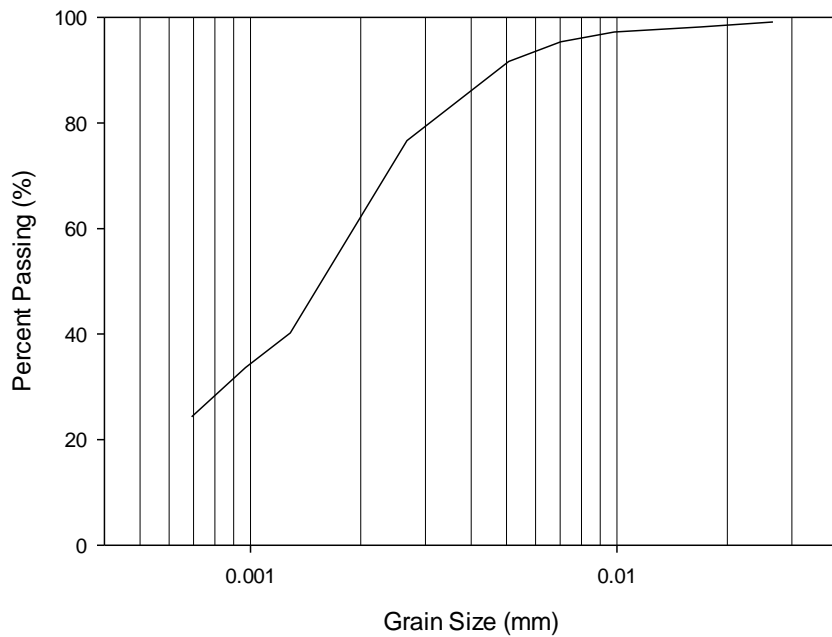


Figure 28 Grain Size Distribution for Expansive Soil (90% Kaolin and 10% Bentonite)

3.3.3 Test Soil Preparation

Soil preparation generally followed established methods to achieve a consistent initial moisture and density profile. For each road model, a mixture of 7000g of dry soil is mixed to a target water content of 28% and a final volume of approximately 5200cm³. This volume corresponds to a block of compacted soil 17cm tall with an area equal to that of the cradle (30cm x 10cm). This allows for some loss of material in the mixing process and for the surface layers to be removed to create the required model design.

A mixture at the target water content with an even distribution of the two soil types is produced by mixing, by dry mass, 90% Speswhite Kaolin with 10% MX-80 Bentonite. Due to the size of the mixing bowl, the mixing is typically done in two batches for each model mixture with 3500g total mass of soil for each batch; 350g of bentonite is added by thirds to 3150g of kaolin.

Once the soil has been measured into the bowl, the soil is then mixed dry until the bentonite is no longer visible in the kaolin. To produce a uniform soil both hand mixing and mechanical mixing are used. To achieve the 28% gravimetric water content, 980g of water is added to the bowl and again mixed by hand to minimize aeration of the fine clay particles when mixing in the machine. Once the water has been preliminarily mixed with the soil using a large steel spreader knife, the bowl is placed in the stand mixer which is fitted with a large whisk attachment. The whisk was found to reduce clumping and produce a more uniform soil mixture than the mixing paddle at this water content. The soil is mixed for approximately three minutes, one minute at each of the speed settings, beginning with the lowest speed, and periodically scraping the sides and bottom of the bowl with a steel spreader knife to expose dry areas or break up wetter clumps. Further mixing past this point was found to only compact soil against the sides of the bowl and not to improve the uniformity of the soil mixture or reduce clump sizes. Figure 29 shows a typical soil after mixing with the whisk for three minutes. A visual inspection ensures no large clumps or dry areas remain and clumps larger than 8mm across are broken up by hand. The two soil batches are combined and placed in a sealed container for a minimum of 16 hours to allow moisture to distribute evenly throughout the mixture. Soil samples are taken during construction of the model to determine the gravimetric water content and ensure that the target water content is achieved.



Figure 29 Mechanically Mixed Soil

3.3.4 Model Construction

A method that allows for consistent construction of an unsaturated soil model was developed to ensure that the model would not undergo significant shrinkage prior to swelling. A consolidated, saturated sample was rejected because during the first drying cycle, shrinkage produced large voids around the model and allowed flow around the model rather than through the soil. Instead, the physical model is constructed from a compacted block with constant initial moisture content and density. This allows the soil to be prepared to a target void ratio and degree of saturation, improving behaviour of the model and consistency between tests.

The physical model is compacted in a wooden form with the same area dimensions as the cradle (Figure 30). The interior walls of the form are sprayed with a silicon lubricant prior to compaction to minimize disturbance during removal. Due to the high compaction energy, clamps around the form are secured to augment the screws used to hold the form together. Compaction energy was selected to replicate the $600 \text{ kN}\cdot\text{m}/\text{m}^3$ applied in the Standard Proctor test. Therefore 65 blows with a proctor hammer are used for each of the six lifts. A second consideration is compacting against the flat edges of the form. Because the wooden form is rectangular rather than round (Figure 30) a 60mm square piece of aluminum is used for 35 of the blows to ensure compaction is also achieved in the corners and along the edges of the compacted soil. The Proctor hammer is used alone for the remaining 30 blows (alternating square and round, 15/15/15/15/5). The resultant block of compacted material is now ready to be cut to the model road design geometry.

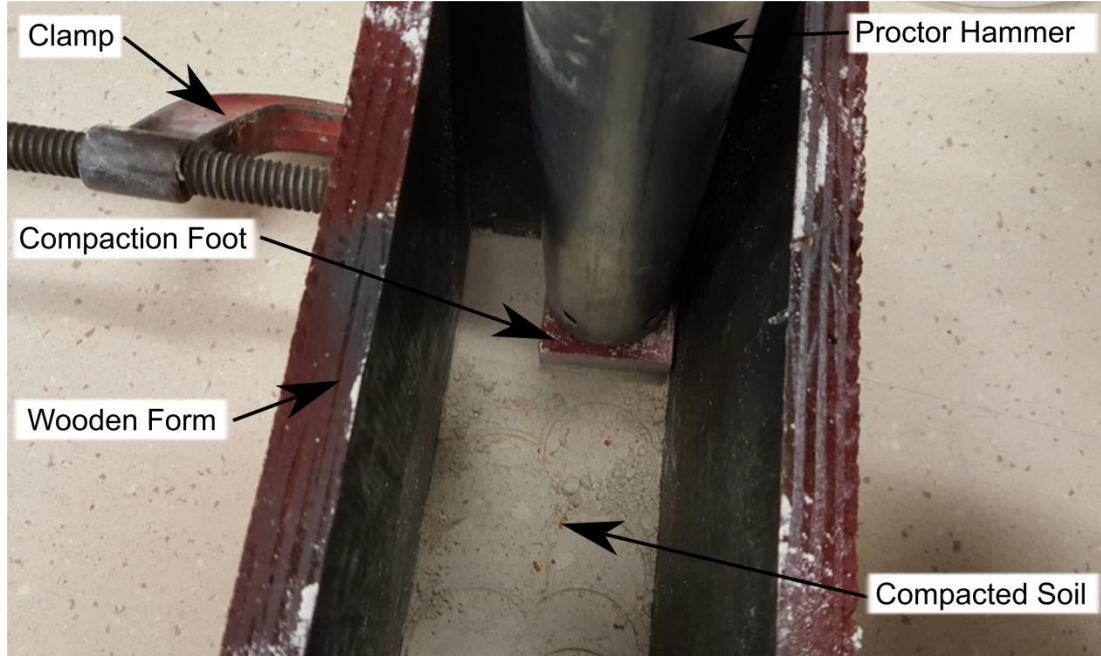


Figure 30 Model Preparation

For data acquisition, a textured surface is required on face of the model visible through the centrifuge cradle's window. This allows the analysis software to differentiate between portions of the model (Stanier et al., 2005). Once the soil has been compacted, one side of the form is removed and coloured sand is sprinkled, and then pressed, into the soil, ensuring that the face of the soil remains uniform (Figure 31). Care must be taken to tailor the degree and complexity of the texture to the type of analysis that will be conducted (Appendix C).

Once the texture has been applied the other sides of the form is removed and, using a sharp knife, the desired model geometry is cut into each face of the model (Figure 31). The extra soil above the profile is carefully removed using a wire saw and sharp knife, ensuring that the profile is uniform across the depth of the model to produce uniform behaviour parallel to the centreline of the road as well as along the width of the far field of the soil from the ditch to the cradle boundary.

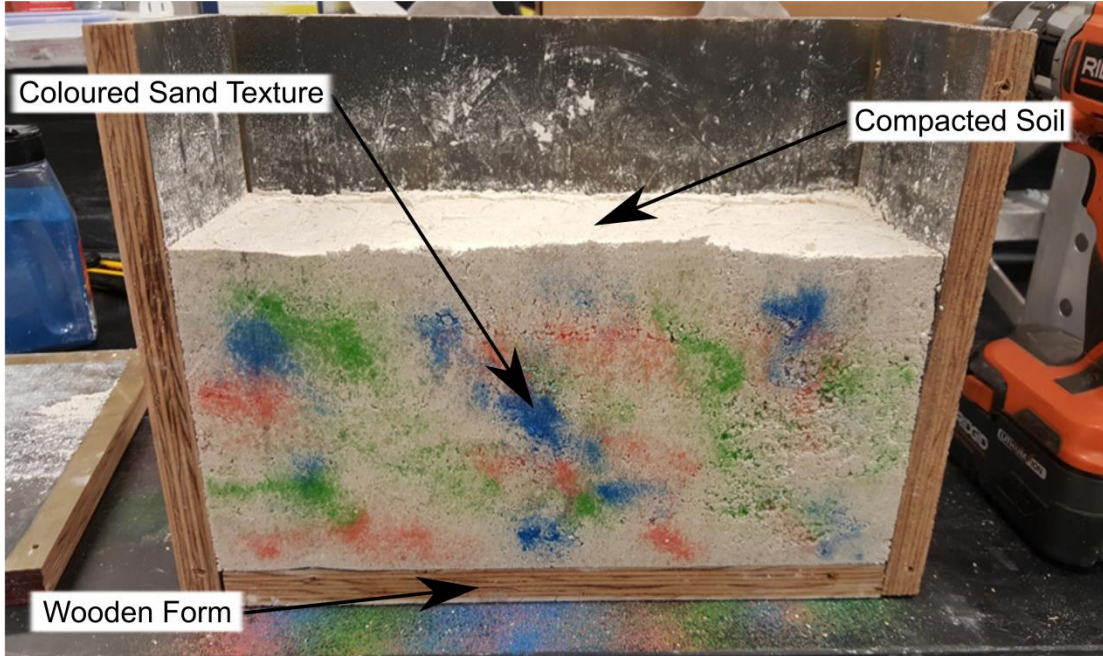


Figure 31 Typical Texture for Image Analysis

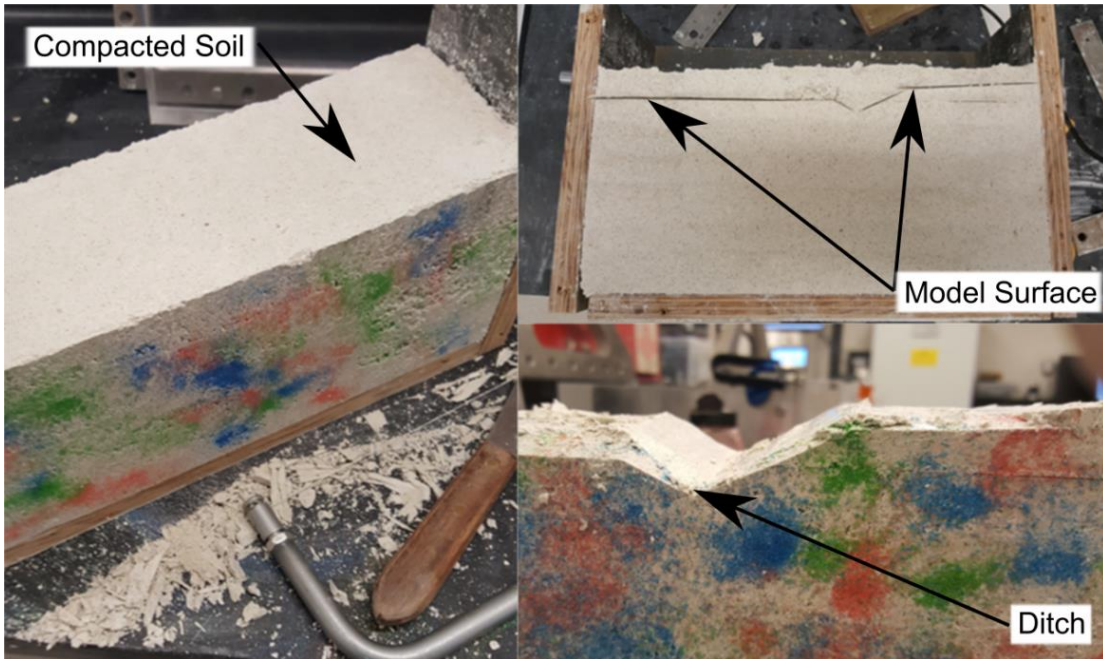


Figure 32 Model Construction

The impermeable road surface is achieved by applying a maximum thickness of 2mm of paraffin wax to the desired portion of the road surface (Figure 33). Melted wax is applied to the surface of the clay with a paint brush, using a paper template along the edge of the model road surface at the shoulder to prevent the running wax from affecting the permeability of the remainder of the model surface. This is done once the model had been placed inside the cradle to ensure a good seal between the surface and the cradle walls which ensures that infiltration does not occur through the road surface.



Figure 33 Impervious Road Surfacing with Paraffin Wax

3.3.5 Centrifuge Cradle Setup

The soil model is installed in the cradle centrifuge by placing the model on top of three 100mm square, 6.5mm thick filter stones with filter paper between the soil and the filter stones (Figure 34). The filter stones and lower drainage serve two purposes for these experiments. The first purpose is to prevent the dry air in the centrifuge drum from entering through the base of the model from. The second purpose is to allow for air to flow out of the soil ahead of the wetting front during infiltration. If air is not allowed to escape, the wetting front slows down and the degree of saturation in the wetted zone is less (Siemens et al., 2015), which is not representative of the prototype. The filter stones are hydraulically connected to an outlet through the side of the cradle, accessing a device allows bleeding of the air pressure. The device consists of a ¼” steel pipe connected to a flexible container (balloon) which can expand and release excess air without increasing air pressure (Figure 35). The balloon is located above the surface of the model, held within a rigid 3D printed PLA mount. This device allows air pressure to remain constant at the base of the model as well as to seal off the lower boundary from the dry air in the centrifuge drum.

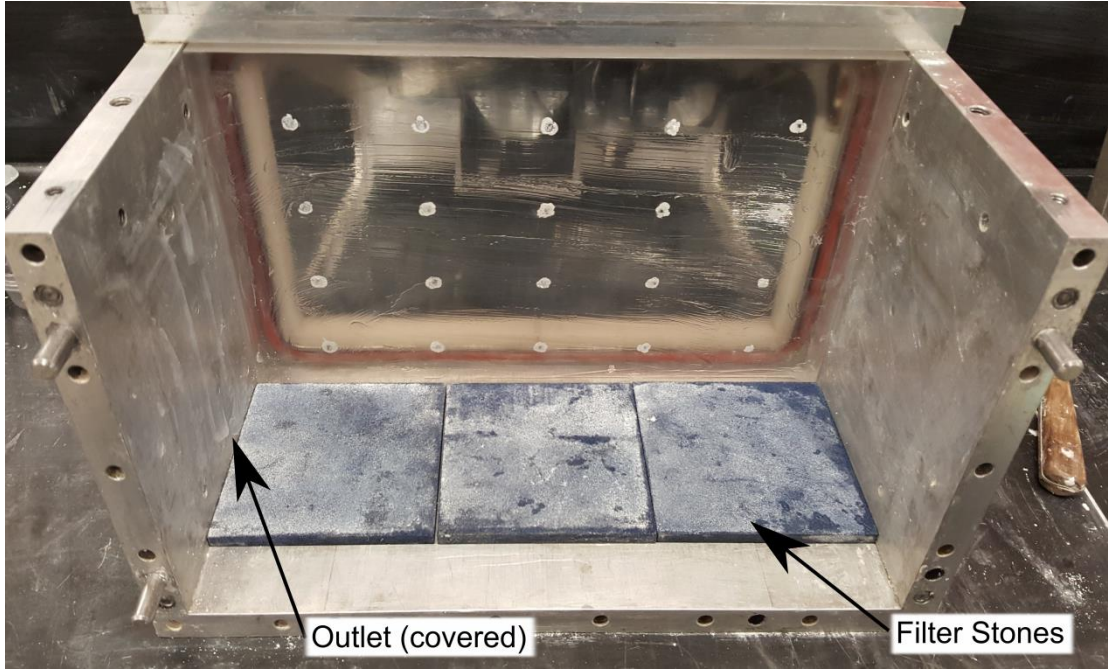


Figure 34 Filter Stone Base

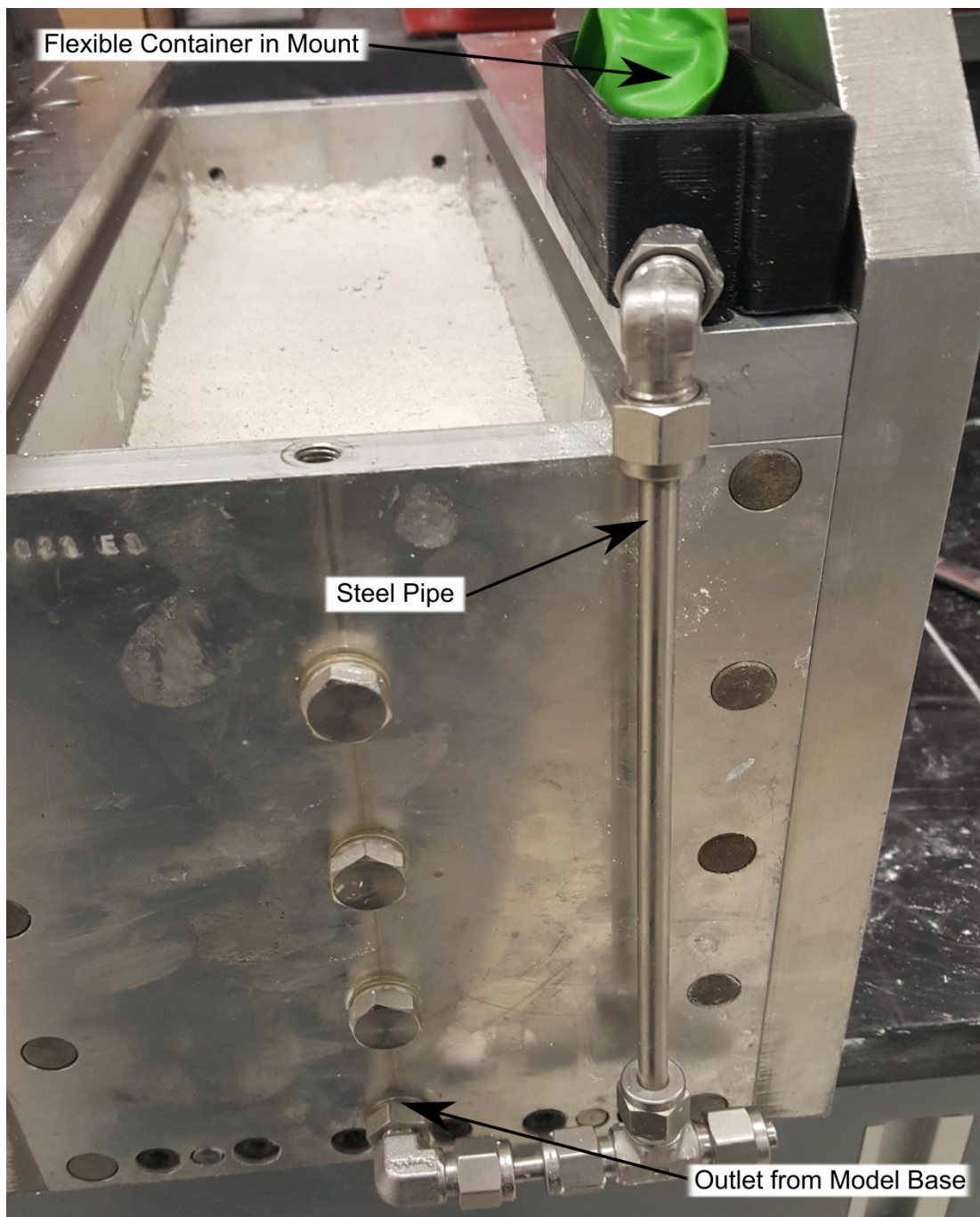


Figure 35 Air Control Apparatus on Centrifuge Cradle

After placing the model on the filter stones the model and filter stones are slid horizontally from the open side of the cradle into the cradle and against the cradle window. In order to minimize friction between the model and the glass and cradle walls as well as to ensure good contact for PIV, and that no leakage occurs around the sides of the model during

wetting cycles, liberal amounts of Dow Corning high vacuum grease are applied to all boundaries. This lubricant was chosen because it is resistant to water and highly viscous which helps to reduce the risk of flow around the sides of the model at its interface with the walls of the cradle and the Perspex windows. Once the model is in place, the side of the cradle is replaced and the screws tightened evenly to ensure a tight seal all around the model. Any voids that are visible along the interface between the model and the cradle are sealed with vacuum grease. The cross section installed within the cradle can be seen in Figure 36.

Once the sample is installed in the cradle the atmospheric control table, housing the rainfall apparatus as well as a relative humidity (RH) and temperature (T) sensor (Appendix B), are attached (Figure 38). The cradle, with all apparatuses that are required for the test, is weighed and a centrifuge balance calculation is done to determine the required counterweight. The cradle is then lowered into the centrifuge and attached at the pivot points along with the rainfall, power for lighting and cameras, and RH/T sensor (Figure 36).

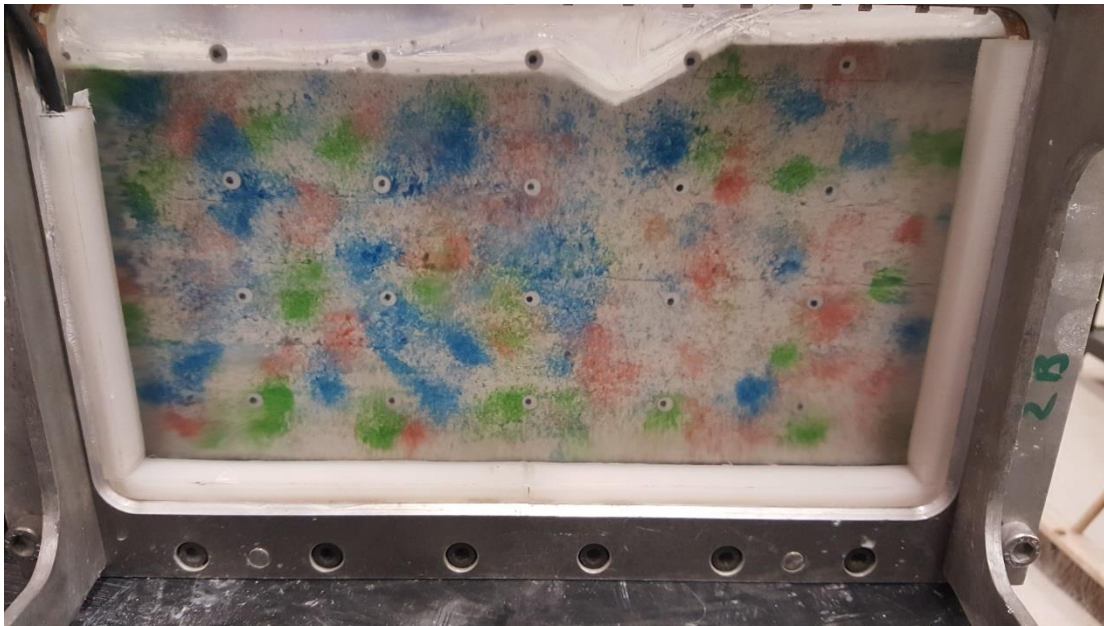


Figure 36 Constructed Road Model in Centrifuge Cradle

Two cameras (shown in Figure 37) monitor the models in flight. An ELP HD Webcam provides a live video feed of model in flight and a GoPro Hero4 captures images for analysis. The GoPro takes photos once per minute to capture the behaviour throughout the testing cycles. The ELP camera is used to monitor the rainfall and ensure that the test cycles are being applied correctly. A strip of LED lights contained in a 3D printed light diffusing cover provides lighting for the cameras while minimizing glare and reflections on the Perspex window. Control points on the window allow for correction of camera movement during flight, lens distortion, and calibration of the data to model units (Figure 36).

A Vaisala HMP 110T RH/T sensor is also mounted on top of the atmospheric control table (Figure 37). This measures relative humidity and temperature in the air space above the model which is used to estimate suction during drying cycles. The atmospheric control table also holds three Continental PCMK-25 misting nozzles (Figure 38). The three nozzles are set

approximately 100mm above the model surface which gives each nozzle a coverage area of 100x100mm (or 1/3rd) portion of the 300x100mm sample surface. The three misting nozzles provide an even distribution of water across the surface of a model within the cradle while minimizing the size of the droplets to accommodate the scaling of the drops and minimize their impact effects on the surface of the model. The water is supplied through the centrifuge stack from a pressure vessel set to 70kPa, the minimum operating pressure for the nozzles. This produces a cumulative flow through the nozzles of 60ml/minute when the valve at the top of the stack is opened, providing an even distribution of infiltration during the test.

Atmospheric conditions within the centrifuge are monitored throughout the experiment using the on-board computer. Both the RH/T sensor and the ELP camera are connected to the onboard computer. The onboard computer includes an Aclipse Data Acquisition System (DAS) which allows for data acquisition and real-time data plotting during flight and can be accessed remotely via a fiber optic cable.

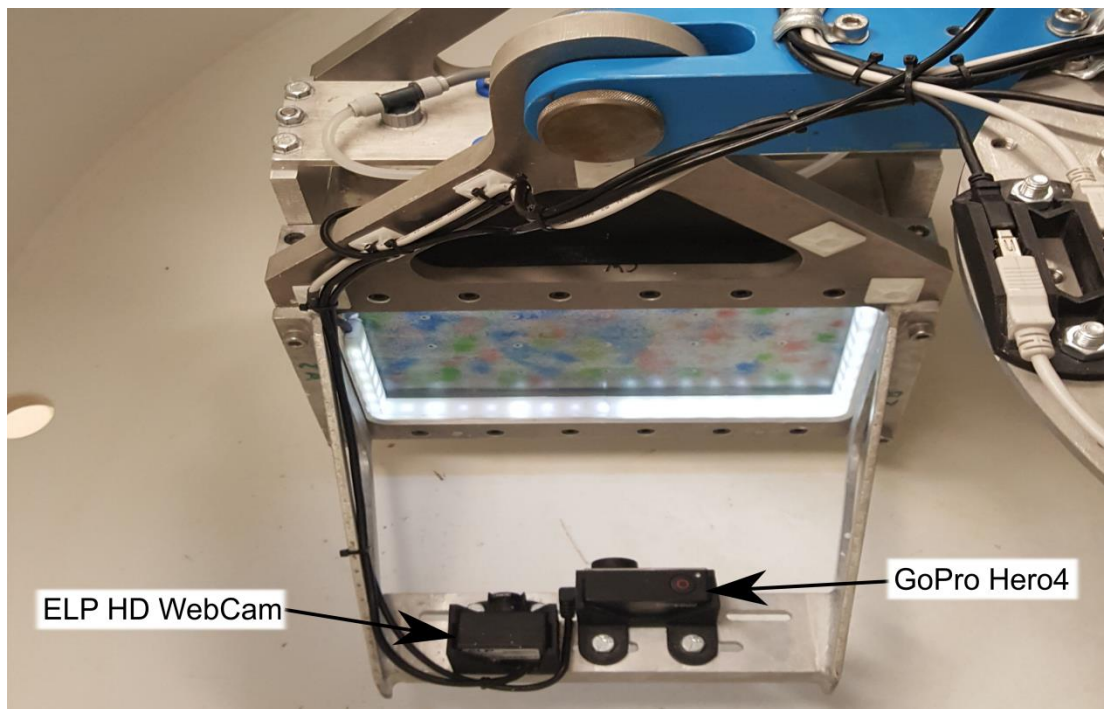


Figure 37 Camera Layout

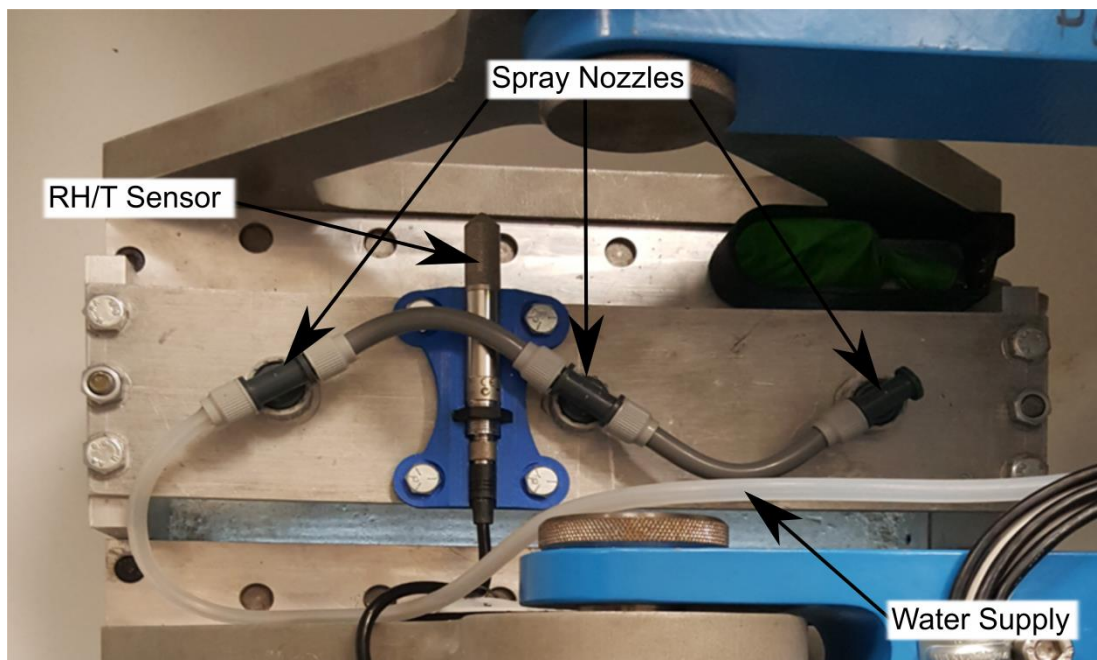


Figure 38 Atmospheric Control Apparatus

3.3.6 Testing Cycle

With the model and cradle installed in the centrifuge, the cameras, RH/ T sensor, and data acquisition are started. Once these are confirmed the centrifuge is started and accelerated at three RPM/sec to the target N_g . For all tests conducted in this chapter the target N_g is 40g (233RPM). After the target RPM is reached the sample is allowed to settle for 15-30 minutes in order for any movements from the increased acceleration on the model to occur. At this point the model is ready to undergo the seasonal wetting and drying cycles that will produce any volume change in the soil.

A testing cycle that gives representative atmospheric conditions, infiltration from rainfall and evaporation from ambient RH and T conditions was chosen to permit volume changes to occur. Three cycle wetting-drying periods were applied to the model over a total test length of 36 hours. Preliminary tests investigated the effect of an extended drying time (up to 24 hour cycles), however this produced excessive drying which can cause extreme model degradation. Using a 12 hour cycle helped reduce the degradation of the model, particularly with respect to its boundaries with the cradle walls which would fail to remain sealed if too much shrinking occurred.

Figure 39 shows a typical test of three wetting/drying cycles with 200ml rainfall events. Initial tests were subjected to 100ml-300ml rainfall events to gauge the effect of these volumes. After observing the initial tests, a 200ml rainfall was chosen for the remaining tests because it allowed for a sufficient depth of infiltration through the zone of interest but would not interfere with the bottom boundary condition. The scaled depth of the 200ml rainfall over the 300cm³ surface area of the model is 267mm of rainfall. This can be compared to an average annual precipitation of 390mm in Regina, Saskatchewan (Gov. of Canada, 2010),

926mm in Oklahoma City, Oklahoma, or 870mm in Austin, Texas (US Climate Data, 2017); all regions which experience problems with expansive soils. Because of the rate of precipitation produced by the rainfall apparatus is greater than the maximum infiltration rate of the soil, the infiltration cycle is achieved by a rapid ponding of water which is then permitted to infiltrate until the surface is dry.

The drying cycle begins as soon as the surface is dry. In Figure 39 the RH observed during the test, on the vertical axis, is plotted over the cycles to indicate the degree of suction for the drying cycle. This suction is determined using the Kelvin equation (Equation 14, Fredlund et al., 2012). The spikes in RH readings at each ponding cycle are a result of the misting from the nozzles occurring in the vicinity of the sensor but due to the ponding the RH for the surface soil during the wetting cycles is assumed to be 100% as shown on the graph. The drying cycle is ended after 12 hours from the start of the last wetting cycle.

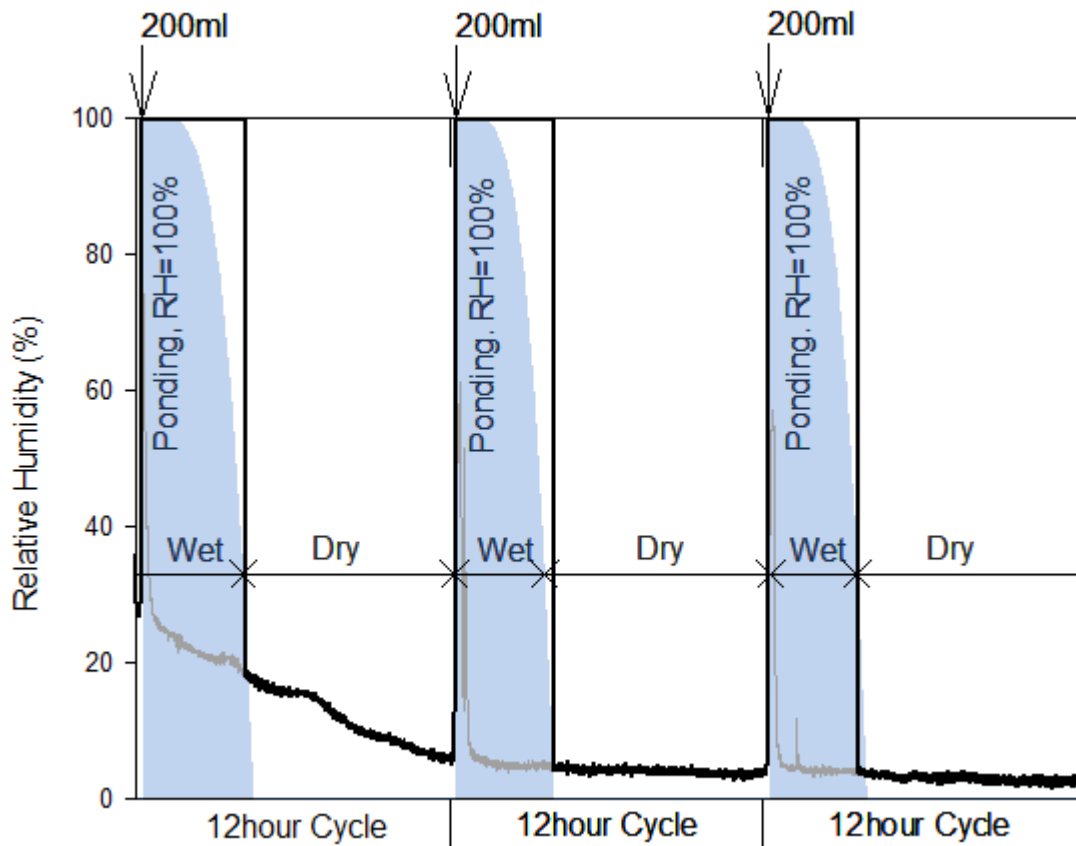


Figure 39 Typical RH for Wetting and Drying Cycles

$$(u_a - u_w) = -135,053 \ln(\text{RH}) \quad \text{[Equation 14]}$$

After a test was completed the model was removed at the end of the last drying cycle. Soil samples were taken at various locations representative of the portions of the model throughout its depth. These were weighed and oven dried for a minimum of 48hrs to determine the gravimetric water content and subsequently to provide further information for understanding the infiltration and evaporation effects on the model.

3.3.7 Particle Image Velocimetry Analysis

The two tests are analyzed using particle image velocimetry (PIV). The analysis provides displacement measurements across the entire soil profile for every image captured. An analysis is conducted for each of the wetting and drying cycles in each test. The two types of behaviour analysed are the vertical displacement and vertical strains throughout the model. These displacements and strains are compared with the predicted behaviour leading to the described (Zornberg et al., 2009) failure mechanism and with results observed in case studies (Roodi et al., 2016).

To maximize the benefit of full observation of the cross section for the duration of the testing of each model, particle image velocimetry (PIV) developed for geotechnical applications (White, et al., 2003, Stanier, et al., 2015) is used. This method allows for a robust analysis of the data gathered by the GoPro camera during testing including behaviour both at the surface and through the depth of the model profile. The analysis provides a full description of the behaviour of the model throughout the tests.

PIV analyzes a series of photos and identifies changes in the pixel values in the images. The PIV software defines a portion of a digital image as a set of patches (Figure 40). PIV identifies the new location of each of the patches for each subsequent photo step. The resultant output from the PIV gives displacement of each patch in digital pixels as changes in location from original u (horizontal) and v (vertical) pixel locations, producing a field of displacement vectors over the region of interest (RoI). The program also produces a correlation coefficient describing how close of the match for each patch is. PIV produces high resolution displacement data throughout the model profile. This data can be gathered quickly and easily by the cameras in the centrifuge and allows a comprehensive description of the behaviour during wetting-drying cycles.

A representative selection of the thousands of images taken during the test is chosen. This consists of selecting approximately 20 photos for each wetting and each drying cycle. The frequency of images used is chosen to match the changes in displacement rate for the faster displacement rates in wetting and the slower displacement rates in drying. This ensures that the range of displacements is being captured as well as improving the correlation between steps of the analysis.

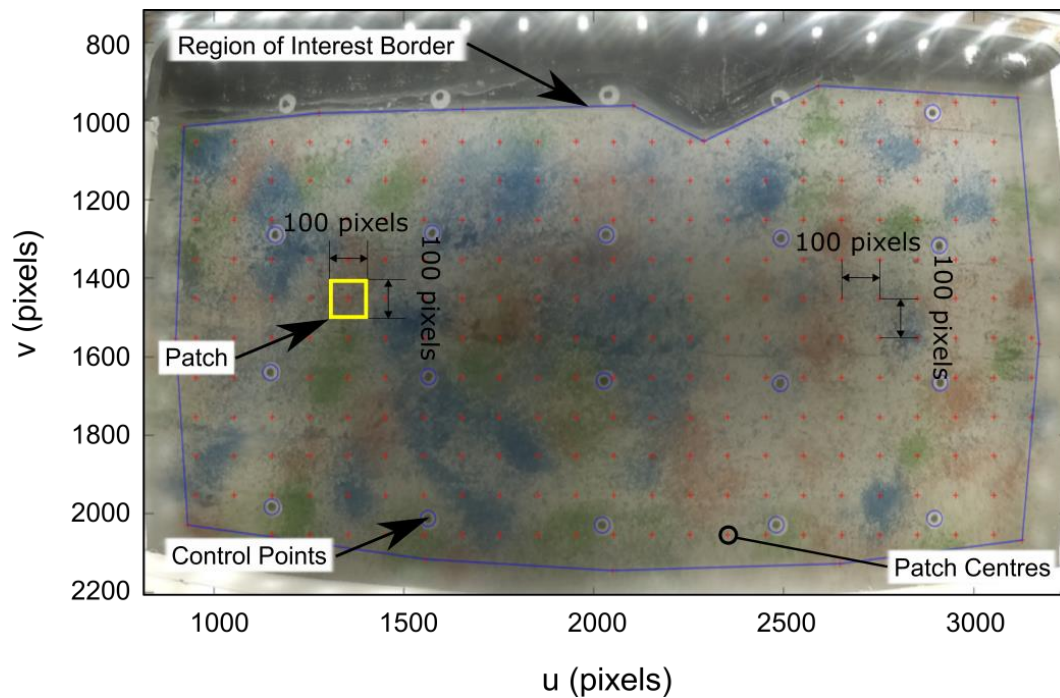


Figure 40 Typical PIV Analysis Mesh (Modified Road)

To translate pixels into real-world units, a control point analysis using a matrix of the known coordinates of the control points in millimeters is run for each test with the analysis images. This is conducted using the same selection of images from the test as would be used for the displacement analysis. The displacement analysis was then run on the images and the pixel displacement data. However, the error for the control point analysis was typically high and, when combined with the minor error in the uv (Table 8 and Figure 41) data produced in the displacement analysis, the calibrated data had too high a degree of error (achieved error of 10px compared to the suggested limit of 0.5px) to achieve the precision desired to describe the displacements in the models. As a result, the uv data was used for the analysis of the relative displacements and directly processed for the strain calculations to minimize error. The scale of these displacements can then be manually calibrated to compare with observed displacements in case studies. Table 9 shows the suggested starting values (Stanier et al., 2015) for the analysis parameters to achieve good displacement data. The values used for the tests, while slightly lower than those suggested by Stanier (et al., 2015) to accommodate changes in the images due to infiltration into the model and other incidental image effects, were still high enough to minimize “wild” vectors (Figure 41).

Figure 41 shows the vertical displacement values for patches nearest the surface of the soil, across the top of the model, for a typical analysis. The corresponding coefficients of correlation (CC_{field}) for each patch in the mesh and each step of the analysis are also plotted. The CC_{field} values are consistently high for the analysis with minor variations. Note at analysis step 85 that the CC_{field} for several patches dips below the $CC_{\text{field tolerance}}$ value; this is a permissive function of the program which, if required, will relax tolerances by 10% in order to successfully calculate an analysis step without causing the analysis to fail. The consistently

high coefficients of correlation for each individual patch provides confidence in accuracy and precision for the uv data's description of small movements in the soil.

Table 8 PIV Displacement Analysis (Leapfrog Analysis with 50 Iterations¹)

| Model Type | Number of Images | CC _{seed tolerance} | CC _{field tolerance} | $ \Delta p _{\max}$ |
|--|------------------|------------------------------|-------------------------------|---------------------|
| Suggested Starting Values ¹ | NA | 0.95 | 0.75 | 1e-05 |
| Test 1 | 116 | 0.80 | 0.50 | 1e-05 |
| Test 2 | 124 | 0.90 | 0.75 | 1e-05 |

¹Values suggested as first attempt values for analysis by Stanier et al., 2015

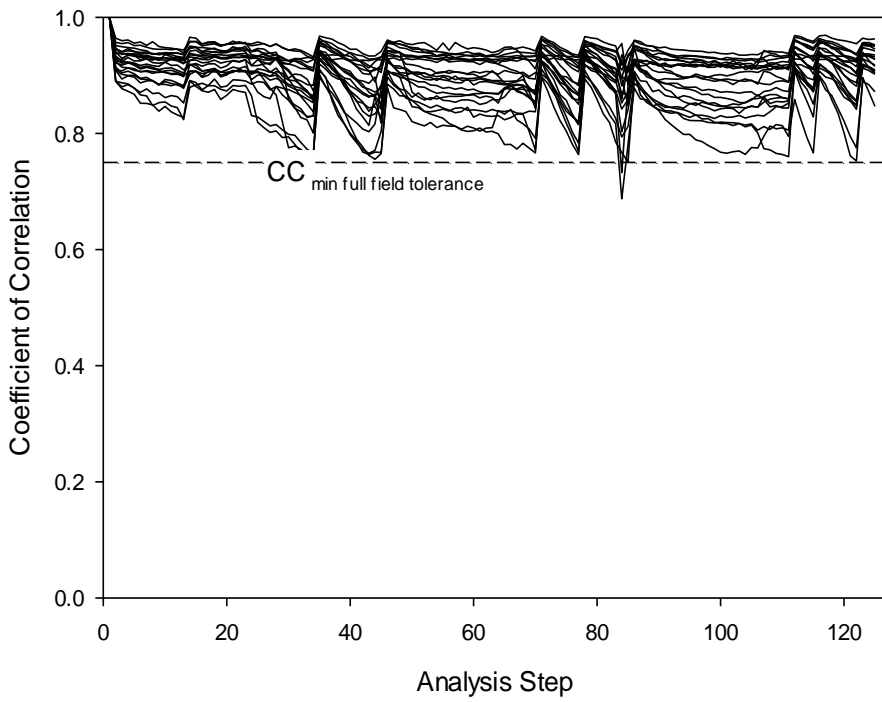
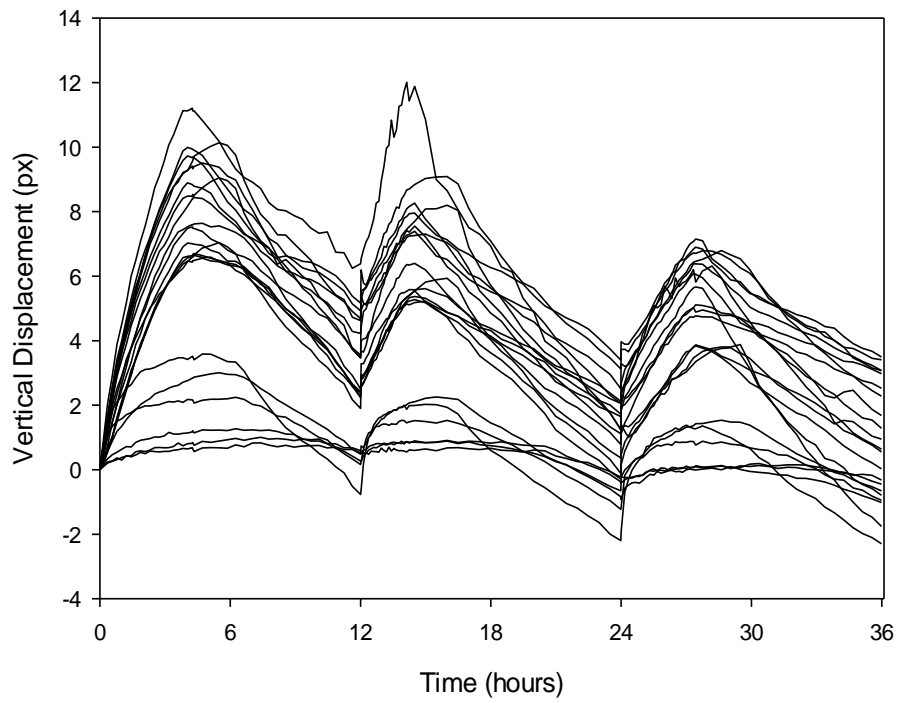


Figure 41 Typical Correlation Coefficients Values with Patch Displacement Data

3.4 Results

Two idealized road model test results are presented in this chapter: an idealized road with a fully surfaced upper portion and flat lower portion (Test 1) and a modified road model with an exposed shoulder and a ditch at the base of the slope (Test 2). Details of the cross-sections are given in **Figure 25** and more details are listed in Table 9. Each test consisted of three 12 hour wetting and drying cycles for a total duration of approximately 36 hours. The wetting cycles consisted of a rainfall event totalling 200ml precipitation resulting in ponding on the model surface. The impact of the wetting cycles is controlled by the soil's void ratio (e) and degree of saturation (S) of the soil. The depth at which saturation occurs corresponds to the depth of wetting front. The initial void ratio of the soil (at 1.34g/cm³ dry density) was calculated to be 0.95. With 28% water content and 77% saturation of the available volume of voids, a volume of air of 34cm³ exists per cm depth of soil. As a result, the 200ml rainfall was predicted to saturate the soil and produce expansive behaviour to a depth of nearly 60mm, or, at prototype scale, 2.4meters.

Drying cycles began when the surface dried and continued until the next 12 hour cycle began. The wetting cycles are followed by a period of applied suction, or drying. For the drying cycles the RH and T are driven by the ambient air conditions within the centrifuge. The suctions applied during the drying cycle reverse the swelling volume change that occurs in the wetting cycle back to approximately the same or less than the start state, providing a significant range of displacements to be observed. These ranges of swelling as a result of wetting and shrinking as a result of drying were analysed.

The analysis of the data produces the displacement and strains in the three portions of the model. The Test 1 Road Model is presented first and the Test 2 Road Model second. Plots of the displacements at the surface are presented as well as the behaviour of the model below the surface which is described with the strain of the soil throughout its depth. The displacements and strains are described with the zones that have been previously discussed; below the far field, below the transition zone (slope and ditch), and below the paved road.

Table 9 Testing Cycles for Test Serials

| Test Serial | Road Width | Pavement Width | Ditch | Number of Cycles | Cycle Length | Rainfall Volume ¹ |
|-------------|------------|----------------|-------|------------------|--------------|------------------------------|
| Test 1 | 92.5mm | 92.5mm | No | 3 | 12 hours | 200ml |
| Test 2 | 92.5mm | 82.5mm | Yes | 3 | 12 hours | 200ml |

¹ for each of the three wetting cycles.

3.4.1 Test 1 Road Model Results

In order to analyse the expansive behaviour of the model, the beginning and end of the wetting and drying cycles need to be determined. The start of the wetting cycles is controlled by turning on of the rainfall apparatus but the determination of the end of the wetting cycle is less clearly defined during testing. Figure 42 shows the applied wetting and drying cycles as ponding and suction (calculated using Equation 14).

During ponding the suction is assumed to be 0kPa at the surface. The end of the ponding indicates the end of the wetting cycle and the beginning of the drying cycle when suction is applied to the surface of the model. This corresponds to an end of swelling and the beginning of the shrinking cycle. A selection of the uv displacement data is used to determine the beginning and end of the swelling period. An average displacement value of ten patches near the surface (at a depth of approximately 10mm) and across the far field zone of the model is used to give a representative baseline of the expansive soil's behaviour. The peak displacement of this portion of the model is taken to indicate the time when water is no longer ponded at the surface. The local maximum and minimum values for each cycle of the test are identified from Figure 43 and indicate the end and beginning of each wetting cycle. The corresponding times and image steps are used for further analysis of each of the three wetting and drying cycles.

The variation in duration of ponding seen in the wetting and drying cycles is produced by the rate of infiltration changing as soil structure changes and the amount of water that evaporates during ponding.

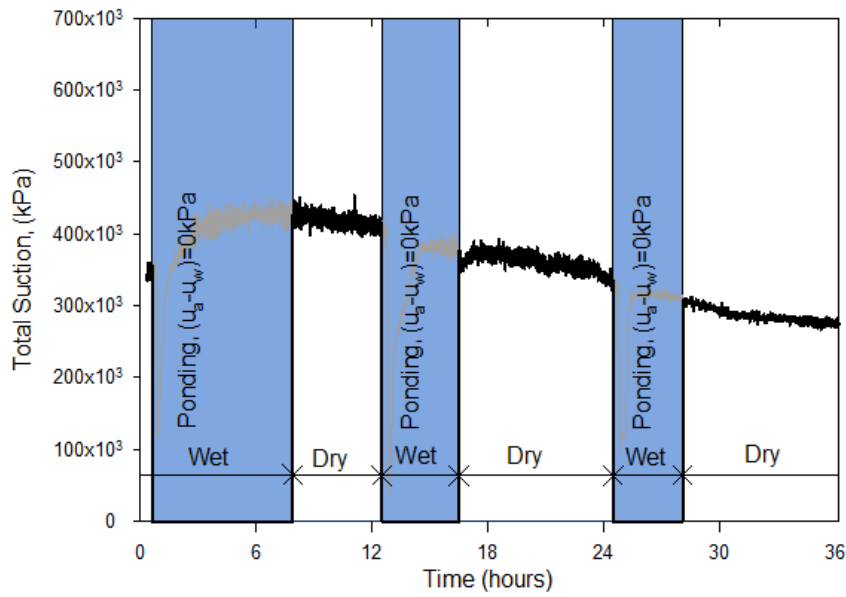


Figure 42 Test 1 Road – Total Suction Applied to Surface

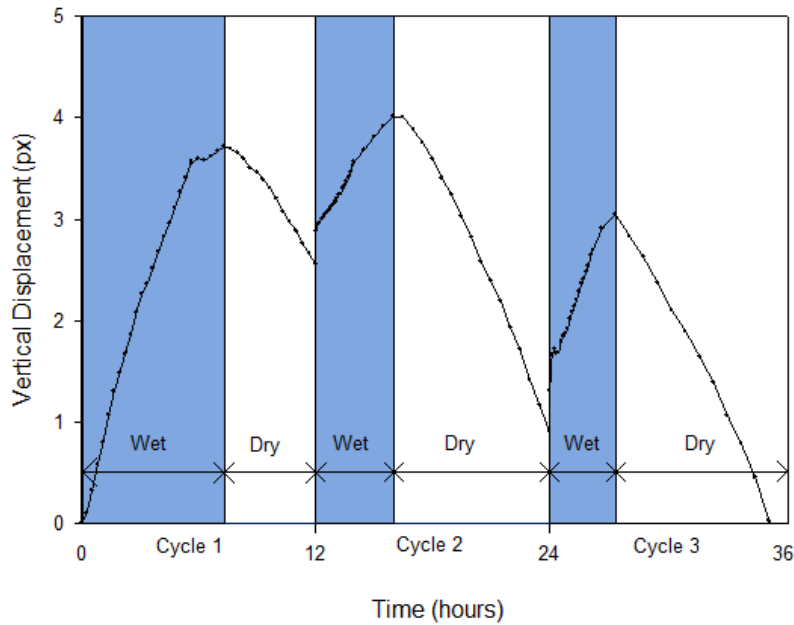


Figure 43 Test 1 Road – Average Displacement for Top Patches Below the Far Field

Figure 44 show the surface of the Test 1 Road Model which is analysed for vertical displacement. The three zones, far field, transition, and paved road, are indicated as well as the scale. These can be seen in relation to typical images from of the model. Note the distortion from the lens implies curvature of the far field and road surface when the actual far field is flat and the road camber increases in elevation towards the centreline (**Figure 25**). The far field is descriptive of the normal displacement behaviour of expansive soil while the transition and paved road show the displacements of the structure. The location of the roads is also shown for reference. This appears in the subsequent strain plots.

The vertical displacements across the model surface for the three zones are plotted in relation to the image (Figure 44). Generally, the far field experiences significant displacement while the transition zone has reduced displacements and the road shows almost no displacement, approaching zero towards the centerline. The maximum (swelling) and minimum (shrinking) displacements for each cycle are plotted with the original, normalized elevation (0) indicated. Note the distortion from the lens implies curvature of the far field when the actual model is flat. The far field is indicative of unimpacted behaviour of expansive soil while the transition and paved road zones show the impacts of the soil-structure interaction. A localized vertisol effect caused by the formation of a large vertisol is seen in the middle of the far field. A vertisol is a vertical crack in a soil mass formed as a result of horizontal strain (shrinking). While the effects of this vertisol do not extend to the transition or road, localised impacts are visible in some of the strain plots.

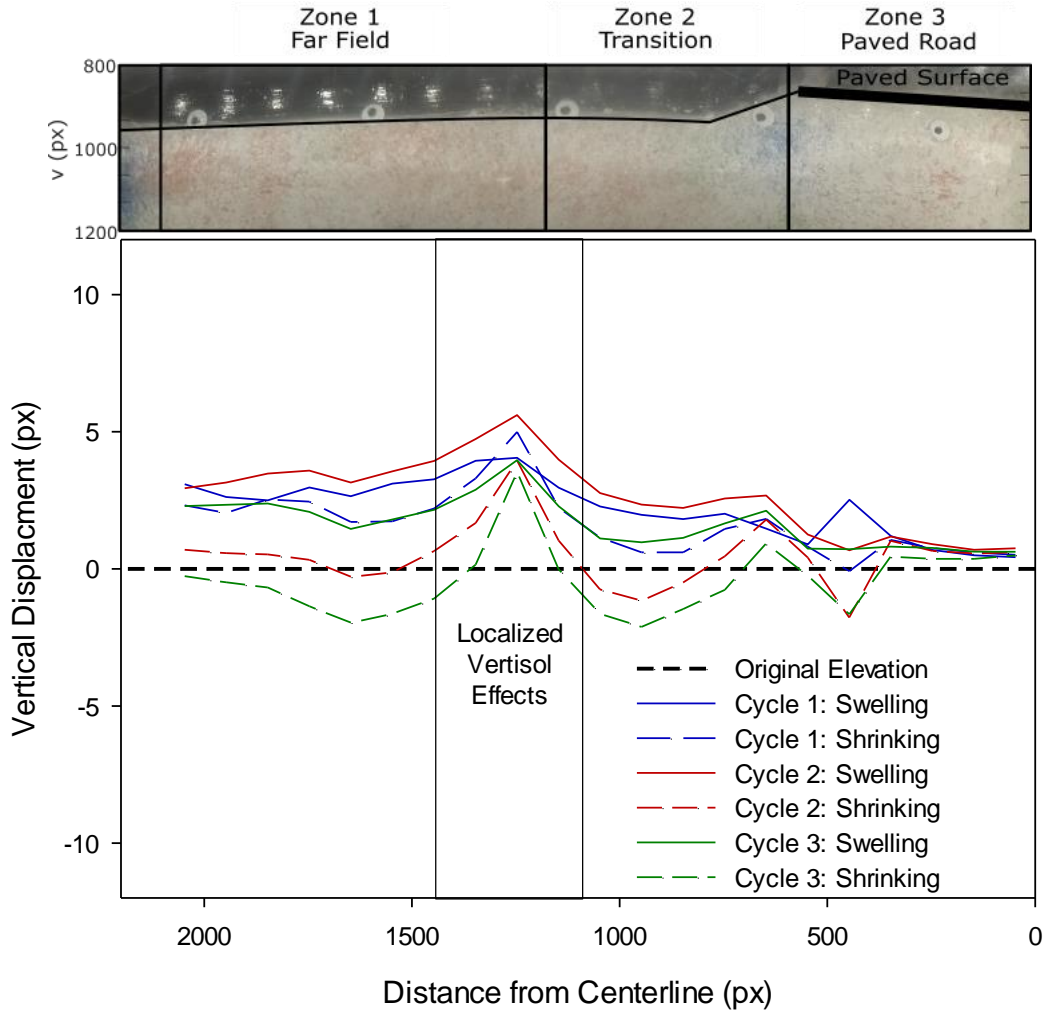


Figure 44 Test 1 Road - Vertical Displacement of Model Surface at the End of Each Cycle (Swelling/Shrinking)

The subsurface strains show the underlying mechanism for the surficial displacements. Figure 45 is a typical image from Test 1 and also indicates the location of the analysis zones as well as the initial surface. The strains below the surface do not meet the surface due to the location of the patches chosen. Figure 46 and Figure 47 show contour plots of subsurface strains throughout the Test 1 Road Model. Each cycle is shown for both swelling (Figure 46) and shrinking (Figure 47). Contours are plotted on 0.25% intervals. The extent of the wetting front is indicated by the 0.25% contour, the smallest contour where strain is observed. In the far field the wetting swelling occurs in the upper 250 pixels below the surface. Maximum swelling occurs at the surface and decreases with depth. The impact of the vertisol in the middle of the far field zone can be seen. However, the contours demonstrate its localized impact. Throughout the three wetting cycles the depth of infiltration of the 200ml infiltration events produces vertical strains down to the same depth. The one variation from this is a

slight reduction in Cycle 2 (Figure 46B); coupled with this reduction some strain is observed at lower boundary of the model for Cycle 2. This is likely caused by minor leaking around the boundaries of the model. The lost water reduces the depth of the wetting front slightly. Because the stress at the base of the model is relatively greater, little strain is produced by this change in suction at the base of the model (**Figure 20**) and it has minor impacts on the global behaviour.

Typical vertical strain profiles, plotted in Figure 48, display the cyclic strain profile through the expansive zone. For all three columns, far field, transition, and paved road all reduce to zero strain at the bottom of the zone of interest, confirming that the expansive zone is limited to this zone of interest. Comparing the three zones shows that greatest strains occur in the far field, lesser strains in the transition, and approaching zero strains below the paved road.

The gravimetric water contents taken at the end of drying Cycle 3 (Figure 47C) of Test 1 are plotted in Figure 49 for both below the far field and below the paved road. The gravimetric water contents profiles are consistent with the image analysis. Gravimetric water content reduction in the unpaved region (far field) of the model is notably larger than the reduction under the paved road, consistent with the applied suctions at these two points.

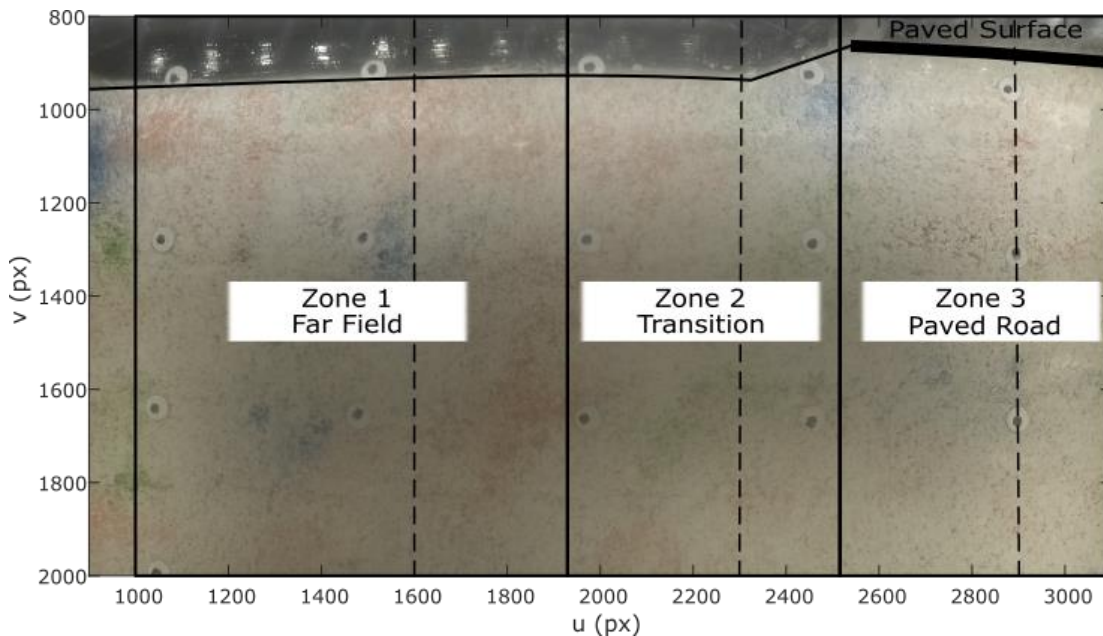


Figure 45 Test 1 Road – Surface and Zones with Image Dimensions

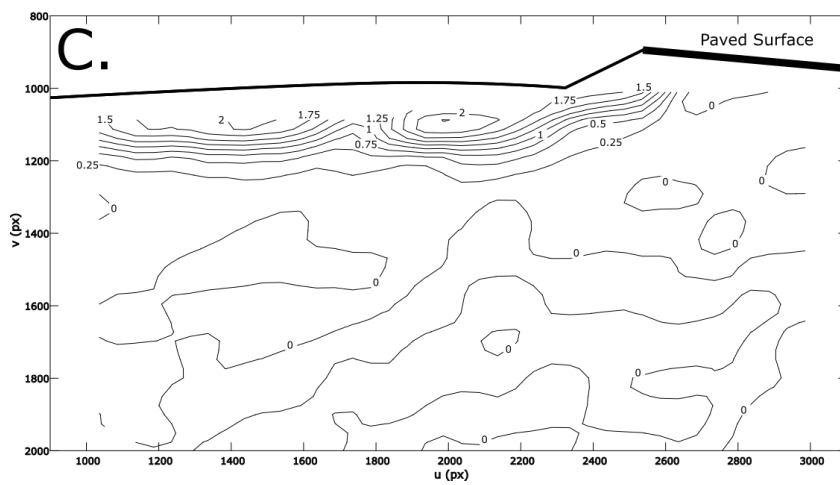
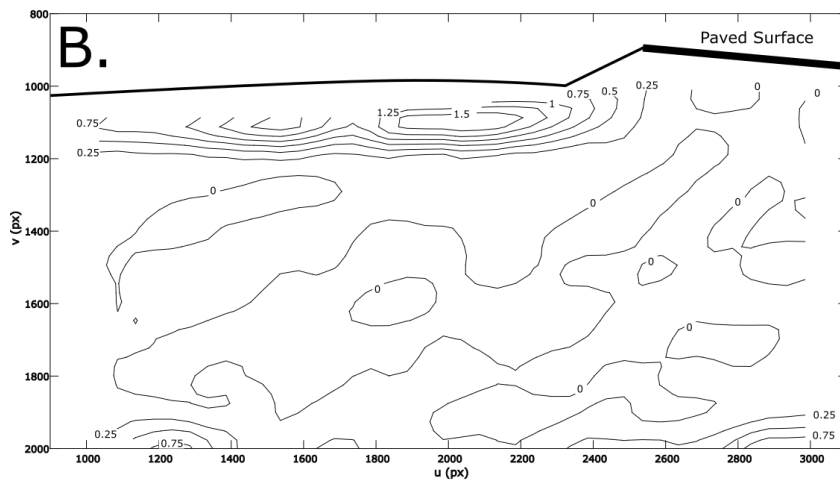
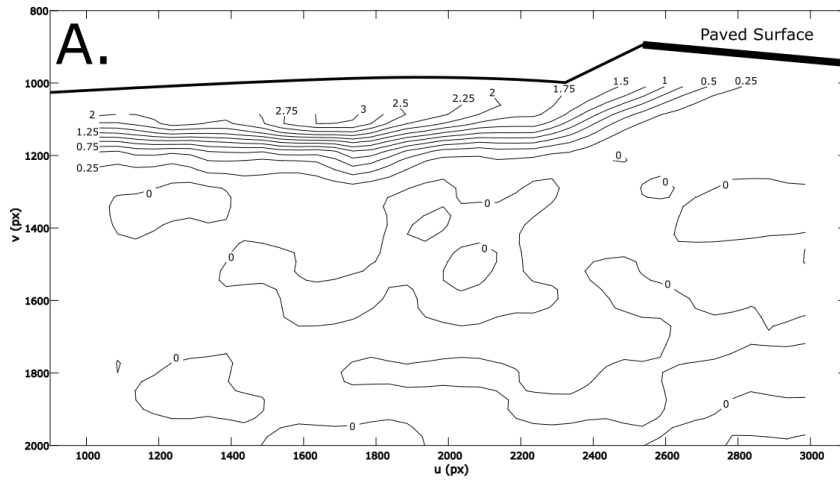


Figure 46 Test 1 Road – Swelling Strains for Cycles 1 (A), 2(B), and 3(C)

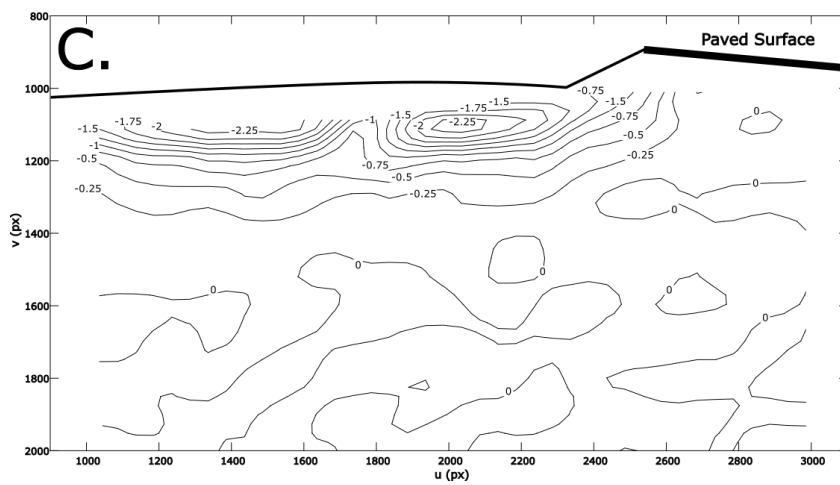
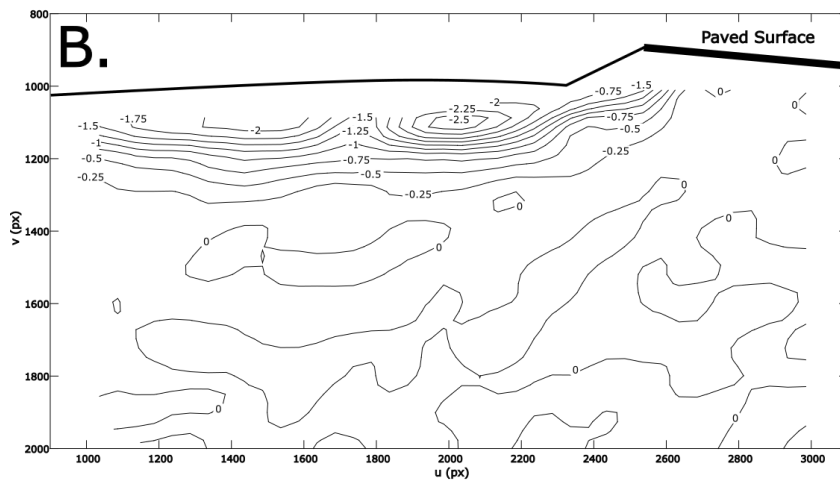
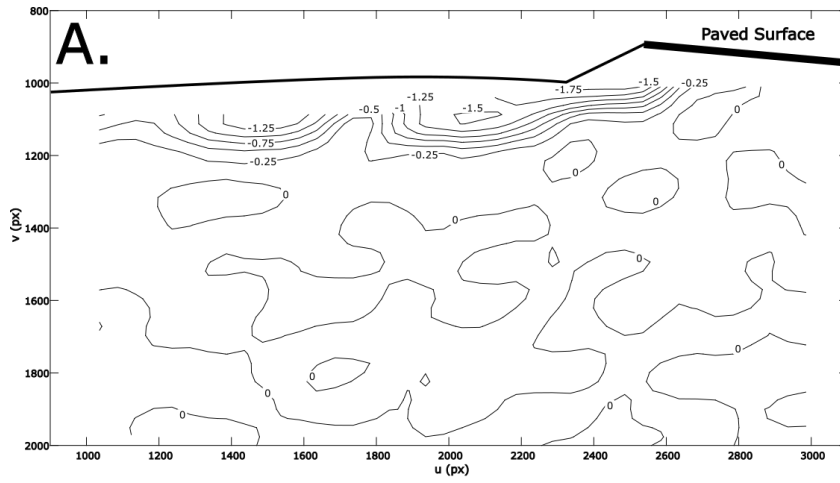


Figure 47 Test 1 Road – Shrinking Strains for Cycles 1 (A), 2(B), and 3(C)

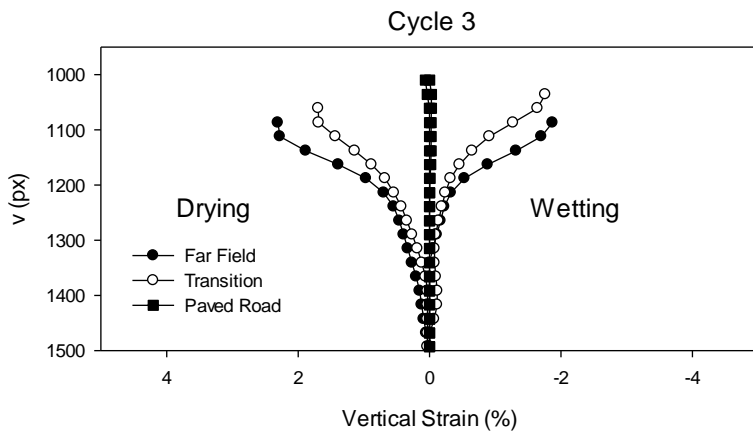
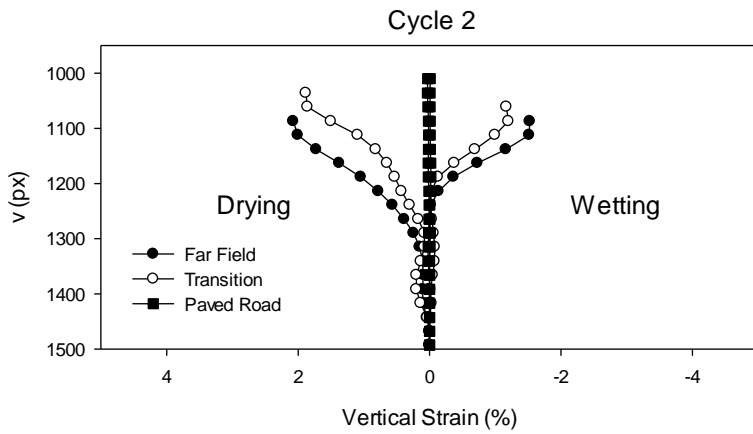
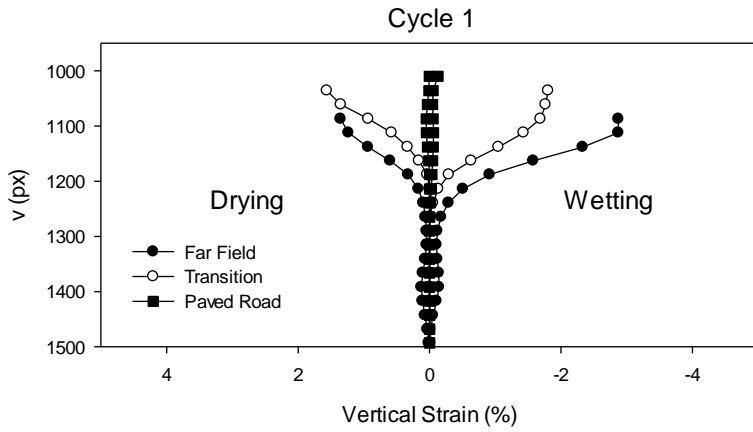


Figure 48 Test 1 Road – Vertical Strains through Expansive Zone for Representative Profile

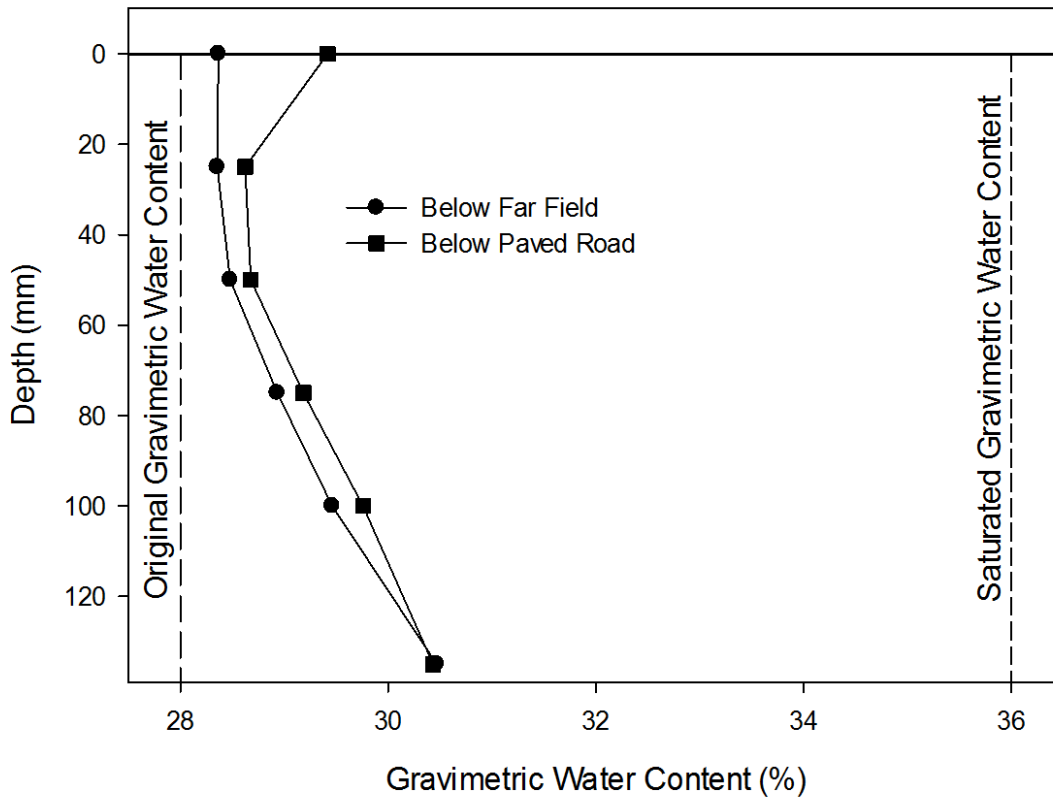


Figure 49 Test 1 Road – Water Contents with Depth at End of Drying Cycle 3

3.4.2 Test 2 Road Model Results

The beginning and end of the wetting and drying cycles in Test 2 were determined using the same method as Test 1. Figure 42 shows the applied wetting and drying cycles as ponding and suction. A selection of the uv displacement from across the far field zone of the model is plotted to give a representative baseline of the expansive soil’s behaviour. The peak displacement of this portion of the model is taken to indicate the end and beginning of each wetting cycle. The corresponding times and image steps are used for further analysis of each of the three wetting and drying cycles.

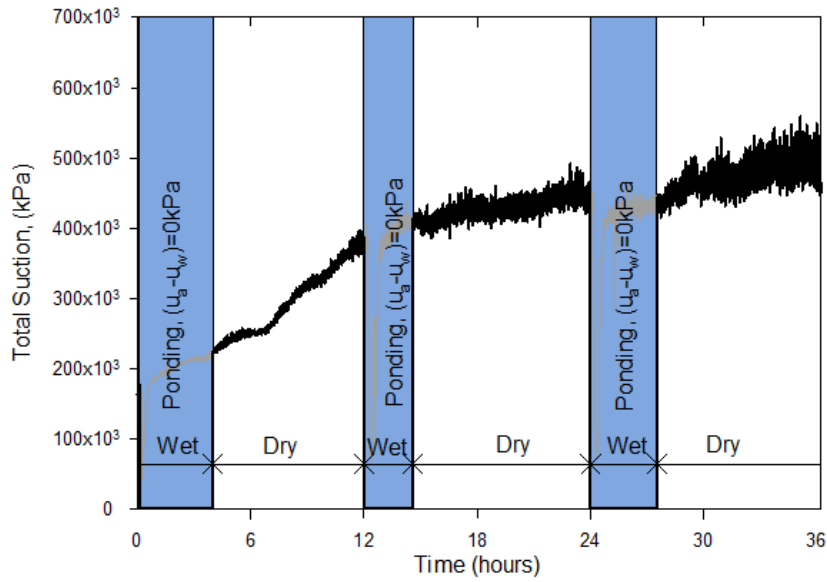


Figure 50 Test 2 Road – Total Suction Applied to Surface

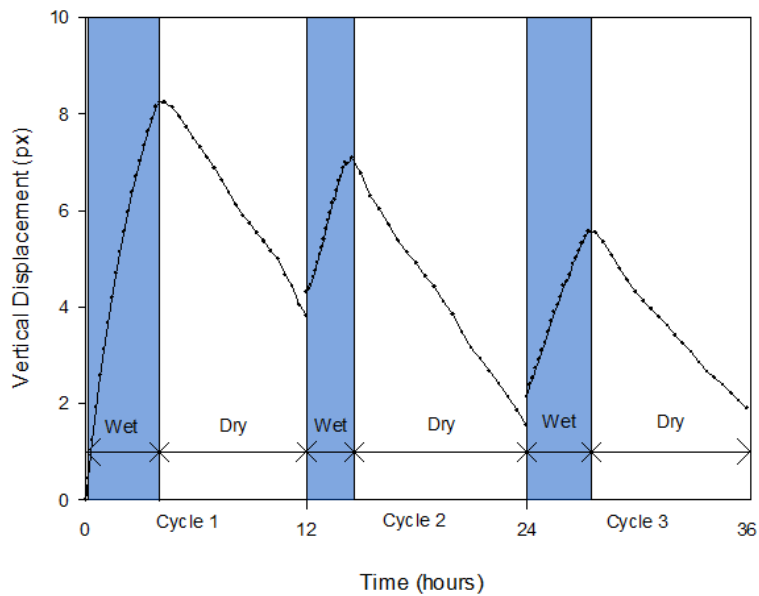


Figure 51 Test 2 Road – Average Displacement of Top Patches Below the Far Field

Figure 52 shows the surface of the Test 2 Road which is analysed for vertical displacement. Again, three zones, far field, transition, and paved road, are indicated as well as the scale. These are seen in relation to a typical image from of the model the addition of the ditch and the reduced paved surface compared with the Test 1 Road (Figure 44). The location of the roads is also shown for reference. This appears in the subsequent strain plots. Also plotted are the vertical displacements across the model, including all three zones. As with Test 1, the maximum (swelling) and minimum (shrinking) displacements for each cycle are plotted with the original, normalized elevation (0) indicated. The far field experiences significant displacement which increased towards the transition zone which shows large displacements, reducing at the slope of the road. Comparatively, the road shows almost no displacement, again, approaching zero towards the centerline.

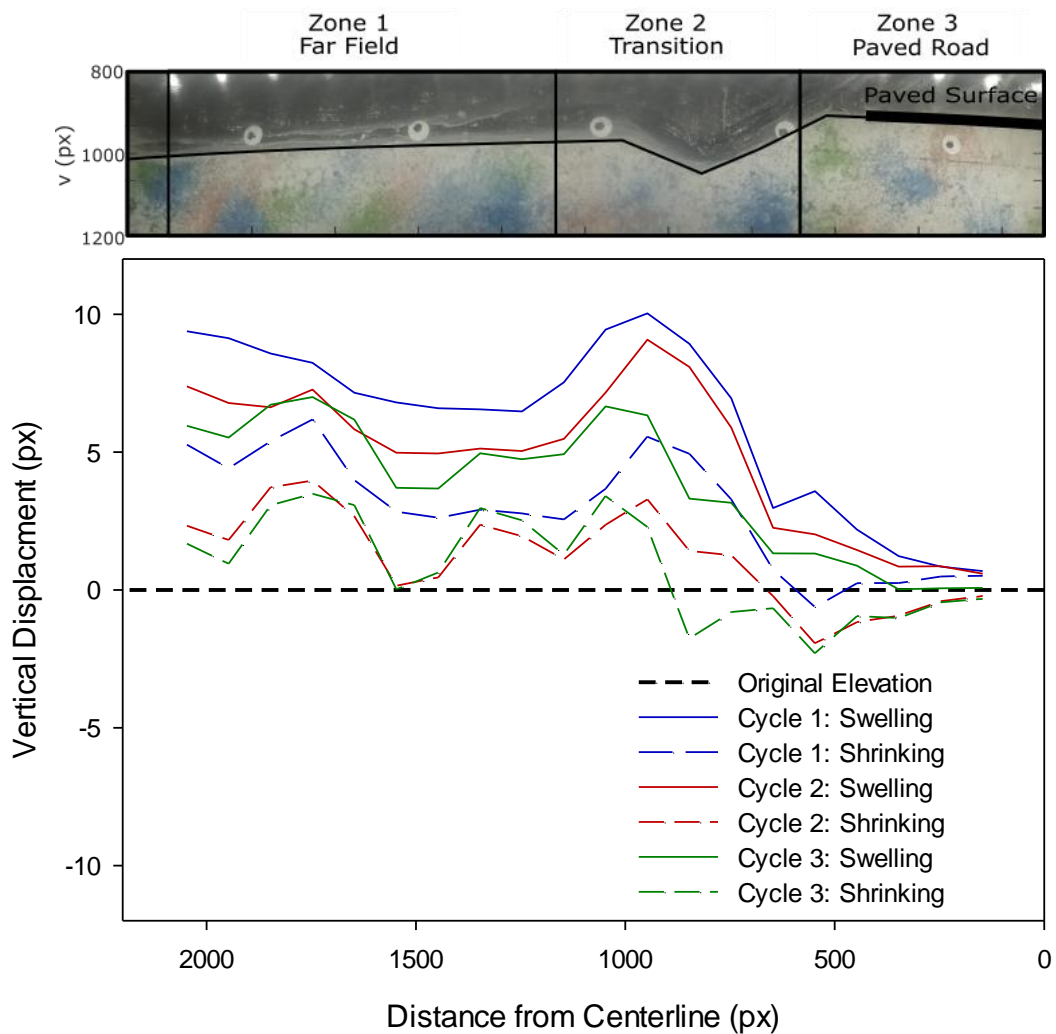


Figure 52 Test 2 Road - Vertical Displacement of Model Surface at the End of Each Cycle (Swelling/Shrinking)

Figure 53 show the regions of the models analysed for strain through their depths for Test 1. The same (Figure 45) three zones, far field, transition, and paved road, are also indicated as well as the scale. These are seen in relation to a typical image from the test. A representative column from each section is indicated by the vertical dashed line in each zone. These appear in the subsequent strain plots (Figure 56). The surface location of the road is also shown for reference.

Figure 54 and Figure 55 show contour plots of the strains throughout the Test 2 Road Model. Each cycle is shown for both swelling (Figure 54) and shrinking (Figure 55). Contours are plotted on 0.25% intervals. The extent of the wetting front can be seen by the 0.25% contour, the last contour where strain is observed. Figure 48 shows the strains through the zone of interest. For all three columns, far field, transition, and paved road all reduce to zero strain at the bottom of the zone of interest, confirming that the expansive zone is limited to this zone of interest. The strains in the far field for both the contour plots and the column strain plots similar strain patterns as those in the transition zone. Below the ditch large strains are seen at the same depths and the wetting front extends further into the soil. Below the paved road the strains approach zero towards the centerline of the road.

The gravimetric water contents taken at the end of drying Cycle 3 (Figure 55C) of Test 2 are plotted in Figure 57 for both below the far field and below the paved road. The gravimetric water contents profiles are again consistent with the results from the image analysis. Gravimetric water content reduction in the unpaved region (far field) of the model is notably larger than the reduction under the paved road, consistent with the applied suctions at these two points. There is also a larger increase in the water content through the depth of the profile. This is attributed to the increased depth of seepage from the wetting cycles.

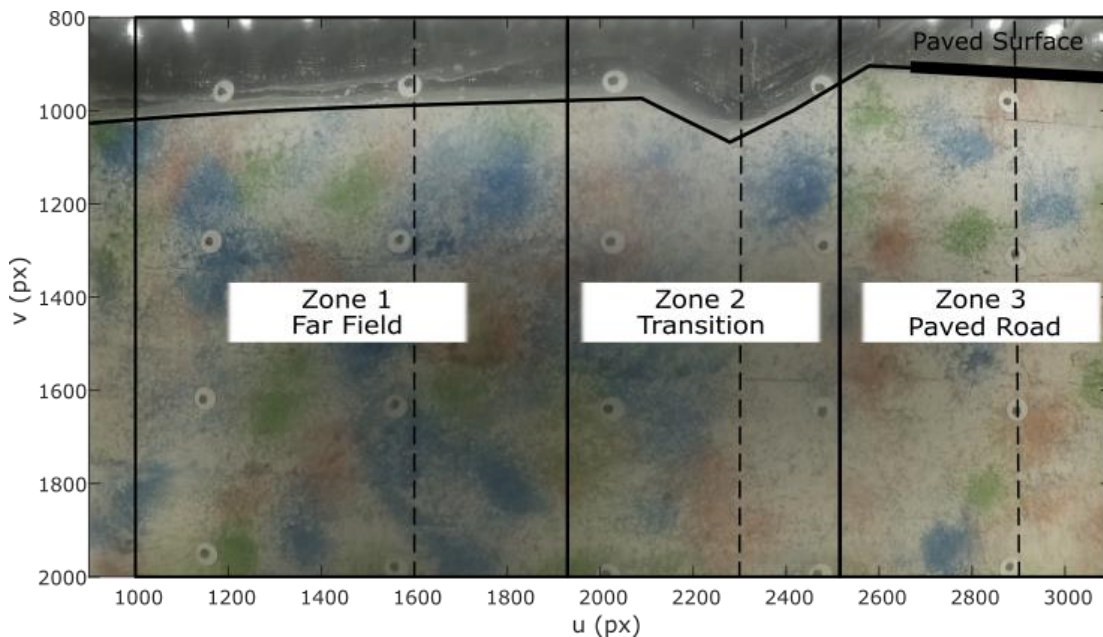


Figure 53 Test 2 Road – Surface and Zones with Image Dimensions

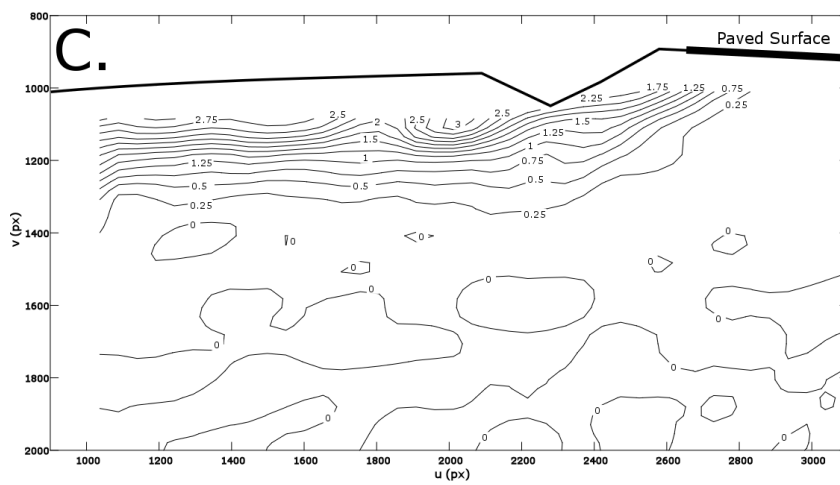
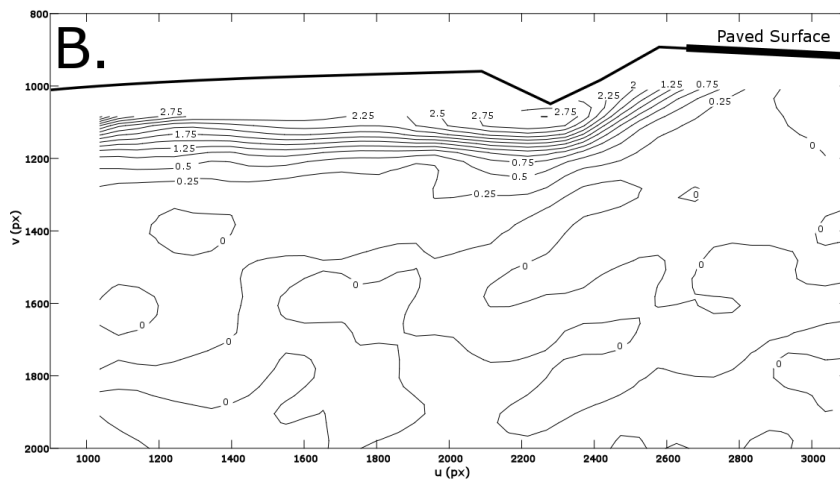
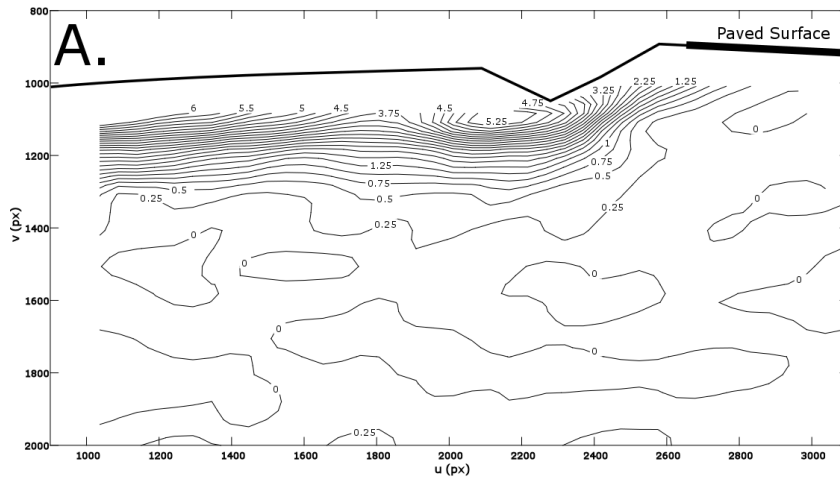


Figure 54 Test 2 Road – Swelling Strains for Cycles 1 (A), 2(B), and 3(C)

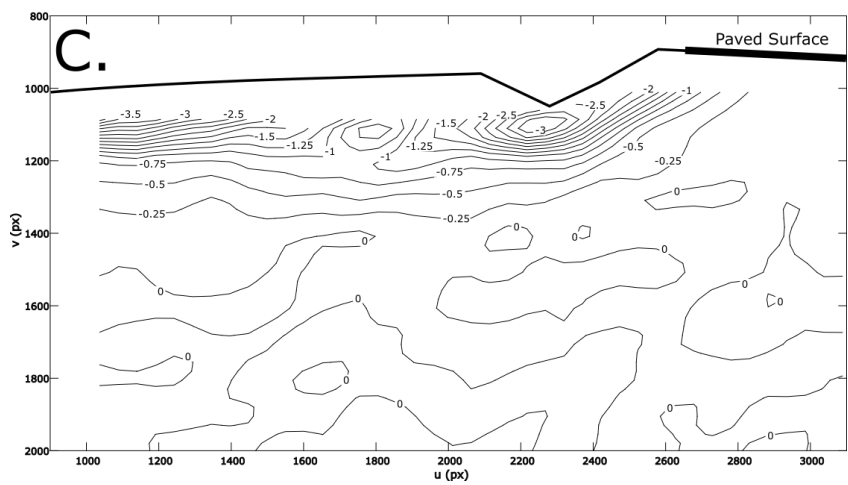
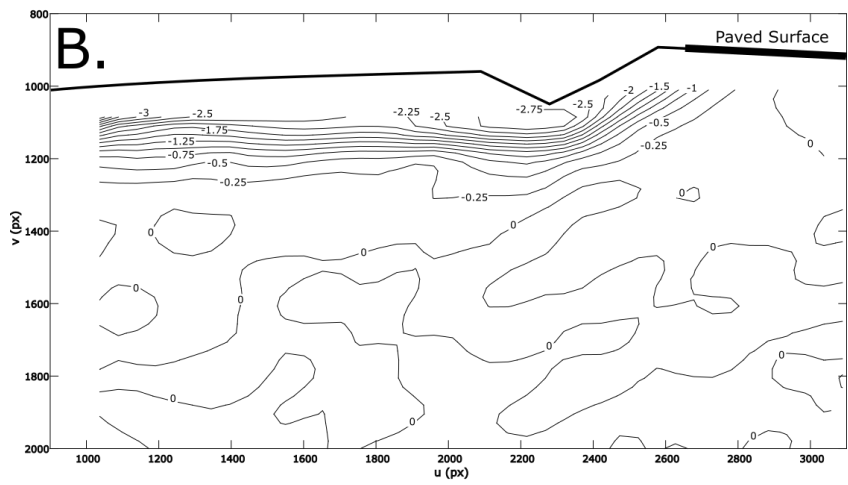
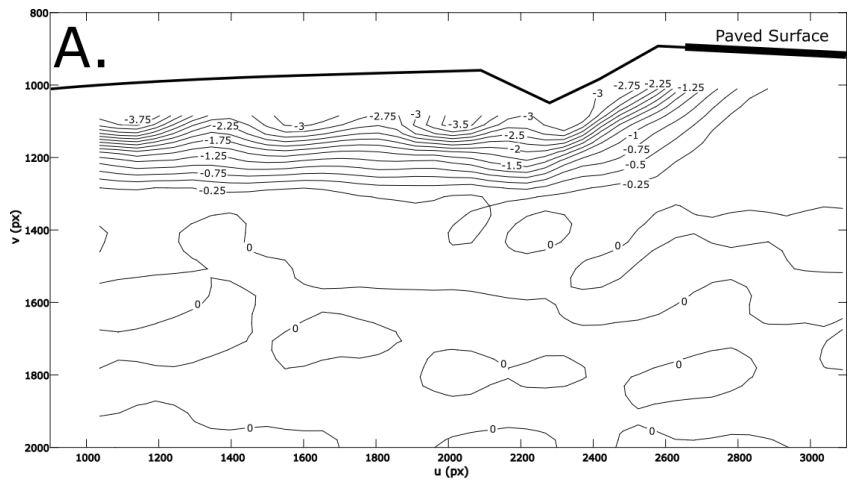


Figure 55 Test 2 Road – Shrinkage Strains for Cycles 1 (A), 2(B), and 3(C)

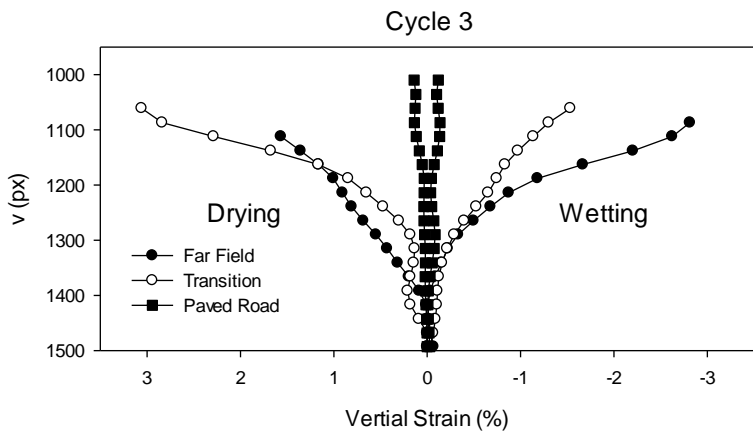
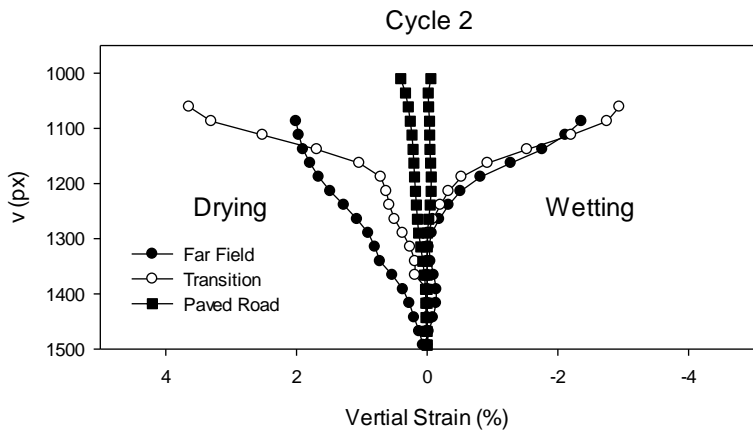
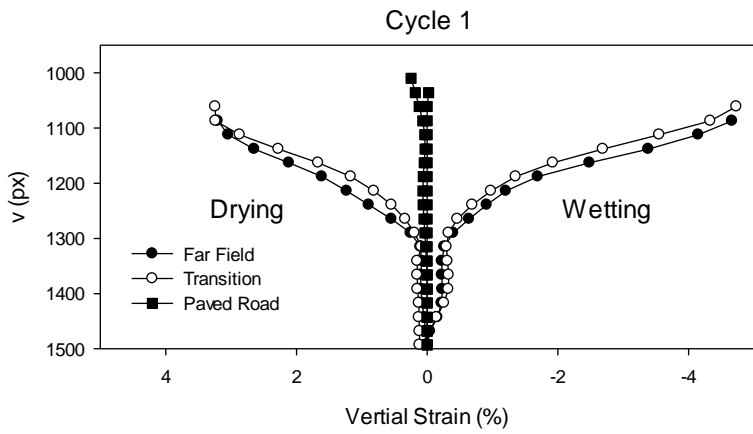


Figure 56 Test 2 Road – Vertical Strains through Expansive Zone for Representative Profile

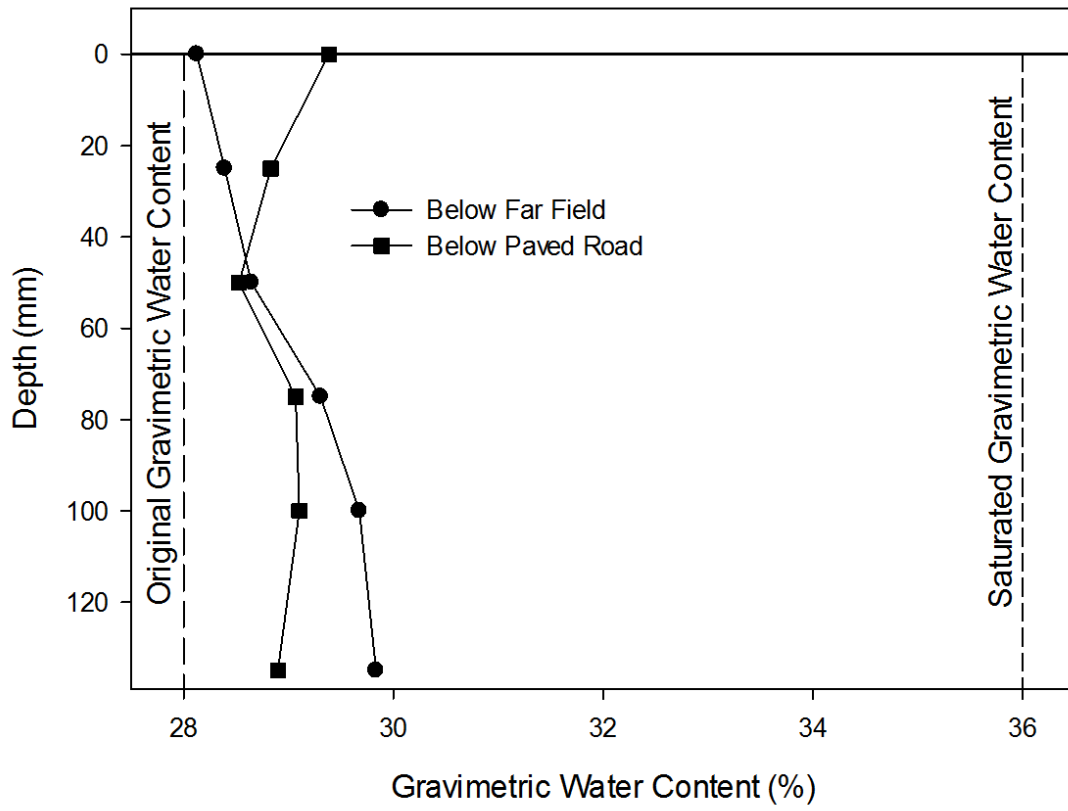


Figure 57 Test 2 Road – Water Contents with Depth at End of Drying Cycle 3

3.5 Discussion

The physical model results for idealized roads constructed in expansive soil show the effect of wetting-drying cycles on this soil-structure interaction problem. The results allow for internal comparison of the physical models to examine the impact of geometrical differences between the two cross-sections as well as with field data. In addition to the road surface displacements the physical models allow for comparison of the subsurface strains distributions, which are reflected at the surface. The results are compared with the theoretical and field behaviour of road structures constructed in expansive soils and the centrifuge physical modelling results to ascertain how closely the theoretical and observed mechanisms produced by cyclic seasonal wetting and drying can be replicated in centrifuge testing. The effects of the limitations and constraints of physical modelling, the success of the use of a remolded and mixed swelling soil, and the simplifications and variations in the design of the road are also discussed. By showing whether the behaviour of the models can reproduce the theoretical behaviour of the swelling soil and its effects on the road and by reproducing similar mechanisms as those observed in roads built on expansive clays, confidence is produced in the method. The surface behaviour observed is further investigated through a discussion of the strains below the ground surface.

3.5.1 Surface Displacement

In the field, behaviour of roads constructed on expansive soil can only be directly observed at the surface. This data is typically gathered by using surveying equipment to determine vertical displacements at points across the surface of a road (Roodi et al., 2016). This data can be used to confirm the mechanism of failure (Zornberg et al., 2009) by observing actual failures and real-world displacements. However, it is limited to a few points observed at the surface at discreet locations, and usually measured periodically over long intervals.

To confirm the behaviour of the models is representative of the effects of expansive soil on roads, similar vertical displacements of the surface of the model must be produced from the models' analyses. The general behaviour of the model is consistent with behaviour which is associated with road failure as a result of expansive soils. However, these failure mechanisms are normally described in relation to the road surface because far field measurements of displacements is difficult with survey equipment and can be eclipsed by other changes in the environment. In order to compare to data gathered at a road surface the displacements of the paved road must be evaluated. The maximum and minimum vertical displacements of the uppermost patches below the road surfaces of the Test 1 Road and Test 2 Road are plotted in Figure 58 and Figure 59. The maximum (swelling) and minimum (shrinking) vertical displacement is plotted with distance from the centreline for each testing cycle. The initial (0) road model displacement is also shown with the width of pavement for each road.

The results shown in Figure 58 and Figure 59 show very good agreement with road failure behaviour which can produce significant cracking. At the edge of the paved road width, relatively large displacements are seen in comparison to the minimal displacements toward the centreline of the road. The reduced paved portion of the road, coupled with the ditch at the base of the slope produce displacements closer to the centerline of the road and larger displacements. This is attributed to the reduced impermeable area and the increased

depth of infiltration in this region. The discussion of the model's behaviour through the depth of the expansive zone examines this in more detail. The swelling and resultant vertical displacement of the soil at points further away from the road's centreline will produce compression in the road surface while the shrinking during the drying portions produces tension in the road surface. The cyclic compression and tension produced by infiltration and evaporation cycles produces the conditions to cause damage to the road surface in the form of longitudinal cracking. The inflection point between the relative stable portion of the road and the mobile edge of the paved road is where cracks would occur. For the Test 1 Road this inflection point is nearer the edge of the road while the Test 2 Road shows a shallower increase that extends further towards the centerline; this indicates that the cracks will likely appear nearer the centerline for this road.

For comparison with field data, the displacements can be scaled to the prototype dimensions. Roodi et al., (2015) plotted cross-sections of a failed road surface which was constructed in expansive soils. These displacements were observed over a four month case study from February 2015 to June 2015 in Northern Texas. Figure 60 shows the scaled plot of the displacements from Test 1 and Test 2 previously discussed in Figure 58 and Figure 59 with the observed minimum (February) and maximum (June) displacements from the case study. Both the shape and magnitude of the displacements that produced severe cracking in the case study are congruent with the physical model data. This confirms that the displacements produced in both road models tests can be expected to produce the damage described in Figure 22 and failures like those seen in Figure 23.

The behaviour of the surface of the paved road is consistent with both the theory and observed case study behaviour of roads constructed in expansive clay (Zornberg et al., 2009, Roodi et al., 2016). However, this is the limit of the data provided by the field data. The centrifuge modelling and analysis of the models with PIV allow observation of the behaviour of the road through the depth of the soil. This deepens the understanding of the mechanism from only surface observations to the behaviours of the soil throughout its profile.

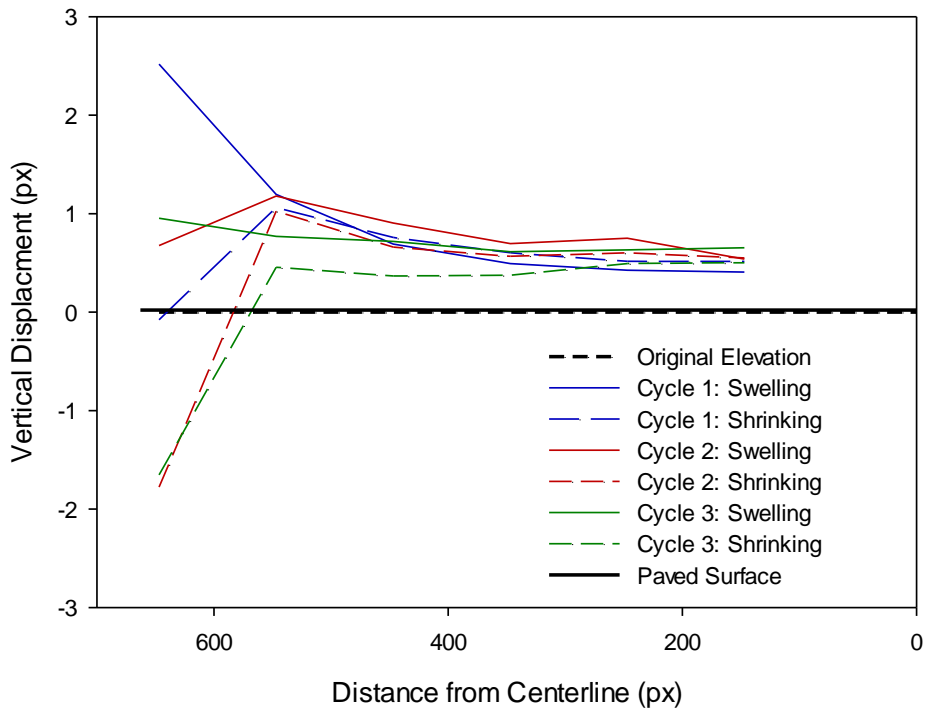


Figure 58 Test 1 Road - Vertical Displacement of Pavement (Swelling/Shrinking)

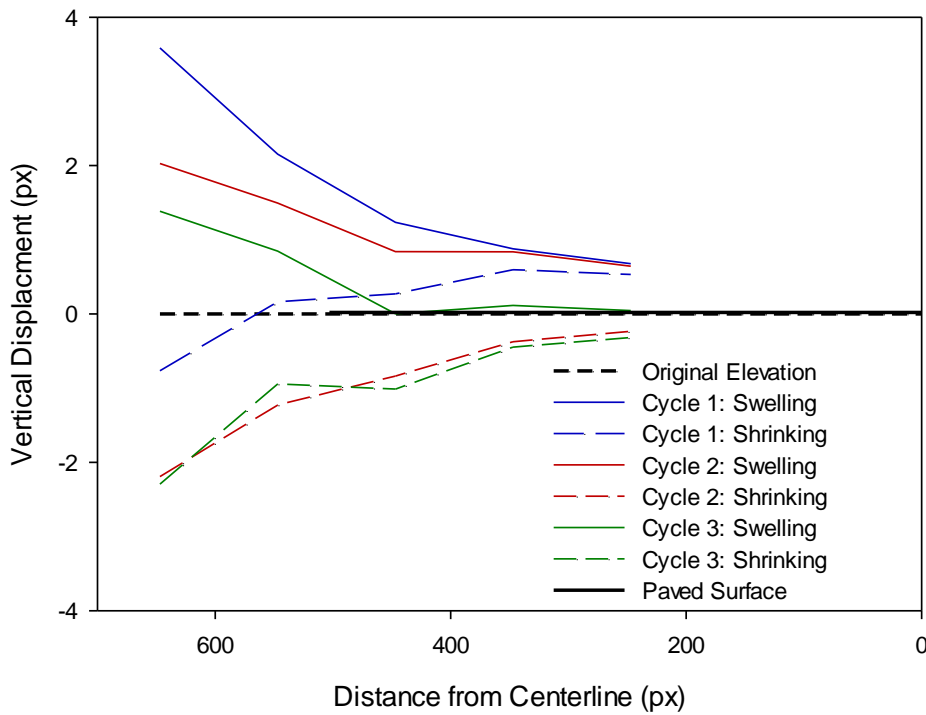


Figure 59 Test 2 Road - Vertical Displacement of Pavement (Swelling/Shrinking)

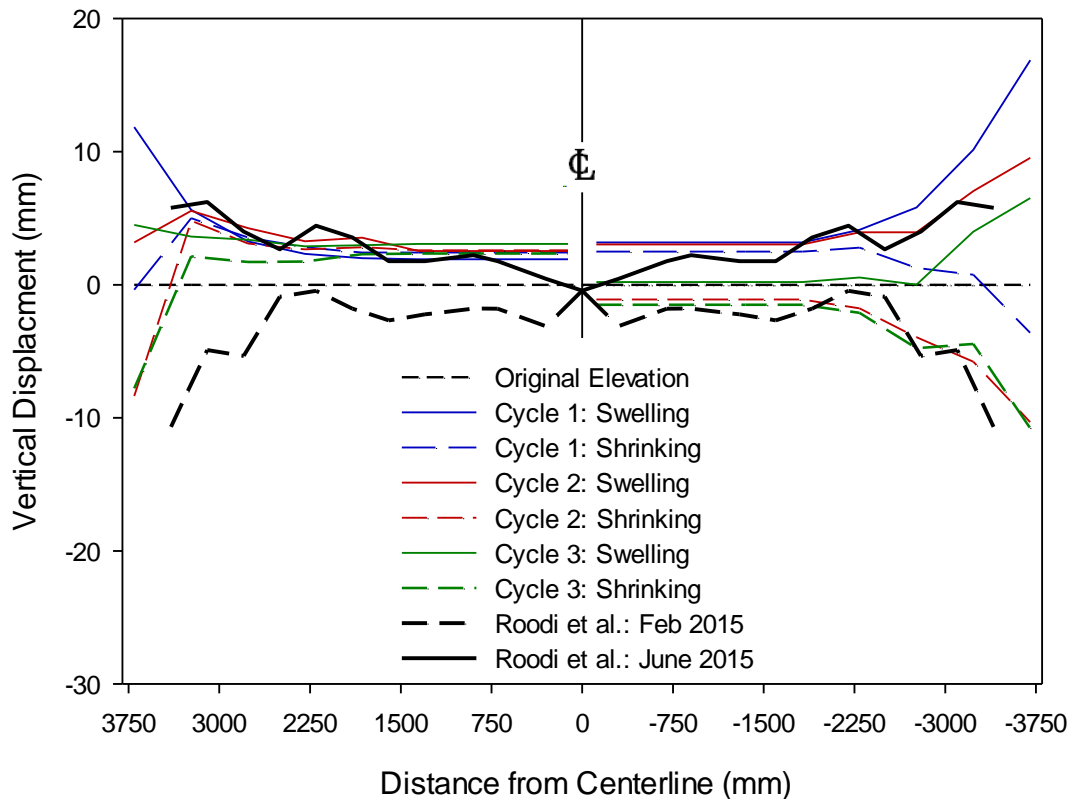


Figure 60 Test 1 Road (Left) and Test 2 Road (Right) - Vertical Displacement of Pavement (Swelling/Shrinking) with Typical Case Study Values (Roodi et al., 2016)

3.5.2 Soil Profile Strains

The initial data produced by the image analysis of the models is in the form of vertical displacements. PIV also produces a triangular strain matrix of the region of interest based off of the uv displacement data. The critical behaviour that drives the failure mechanism is the depth of infiltration into the soil and the extent the wetting front progresses under the road. Horizontal infiltration into the slope appears to be the driving cause of the swelling behaviour at the road surface, producing the damaging displacements. Because changes in saturation, producing changes in suction, occur up to the limit of the wetting front, it is possible to determine the extent of the wetting front by the limit of the strain in the soil. During the drying phase, the extent of the effect of the applied surface suction through the soil can also be determined by the limit of the strain within the soil.

To determine the extent of the wetting and drying fronts under the paved road surface this limit of the strain was determined for each cycle of both tests. The limit of the strain was

assumed to be the 0.25% contour. The Test 1 and Test 2 contour plots show the 0.25% contour for each of the tests in Figure 46 and Figure 47 for Test 1 and Figure 54 and Figure 55 for Test 2. Initially the 0% strain contour was thought to be optimal but, due to background noise in the image analysis, the 0% contour covers the immobile portion of the models, which is below the expansive zone and under the paved surface. Therefore it cannot be used to delineate the extent of the strain. The 0.25% contour is indicative of the limit of strains and thus is a clear indication of the extent of the wetting front.

Figure 61A and Figure 61B show the extent of the wetting and drying fronts below the Test 1 Model Road respectively. They plot the 0.25% strain contour from each cycle in the road models. In Road Test 1, the wetting front for Cycle 1 extends the furthest of the three cycles and the limit of the strains by the paved road can be seen. The horizontal penetration of the wetting front extends slightly below the paved surface. This corresponds with the highest displacement data for the three wetting cycles in the Test 1 Road. The extent of the wetting front also corresponds with the inflection point in the surface displacement curve (Figure 44) where cracks are likely to occur. The vertical depth of the wetting fronts below the transition zone, controlling the magnitude of the displacements in the transition zone, are consistent and reduce under the road surface. The following two cycles show repeating swelling and shrinking strains as the ground responds to subsequent wetting and drying events.

Figure 61C and D show the extent of the wetting and drying fronts for Test 2. When compared with Test 1, the notable difference is the greater horizontal penetration of the wetting front below the road. A second difference is the depth of the wetting front is increased near the road. This produces the twofold effect of increased magnitude of deformations and their presence closer to the centerline of the road. This change in shape moves the inflection point in the surface displacement curve closer to the middle of the road. From a trafficability perspective the cracking location is now within the lane of traffic making it much more dangerous.

The two modifications made to the road design work in concert to move the inflection point from the shoulder into the roadway. Because the ditch collects water longer than the duration of the ponding on the far field, a greater volume of water is available for the soil below and around the ditch for a longer period of time. This produces a greater depth of saturation around the ditch and increases swelling strains. The reduced paved width of the road and exposed shoulder allow further penetration of the wetting front under the road surface. This is reflected by the more gradual gradient in the vertical displacements across the paved surface of the road.

The drying cycles for Test 2 show a similar increased depth of changes in suction. The ditch geometry increases the surface area and reduces the distance from the surface around the ditch. The reduced shoulder also promotes a greater extent of increased suction and shrinkage strain under the road. These shrinking strains, combined with the swelling strains, give a greater range of movement and further contribute to the road failure. While the Test 1 Model and Test 2 Models both show the failure mechanism behaviour, the ditch and reduced pavement exacerbate these by providing more water near the side of the road and giving both infiltration and evaporation greater access to the soil towards the centerline of the road.

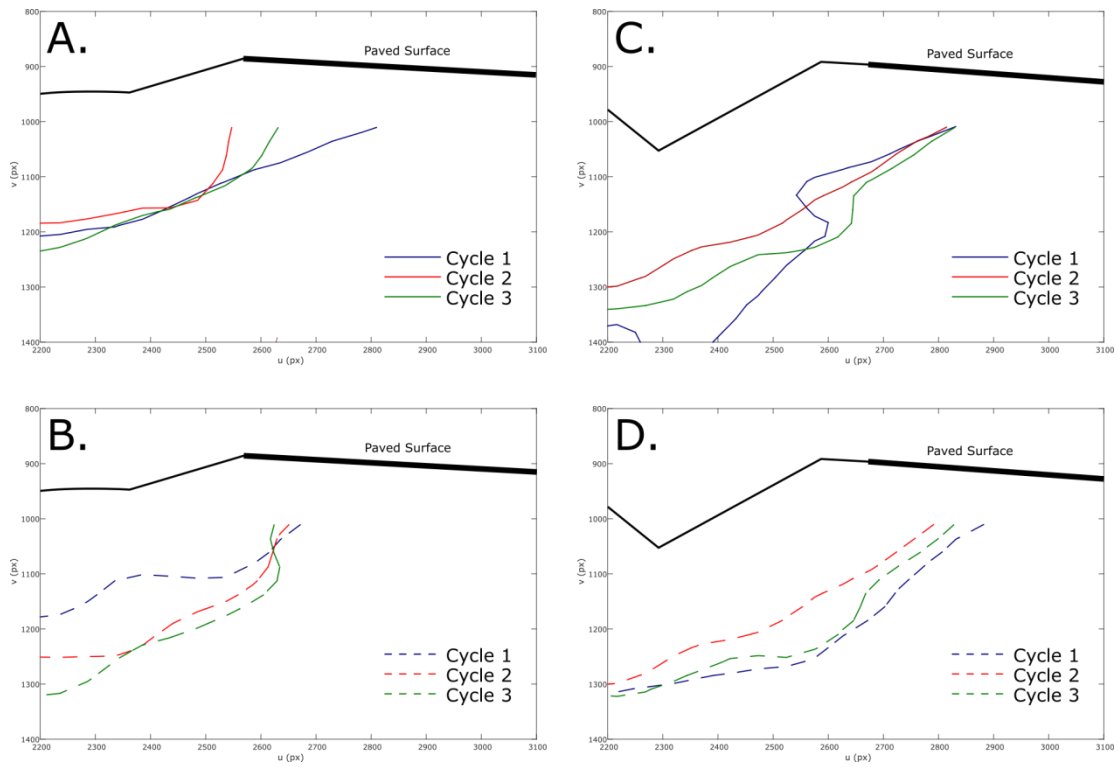


Figure 61 Test 1 Road Swelling (A) and Shrinking (B) and Test 2 Road Swelling (C) and Shrinking (D) - Limit of Strains below Road Surface

3.6 Summary

The expansive soil physical models demonstrate the ability to reproduce field behaviour of prototype roads constructed in swelling soils. The significant road surface vertical displacements observed during cyclic wetting-drying cycles demonstrate the success of this method in modelling expansive soils. The wetting cycles produced consistent responses within the expansive zone and the drying cycles effectively produce shrinking due to atmospheric conditions. The centrifuge controls provide good control and monitoring of these effects while the collection of image data and the PIV analysis provides an excellent method of observing and analyzing the model's behaviour. The PIV analysis allows for gathering of surficial data for comparison with field data as well as understanding of the underlying swelling/shrinkage mechanisms reflected at the surface. This methodology can easily be adapted for future testing with either modified mixed expansive soil or with remolded clays from prototype in-situ soils to examine a wider range of behaviour.

The road's relative displacement across its paved surface display the same surficial displacement behaviour as the predicted failure mechanism (Zornberg et al., 2009) as well as those observed to produce severe cracking in case studies (Roodi et al., 2016). The impervious road's minimal responses close to the centerline and the significant displacements at the edge of road accurately model the observed field behaviour that produces cracking in road surfaces. More complex and site specific roads could be modelled using this technique to further understand the implications of variations of construction methods and infiltration and evaporation cycles. The possibility of analysis of the model below the surface contributes significantly to the understanding of the road behaviour and its failure mechanisms over the existing methods of collecting field data on surface displacements. This extends the reach of engineers from only seeing surface behaviour in fields studies to observing the whole structure.

These results confirm that the method provides new understanding to the failure mechanism of roads constructed in expansive soil and that it can be applied to produce useful results in further understanding of the expansive soil behaviour and failure mechanisms that control road performance in areas where swelling soils are present. The tests conducted and analyzed in this chapter provide a strong basis for further development and specialization of the methodology presented here for future research.

Chapter 4

Conclusion

The utility of RMCC's centrifuge as a help to geotechnical engineers in being able to predict and interpret the behaviour of geotechnical problems is well established by the results of these two papers. The initial centrifuge confirmatory testing demonstrated with the first paper (Chapter 2) sets the groundwork the use of the centrifuge for research. The second paper (Chapter 3) shows application of the successes of the research from the first paper. The development of the centrifuge is confirmed by the modelling of geotechnical structure that makes extensive use of the equipment and methodology previously proved. The results not only establish the accuracy of the methods and equipment but the invaluable detail of results that is uniquely obtainable through centrifuge testing.

The first paper demonstrates that the centrifuge can be used to replicate geotechnical structure behaviour at various scales. The results show that the slope and bearing capacity models agree with equivalent theoretical solutions and the modelling of models exercise shows that models tested over the range of the centrifuge's limits produces accurate and consistent results. These tests provide confidence in future use of the RMCC centrifuge in research to examine the scaled behaviour of geo-materials and structures. The slope and strip footing tests, with their associated methods and equipment, provide confidence in the use of the centrifuge and the data it produces. These results provide a solid foundation upon which future research, development, and application can be built with confidence in its results.

The second paper builds on the success of the methods and principles established by the first paper. The benefits are seen through the success of modelling the more complex expansive soil structure subjected to cyclic wetting and drying. The design, construction, and testing of expansive soil through the application of cyclic seasonal conditions produce behaviour that is consistent with the complex behaviour seen in roads constructed in expansive soil. The results produced by the testing of the road show the volumetric strain effects of wetting-drying cycles on this soil-structure interaction problem. These results are shown to be congruent with previously suggested theoretical failure mechanisms. The behaviour also closely corresponds with the surficial data gathered in field studies that were linked to this failure mechanism. The road structures constructed on the expansive soil shows very good agreement with road failure behaviour which produces significant cracking in prototype roads.

The accuracy of the surface data produced by the road models permits expanded insight into the model behaviour which can be extrapolated to explain prototype behaviour. The benefit of the centrifuge in accurately reproducing the data that can be gathered from field studies is increased by also providing information on those regions of the structure that are extremely difficult or impossible to observe in full scale prototypes. The critical behaviour that drives the failure mechanism is the depth of infiltration into the soil and the extent to which the wetting front progresses under the road. The mechanism producing road failure and the impact of modifications to road design can uniquely be observed in the centrifuge models, in a way that is impossible in the field. The behaviours throughout the profile of the

structure can be observed and investigated to further expand understanding of the behaviour of geotechnical structures.

This success of the modelling can be extended to broader testing of various geotechnical structures as well as specialized to observe unique conditions and geotechnical designs. Further development of the data collection, climate and weather effects, and modifications to the road design will provide still greater insight into the mechanisms within geotechnical structures. The results show the advantages of physical modelling with a centrifuge. It is rapid, cost effective, and gives access to great depth of data provided through real observation of the structure's behaviour while maintaining flexibility and control over stress history, materials, and climatic conditions.

The success of the modelling undertaken in this thesis substantiates integrated physical modelling of geotechnical structures as an ideal tool for provision of knowledge on their behaviour. Application of the methods to testing of various complex geotechnical materials, structures, and mechanisms will allow for consistent, detailed data to be generated for the range of problems facing geotechnical engineers. The successful modelling of both idealized and increasingly complex geotechnical structures and mechanisms shown affirms the centrifuge is an invaluable tool for teaching and future research at the Royal Military College of Canada and other institutions utilizing geotechnical centrifuges.

References

- ASTM D698-12e2 Standard Test Methods for Laboratory Compaction Characteristics of Soil Using Standard Effort (12 400 ft-lbf/ft³ (600 kN-m/m³)), ASTM International, West Conshohocken, PA, 2012, <https://doi.org/10.1520/D0698-12E02>
- ASTM D2487-11 Standard Practice for Classification of Soils for Engineering Purposes (Unified Soil Classification System), ASTM International, West Conshohocken, PA, 2011, <https://doi.org/10.1520/D2487-11>
- ASTM D4943-08 Standard Test Method for Shrinkage Factors of Soils by the Wax Method, ASTM International, West Conshohocken, PA, 2008, <https://doi.org/10.1520/D4943-08>
- Bowles, J.E. 1968. *Foundation Analysis and Design*, McGraw-Hill, New York, NY, USA.
- Boadbent, Inc. 2015. *Broadbent Operating Manual*, Thomas Broadbent & Sons Ltd., Huddersfield, England.
- Chowdhury, Rashedul H., and Shahid Azam. "Unsaturated shear strength properties of a compacted expansive soil from Regina, Canada." *Innovative Infrastructure Solutions* 1.1 (2016): 47.
- Coating Industry News. "Extreme Drought Damaging MS Roads." *PaintSquare*, 06 Dec. 2016, www.paintsquare.com/news/?fuseaction=view&id=15901. Accessed 06 Mar 2017.
- Das, B.M. 2016. *Principles of Foundation Engineering*. 8th ed., Cengage Learning, Boston, MA, USA.
- Fredlund, Delwyn G., Murray D. Fredlund, and Harianto Rahardjo. *Unsaturated soil mechanics in engineering practice*. Hoboken, N.J: Wiley, 2012. Print.
- Fredlund, Delwyn G. "Geotechnical Problems Associated with Swelling Clays." *Vertisols and Technologies for their Management*, edited by N. Ahmad, and A. Mermut, Elsevier, pp. 1996, 499-524.
- Fredlund, Delwyn G., et al. "Determination of water storage and permeability functions for oil sands tailings." *Proceedings of the Tailings and Mine Waste Conference, Vancouver, BC*. 2011.
- Gadre, A. D., and V. S. Chandrasekaran. "Swelling of black cotton soil using centrifuge modeling." *Journal of geotechnical engineering* 120.5 (1994): 914-919.
- Garnier, Jacques, et al. "Catalogue of scaling laws and similitude questions in geotechnical centrifuge modelling." *International Journal of Physical Modelling in Geotechnics* 7.3 (2007): 1.

Government of Canada. "Canadian Climactic Norms Station Data: Regina International Airport." *Government of Canada*, 19 April 2016, http://climate.weather.gc.ca/climate_normals/results_1981_2010_e.html. Accessed 10 Mar 2017

Ito, Maki, Shahid Azam, and Yafei Hu. "A two stage model for moisture-induced deformations in expansive soils." *Environmental Systems Research* 3.1 (2014): 19.

Kingswood, J., LaPorte, S, Siemens, S., 2016. "Verification of physical modelling with a geotechnical centrifuge using physical models of slope stability and bearing capacity." *In: Proceedings of the 69th Annual Canadian Geotechnical Conference*. Vancouver, Canada.

Kimura, T., O. Kusakabe, and K. Saitoh. "Geotechnical model tests of bearing capacity problems in a centrifuge." *Geotechnique* 35.1 (1985): 33-45.

Lin, Botao, and Amy B. Cerato. "Hysteretic soil water characteristics and cyclic swell–shrink paths of compacted expansive soils." *Bulletin of Engineering Geology and the Environment* 72.1 (2013): 61-70.

Lim, B. F. and Siemens, G. A. "An Unconfined Swelling Test for Clayey Soils That Incorporates Digital Image Correlation," *Geotechnical Testing Journal*, Vol. 36, No. 6, 2013, pp. 823-833, <https://doi.org/10.1520/GTJ20120220>. ISSN 0149-6115

Lyndon, A., and A. N. Schofield. "Centrifugal model tests of the London landslide." *Canadian Geotechnical Journal* 15.1 (1978): 1-13.

Madabhushi, G. 2015. *Centrifuge Modelling for Civil Engineers*, CRC Press, Boca, Raton, FL, USA.

McCudden, Jenny. "Flood misery continues for homeowners." *BBC News*, 20 Jan. 2001, http://news.bbc.co.uk/2/hi/uk_news/1120108.stm. Accessed 28 Feb 2017.

Muntohar, Agus Setyo. "Swelling and compressibility characteristics of soil-bentonite mixtures." *Dimensi Teknik Sipil* 5.2 (2003): 93-98.

PaintSquare. "Extreme Drought Damaging MS Roads." *PaintSquare*, 06 Dec. 2016, <http://www.paintsquare.com/news/?fuseaction=view&id=15901>. Accessed 06 Mar 2017.

Plaisted, M. D., and J. G. Zornberg. "Testing of an expansive clay in a centrifuge permeameter." *Proceedings of the 7th International Conference on Physical Modelling in Geotechnics*. 2010.

Prakash, K. and Sridharan, A. "Free Swell Ratio and Clay Mineralogy of Fine-Grained Soils," *Geotechnical Testing Journal*, Vol. 27, No. 2, 2004, pp. 220-225, <https://doi.org/10.1520/GTJ10860>. ISSN 0149-6115

- Powell, J. S., et al. "Characterizing the swelling potential of Bearpaw clayshale." *Engineering Geology* 158 (2013): 89-97.
- Puppala, Anand J., et al. "Threshold moisture content and matric suction potentials in expansive clays prior to initiation of cracking in pavements." *Canadian Geotechnical Journal* 48.4 (2011): 519-531.
- Puppala, Anand J., Thammanoon Manosuthikij, and Bhaskar CS Chittoori. "Swell and shrinkage characterizations of unsaturated expansive clays from Texas." *Engineering Geology* 164 (2013): 187-194.
- Roodi, G. H., J. R. Phillips, and J. G. Zornberg. "Evaluation of Vertical Deflections in Geosynthetic Reinforced Pavements Constructed on Expansive Subgrades." *Proceeding of the 3rd Pan-American Conference on Geosynthetics, Geo-Americas 2016*. 2016.
- Roscoe, K. H. "The influence of strains in soil mechanics." *Geotechnique* 20.2 (1970): 129-170.
- Siemens, Greg, and James Blatz. "Triaxial apparatus for applying liquid infiltration with controlled boundary conditions and internal suction measurement." *Journal of geotechnical and geoenvironmental engineering* 133.6 (2007): 748-752.
- Siemens, G. A., S. B. Peters, and W. A. Take. "Comparison of confined and unconfined infiltration in transparent porous media." *Water Resources Research* 49.2 (2013): 851-863.
- Stanier, S.A., Blaber, J., Take, W.A., and White, D.J. 2015. Improved image-based deformation measurement for geotechnical applications. *Canadian Geotechnical Journal*, 53(5): 727-739.
- US Climate Data. "Climate Oklahoma - Oklahoma City." *US Climate Data*, 2017, <http://www.usclimatedata.com/climate/oklahoma/united-states/3206>. Accessed 10 Mar 2017
- US Climate Data. "Climate Texas- Austin." *US Climate Data*, 2017, <http://www.usclimatedata.com/climate/austin/texas/united-states/ustx2742>. Accessed 10 Mar 2017
- Take, W. A., and M. D. Bolton. "An atmospheric chamber for the investigation of the effect of seasonal moisture changes on clay slopes." *Proc., Int. Conf. on Physical Modeling in Geotechnics*. Rotterdam, The Netherlands: Balkema, 2002.
- Taylor, D.W. 1948. *Fundamentals of Soil Mechanics*, John Wiley & Sons, New York, NY, USA.
- Terzaghi, K. and Peck, R.B. 1967. *Soil Mechanics in Engineering Practice*, 2nd ed., John Wiley & Sons, New York, NY, USA.

White, D. J. "Contributions to Géotechnique 1948-2008: Physical Modelling." *Géotechnique* 58.5 (2008): 413-422.

White, D. J., W. A. Take, and M. D. Bolton. "Soil deformation measurement using particle image velocimetry (PIV) and photogrammetry." *Geotechnique* 53.7 (2003): 619-632.

Wilson, G. W., D. G. Fredlund, and S. L. Barbour. "The effect of soil suction on evaporative fluxes from soil surfaces." *Canadian Geotechnical Journal* 34.1 (1997): 145-155.

Zornberg, Jorge G., et al. *Implementation of Centrifuge Testing for Swelling Properties of Highly Plastic Clays*. No. FHWA/TX-13/5-6048-01-1. 2013.

Zornberg, J. G., and R. Gupta. "Reinforcement of pavements over expansive clay subgrades." *Proceedings of the 17th International Conference on Soil Mechanics and Geotechnical Engineering*. Vol. 1. 2009.

Appendices

Appendix A

Cradle Base Suction and Pressure Control

One way of controlling the lower boundary of the model when the model is unsaturated and suctions or pressures are being observed is to control a water table within the model. A standpipe and water supply apparatus is affixed to the side of the cradle (Figure 62A) with access to filter stones placed across the base of the cradle. The standpipe is constructed with its outlet 25mm above the base of the cradle creating a water table at that level. A low flow of water is then supplied through the central axis of the centrifuge to ensure that the standpipe does not empty either by a decrease in water in the model or through evaporation in the standpipe. The apparatus was tested with a simple Godfrey silt sample (Figure 63) at both 10g and 40g. The sample was initially dry and accelerated to an N of 40; at this point the standpipe was filled with water and allowed to remain full. The initial saturation and steady state of the capillary zone (Figure 63A) can be clearly seen in the darker saturated silt. When the model was decelerated to an N of 10, the scaling of the capillary zone was reduced by $\frac{1}{4}$ (10g/40g) and the rise exceeded the height of the model, saturating the entire sample (Figure 63B). Therefore, this method cannot be used on fine grain soils unless the N is sufficiently high to scale the saturated capillary zone below the surface of the sample without saturating the sample from below.

A second method of controlling the lower boundary condition is to determine the suction produced by the RH as a function of water content and air pressure (Fredlund et al. 2012) at the lower boundary. This was achieved by the use of a similar apparatus and method used for the water table. A pipe is attached to the outlet at the bottom of the cradle in communication with dry filter stones. The other end of the pipe communicates with a flexible container (balloon) (Figure 62B) within a rigid 3D printed PLA mount. This allows air pressure to remain constant (with small changes in air volume) at the base of the model while ensuring that the RH remains constant, controlled by the water content of the soil.

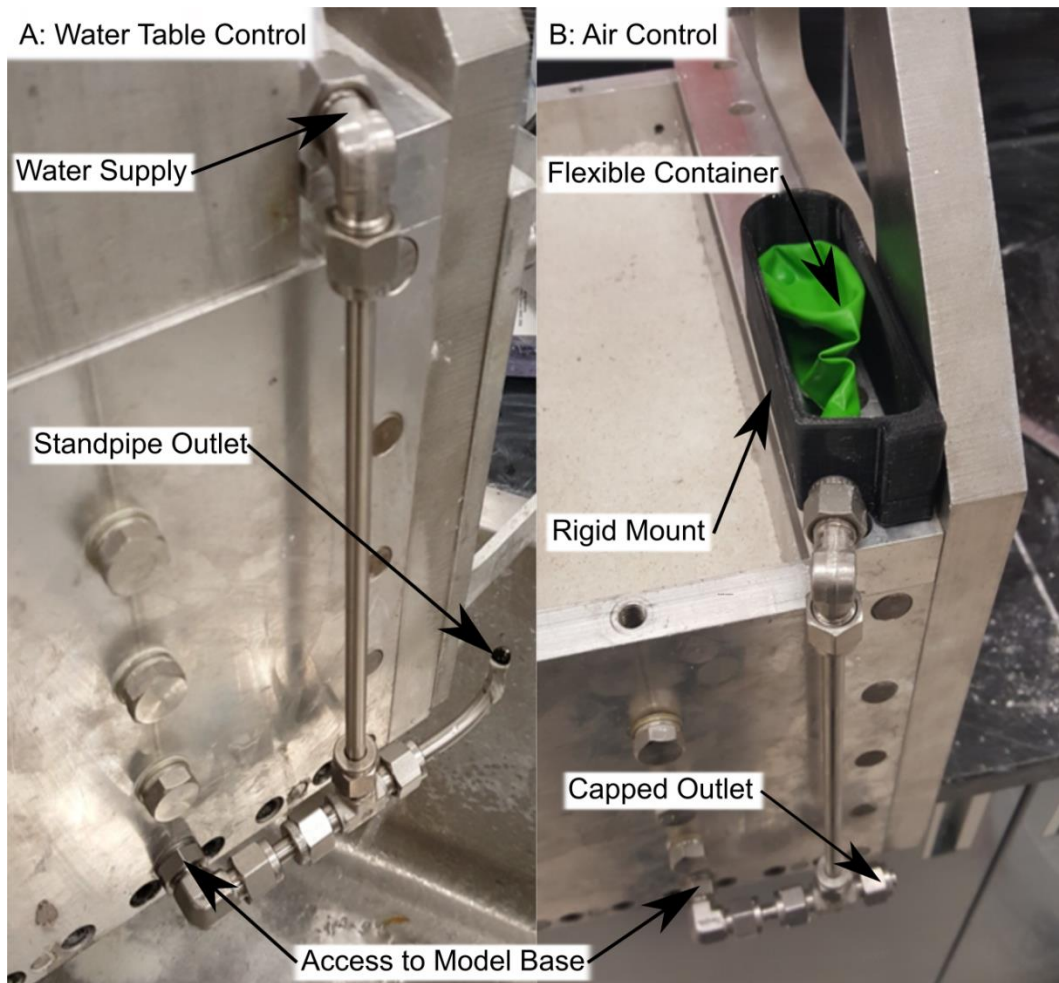
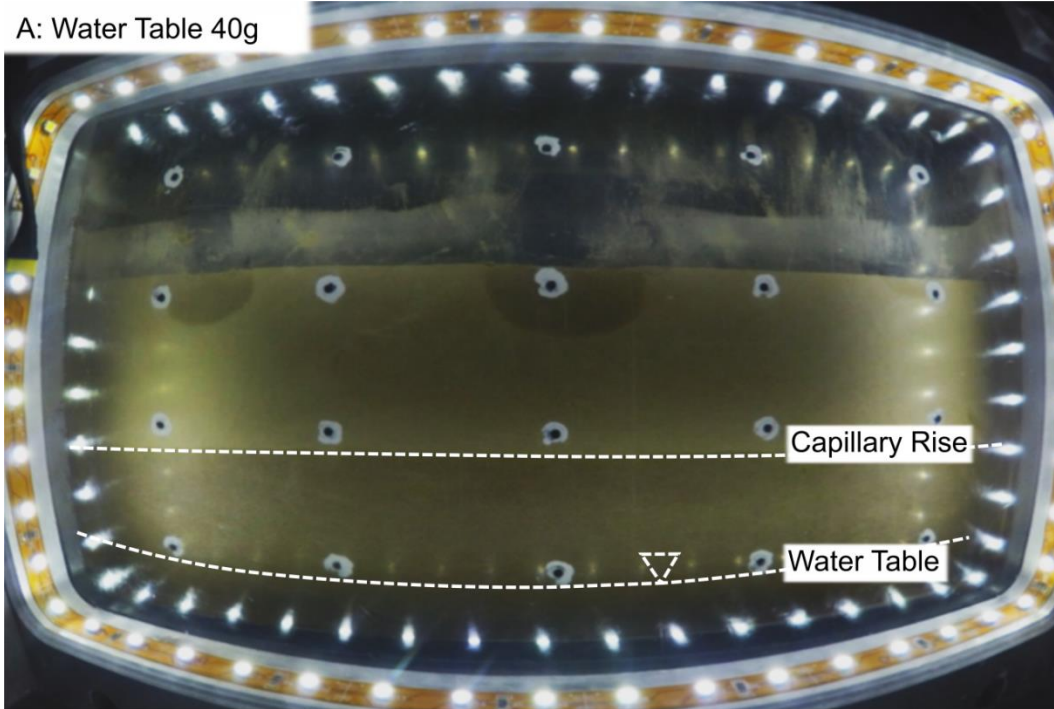


Figure 62 (A) Standpipe and (B) Air Control Apparatus

A: Water Table 40g



B: Water Table 10g

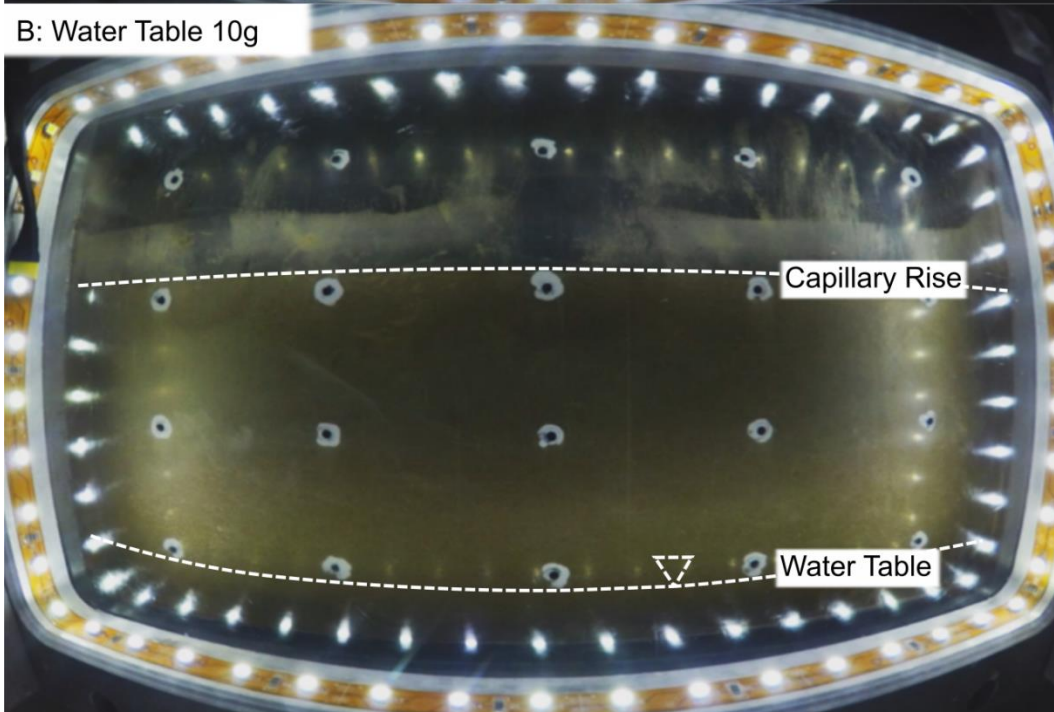


Figure 63 Water Controlled Capillary Rise at (A) 10g and (B) 40g

Appendix B

Atmospheric Control and Monitoring

For studies of infiltration into unsaturated soils and to induce flow within saturated soil models the ability to introduce water in the form of simulated rainfall is critical. Using the conduits through the stack of the centrifuge and an atmospheric control table affixed to the top of cradle (Figure 64) rainfall through three Continental PCMK-25 misting nozzles. The three nozzles were set approximately 100mm above the anticipated model surface which, assuming a 45° spray angle, gives each nozzle a 100x100mm (or 1/3rd) portion of the 300x100mm sample surface. The three nozzles can then provide an even distribution of water across the surface of a model within the cradle while the misting spray minimizes the size of drops to accommodate the scaling of the drops and minimize their impact. In order to calibrate the nozzles for use, a test was run at 40g with the nozzles. The pressure of the water supplied through the central axis was held at 70kPa using a pressure vessel outside the centrifuge. A plastic tray with 18 equal partitions in the surface (Figure 65) was inserted into the cradle at 135mm from the bottom of the cradle to simulate the height of the surface of a sample. Once the centrifuge had reached the required acceleration the water supply was opened into the conduit for 120 seconds. The centrifuge was stopped and the mass of the water collected in the trays was determined to be approximately 117g; accounting for some minor leakage around the trays. The flow rate of the apparatus for 40g and 70kPa was determined to be 60ml/min. The distribution within the trays was also observed to determine if the spray pattern for the nozzles and the Coriolis Effect on the falling droplets would affect the distribution. The trays demonstrated an even distribution of water among all the tray partitions and no significant area collecting a disproportionate amount of the simulated rainfall.

Not only is the control of infiltration conditions important to testing but also the rate at which evaporation from the model occurs. A Vaisala HMP110T relative humidity (RH) and temperature probe is mounted on a 3D printed PLA cradle on top of the atmospheric control table (Figure 64) and provides current atmospheric conditions near the surface of models within the centrifuge through the Aclipse DAS software. The sensor was calibrated using salt solutions and provides RH values within 1% for most operating ranges of the centrifuge.

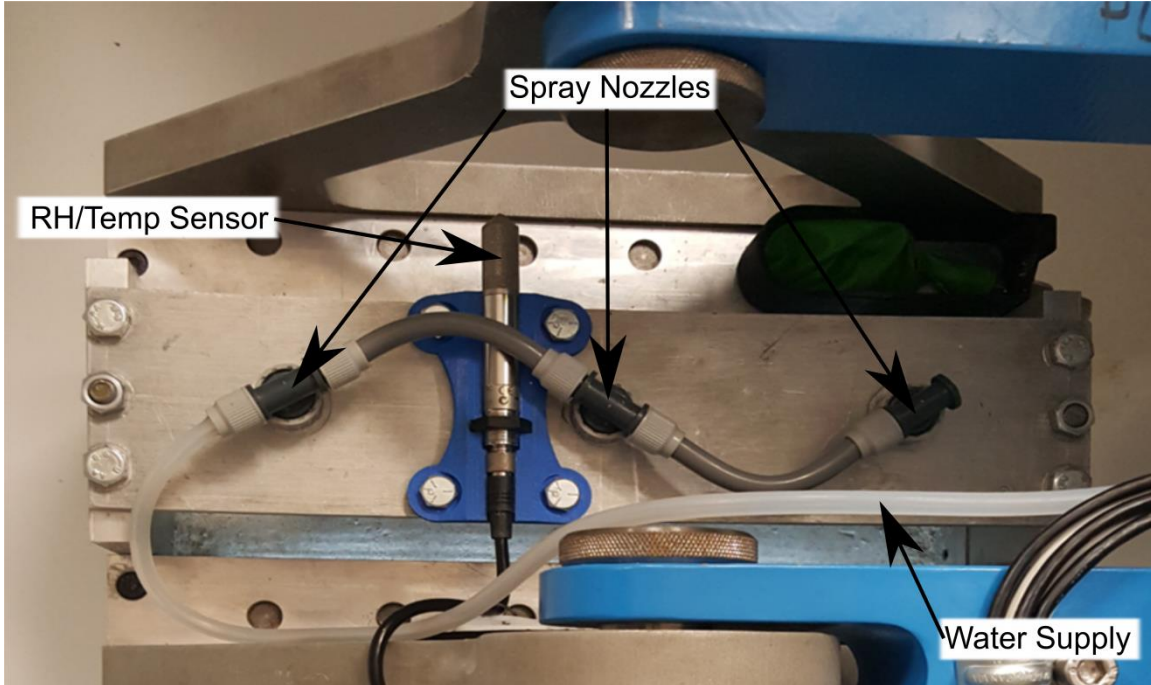


Figure 64 Atmospheric Control Table with RH and Temperature Sensor in Cradle



Figure 65 Collection Tray Arrangement

Appendix C

Particle Image Velocimetry RG Analysis

D.1 Introduction

Particle Image Velocimetry (PIV) RG analysis is described by Stanier (et al., 2005). It is an improved version of previous PIV iterations and provides greater accuracy, improved user interface, and further tools for data analysis. This appendix provides a typical analysis used for the results described in the previous chapters.

D.2 Mesh and Control Point Generation

A .mat file (Figure B1) with physical x and y coordinates of control points in millimeters is loaded into the workspace. The “**geoCENTROID_RG**” subroutine prompts the user to select centers and parameters for identification of each control point and generates a file with coordinates of each point with the xy coordinates from the .mat file and the uv coordinates from the user input. These are corrected and calibrated by the subroutine to find the center of each control point from the pixel contrast values and a standard deviation is also attached to each control point in the CENTROID_CP_TestXX file produced.

The following commands will load and draw from a file of x and y coordinates of control points called CPXY.mat which will then be identified on a photo, chosen by the user when prompted, with a diameter of the control point (40) and radius of the zone of exclusion (60) (Figure 66).

```
load('CPXY.mat')  
  
geoCENTROID_RG(CP_XY, 'TestXX', 60, 40)
```

This produces a MESH_CP_TestXX.txt file that is used when creating the mesh for the correction of lense distortion and camera movements between images as well as a CENTROID_CP_TestXX.txt file.

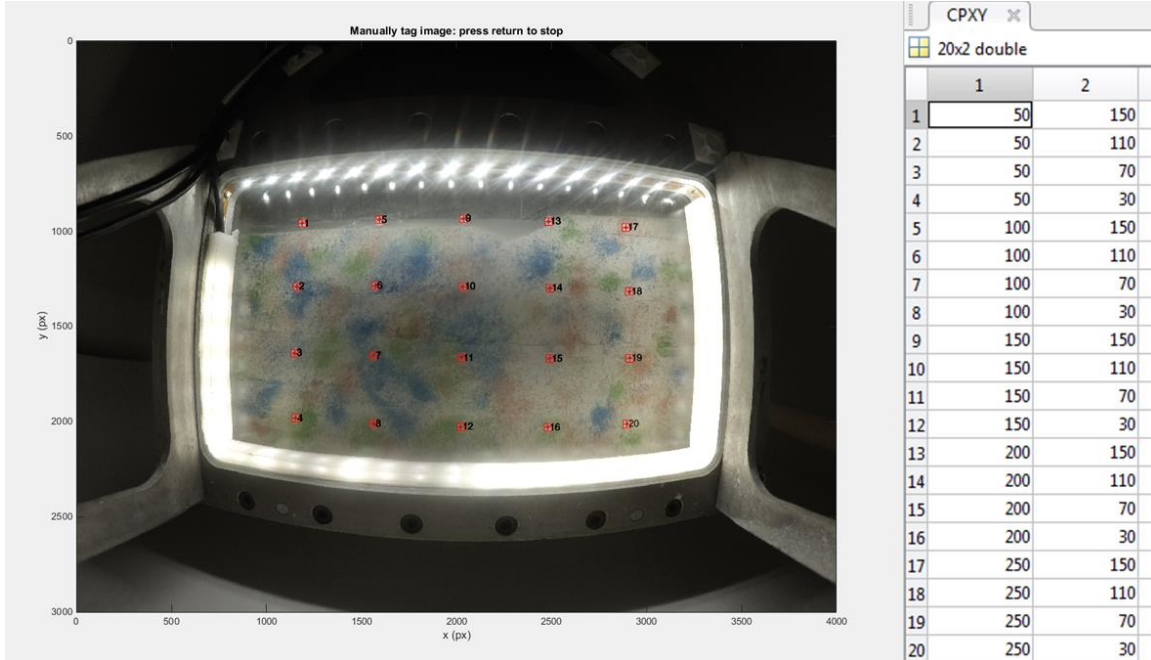


Figure 66 Control Points

The “**geOMESH_RG**” subroutine prompts the user to select a region of interest (ROI) (Figure 67), which is automatically divided into square patches covering the ROI. It also allows for the control points to be automatically selected from the **CENTROID_CP_TestXX.txt** file that was created in the previous step.

The subroutine generates a **MESH_TestXX.txt** file that contains the coordinates of each patch and information about the image for each patch as well as a **RoI_TestXX.jpg** (Figure 68) that shows the region of interest (RoI) selected by the user.

geOMESH_RG('TestXX',100,100)

The above command produces a mesh of 100x100 pixel patches covering the ROI, spaced 100pixels apart in both the u and v axis.

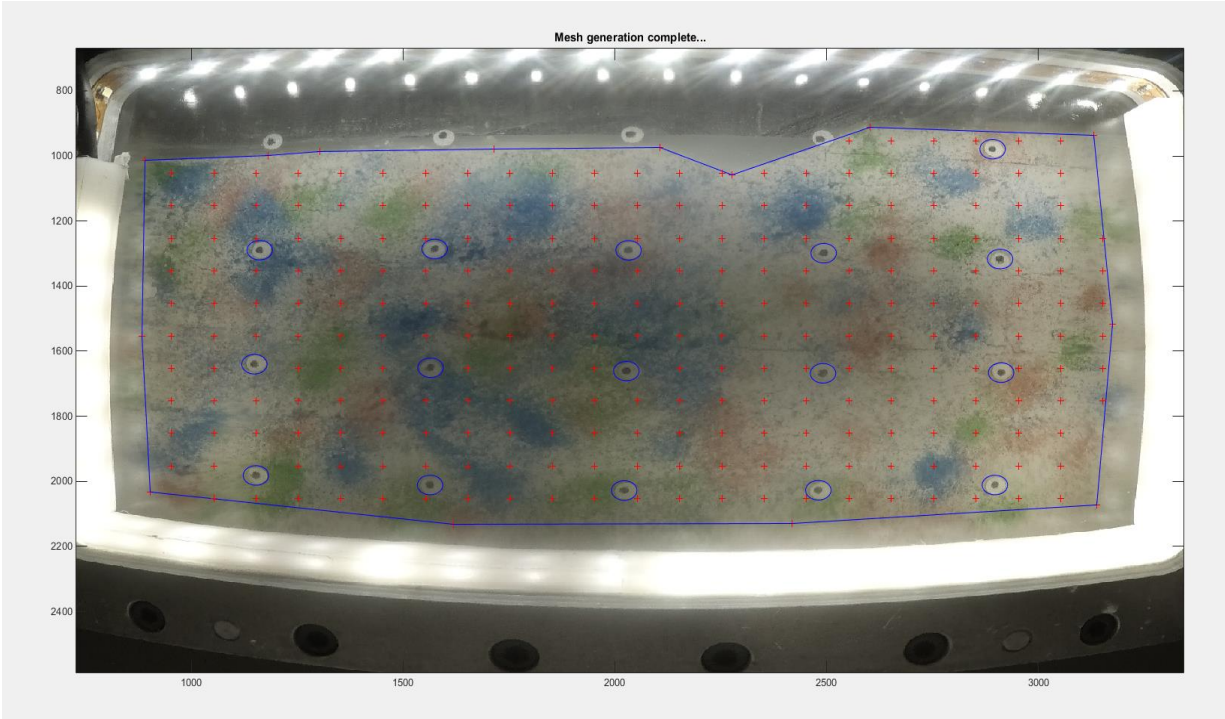


Figure 67 Region of Interest Selected by User with Control Points and Patch Centers

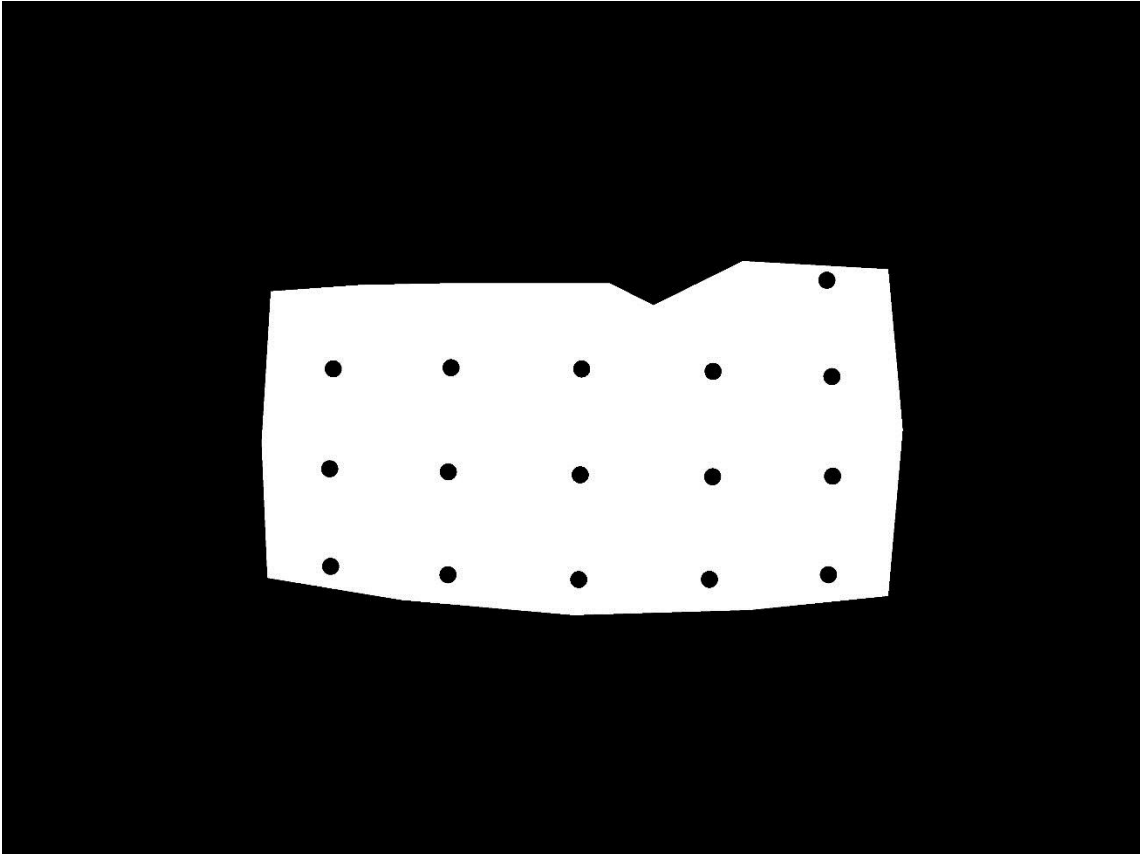


Figure 68 Region of Interest .jpg File Produced by the Subroutine

D.3 Preparation of Launch File

Two launch files are prepared using the “**geoLAUNCH_RG**” command. The first is for the correlation analysis ('**CP_TestXX_analysis_launcher**') and the second is for the PIV displacement analysis ('**TestXX_analysis_launcher**'). The command produces a file that gives the information for the program to complete the analysis, including: Start and end images, step between images, mesh name, produced file name prefix, preface to image files, type of file, type of analysis, and tolerances for shape function difference vectors, number of computation cycles, and patch and full field correlations. Typical starting values suggested by Stanier, et al. (2005) are given in the examples below. Figure 69 shows a typical PIV displacement analysis launch file produced using this subroutine.

This subroutine produces a file for an analysis of every Nth photo according to the mesh described below. The file format used was .jpg and a “leapfrog” analysis was chosen for the PIV displacement. This leapfrog analysis compares each photo with the first photo, giving incremental displacements between photos. A limit of 50 Gauss-Newton iterations was set with an 80% tolerance for the seed and 65% for the full field correlations. This ensured that minor variations in individual patch makeup would not cause errors in the full analysis. If the

tolerances are violated the subroutine will attempt to select a more recent image from which to compare the current image, reducing the leapfrog step.

For the control point analysis the “point to point” analysis is conducted which is more precise for distinct single point analysis as is the case with the control points.

```
geoLAUNCH_RG(12345,56789,1,5,'CP_TestXX','TestXX','G00',  
'jpg',1,1e-5,10,0.9,0.75)
```

```
geoPIV_RG_run('CP_TestXX_analysis_launcher')
```

```
geoLAUNCH_RG(12345,56789,1,5,'TestXX','TestXX','G00',  
'jpg',2,1e-5,50,0.9,0.75)
```

```
geoPIV_RG_run('TestXX_analysis_launcher')
```

```
1 % geoLAUNCH_RG, October 2014, written by Sam Stanier, UWA  
2 % Project: TestXX  
3 % Task: Analysis  
4  
5 % Files containing mesh or region of interest information  
6 MESH_TestXX.txt 0  
7 RoI_TestXX.jpg 0  
8  
9 % Analysis input parameters  
10 analysis_mode 2  
11 cutoff_diffnorm 1e-05  
12 cutoff_iteration 50  
13 seed_zncc_tol 0.9  
14 min_zncc_tol 0.75  
15  
16 % Plots of analysis process  
17 shows_plot_norm_corrcoef 0  
18 show_surf_corrcoef 0  
19 show_dx_disp_hist 0  
20 show_dx_subpx_disp_hist 0  
21 show_dy_disp_hist 0  
22 show_dy_subpx_disp_hist 0  
23 show_quiver 0  
24 show_surf_dx 0  
25 show_surf_dy 0  
26 show_surf_dr 0  
27  
28 % Data path for analysis  
29 \analysis\ 0  
30  
31 % List of images to be analysed  
32 G0012345.JPG  
33 G0012346.JPG  
34 ...  
35 G0056789.JPG  
36
```

Figure 69 Typical geoLAUNCH_RG File

The “**geoLAUNCH_RG**” command (which can either be composed with the launch file name or if none is included will prompt selection of a launch file) conducts the PIV analysis according to the selected launch file. For the control point analysis an M1_data.mat file is produced and for the displacement analysis an M2_data.mat file is produced. These consist of fields of uv locations and coefficient of correlation (cc) matrixes for each control point or patch for each image step. For an analysis of 100 photos with 20 control points the mesh

would be 20x100x3. For an analysis of 100 photos with 200 patches the mesh would be 200x100x3. The number of photos for both analyses must be the same for the control point calibration.

D.4 Control Point Calibration

The “**geoCALIBRATE_RG**” subroutine correlates the uv data produced in the M2_data.mat file (loaded into MATLAB’s workspace and renamed “TestXX_uvdata”) with the displacements for each control point in the M1_data.mat file and the relationship between control point locations in uv space (pixels) vs xy space (mm) contained in the CENTROID_CP_TestXX.txt file. The final product is a horizontal (x) and vertical (y) displacement for each patch between subsequent pairs of photos in a new TestXX_XYdata.mat file in MATLAB’s workspace.

```
load('M2_data.mat')

TestXX_uvdata=data

TestXX_XYdata=geoCALIBRATE_RG(TestXX_uvdata)
```

D.5 Data Manipulation

The data can now be looked at in uv space or xy space. The following six commands select the portions of the matrix which correspond to u or x displacements, v or y displacements, and cc. Note that the cc data will be the same whether produced from uv or xy data. These can be copied to excel and the individual values for each step and patch are given.

```
TestXX_uvdata=TestXX_UVdata(:, :, 1)
TestXX_vdata=TestXX_UVdata(:, :, 2)
TestXX_ccdata=TestXX_UVdata(:, :, 3)

TestXX_xdata=TestXX_xydata(:, :, 1)
TestXX_ydata=TestXX_XYdata(:, :, 2)
TestXX_ccdata=TestXX_XYdata(:, :, 3)
```

PIV has built in subroutine, “**geoPLOTDISP_RG**”, to produce graphs of displacements in vectors, contours, or surfaces from either the uv or xy data for specific ranges of images. The “**geoPLOTDISP_RG_help**” file provides more detail on the subroutine inputs.

```
geoPLOTDISP_RG(TestXX_UVdata, frame1, frame2, x_offset, y_offset, mode, colour, plot_type)
```

A strain matrix can be produced from the uv or xy data using the “**geoSTRAIN_RG**” subroutine as seen in the commands below. These matrixes, like the displacement data, can use the “**geoPLOTSTRAIN_RG**” subroutine to plot various figures showing various types of strain between the image steps selected. The “**geoSTRAIN_RG_help**” and “**geoPLOTSTRAIN_RG_help**” files provide more detail on the subroutine inputs, and types of strain data contained in the matrix.

```
TestXX_UVstrains=geoSTRAIN_RG(TestXX_UVdata)
TestXX_XYstrains=geoSTRAIN_RG(TestXX_XYdata)
```

```
geoPLOTSTRAIN_RG(TestXX_XYstrains,frame1,frame2,x_offset,y_offset,mode,component,plot_type)
```

Appendix D

Shrinkage Curve for Soil Mixture

Two methods were used to produce an estimated shrinkage curve for the expansive soil mixture (90% Speswhite Kaolin/10% MX-80 Bentonite). The first method (Fredlund et al., 2011) periodically measures the volume and mass of a cylindrical soil sample, mixed to its liquid limit and allowed to air dry. Figure 70 shows the Measured Shrinkage Curve. It provides a description of the shape of the shrinkage curve in addition to the shrinkage limit. The second method (ASTM D4943-08) provides initial saturated densities and final dry densities for six soil samples. These are plotted as Wax Method Shrinkage and confirm the first method's results. The Target Compacted Soil Mixture is also plotted for reference.

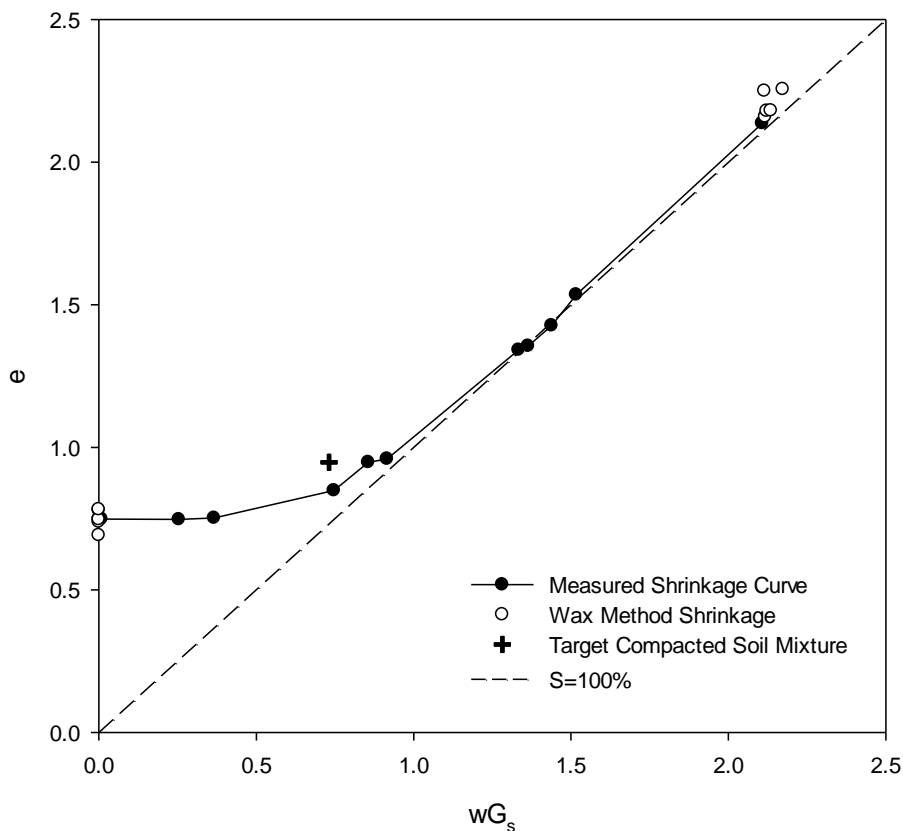


Figure 70 Shrinkage Curve for Soil Mixture

Appendix E

**Verification of physical modelling with a geotechnical centrifuge
using physical models of slope stability and bearing capacity.**

*In: Proceedings of the 69th Annual Canadian Geotechnical
Conference.*

Verification of physical modelling with a geotechnical centrifuge using physical models of slope stability and bearing capacity

John Kingswood, Stephen LaPorte, & Greg Siemens
GeoEngineering Centre at Queen's-RMC
Department of Civil Engineering – Royal Military College of Canada,
Kingston, Ontario, Canada, K7K 7B4



GEOVANCOUVER
— 2016 —

ABSTRACT

The Royal Military College of Canada has recently acquired a 1.5m-diameter, 9 G-ton geotechnical beam centrifuge. It has a maximum operating acceleration of 300g and is capable of carrying two payload cradles. It will be used for both physical modelling research and as a teaching tool. In order to have confidence in the scaling relations and to produce sound laboratory procedures for the equipment, two verification test programs are conducted. First, a slope stability model; varying scale, shear strength, and slope geometry, is tested and correlated with Taylor stability numbers. Second, a strip footing is modelled and compared with analytical solutions. Correlation between the physical models at different scales and the expected analytical results are examined in order to iteratively verify the test results, improve accuracy of modelling, and refine procedure for future physical modelling.

RÉSUMÉ

Le Collège militaire royal du Canada a récemment acquis une centrifugeuse de 1.5m de diamètre pesant 9 gigatonnes. Elle a une accélération maximale de 300g et est capable de transporter deux nacelles. Elle sera à la fois utilisée en recherche sur les modèles physiques et comme outil d'enseignement. Afin de développer une confiance dans les relations de similitudes, d'une part, et une procédure de laboratoire fiable dans l'utilisation des équipements, d'autre part, deux tests de contrôle sont effectués. Le premier, un modèle de stabilité de pente à différentes tailles, valeurs de la résistance au cisaillement et géométries de la pente, est testé et la corrélation avec le nombre de Taylor est étudiée. Le deuxième test, la rupture d'une semelle de fondation, en utilisant une méthode similaire au premier test est effectuée. Les résultats obtenus sont comparés aux solutions analytiques. Les corrélations entre les modèles physiques à différentes échelles et les résultats analytiques attendus sont examinés afin de calibrer de manière itérative les tests, améliorer la précision de la modélisation, et d'affiner la procédure de l'utilisation de la centrifugeuse.

1 INTRODUCTION

Physical modelling in a centrifuge allows for examination of geotechnical structures at elevated g-levels. Centrifuge models are commonly used in geotechnical engineering research and teaching to model shallow and deep foundations, slopes, retaining walls, and soil-structure interaction applications (Madabhushi 2015). The Geotechnical Engineering Group at Royal Military College of Canada recently acquired a 1.5m diameter, 9G-ton geotechnical beam centrifuge (Figure 1) that can apply 300g acceleration to two physical models simultaneously. The maximum size of physical models are 300x180x100mm (width x height x depth) corresponding to a maximum prototype size of 90x54x30m. Prior to conducting research and teaching exercises utilizing the centrifuge, the procedures, scaling and results must be verified to ensure accurate results that demonstrate the principles of physical modelling. The method used to establish the centrifuge to be useful to model soils is the modelling of models (Madabhushi, 2015). This method can confirm that the RMCC centrifuge is operating as expected in applying accepted scaling laws in an accurate manner. This, in turn, allows for an accurate description of the behaviour of prototypes through centrifugal modelling. Modelling of models is a technique for testing two or more physical models for a common prototype. The prototype

model is constructed at two different scales and tested at scale forces that model the same structure (Madabhushi, 2015). If the behaviour of the two models correspond to one another as well as to the expected behavior of the prototype the results substantiate the scaling laws and methods used. They can then be applied to new areas of research and testing. Modelling of models is typically performed in new physical modelling exercises to confirm the scaling laws are applied correctly and modelled behaviour agrees with accepted theory. In beam centrifuges of relatively small diameter modelling of models presents challenges, including variation in the gravity field, which must be considered during interpretation of results.

In this paper two types of prototype structures were considered; firstly, a clay slope brought to a factor of safety (FoS) of 1.0 under undrained conditions and secondly a shallow foundation constructed on clay to the same FoS. The prototype structures' expected behaviours were compared with accepted analytical models. The slope stability models were compared with Taylor charts (Taylor, 1948) stability numbers. The shallow foundation models were compared with Terzaghi's (1967) bearing capacity equation. The digital imagery data for each model was analyzed using particle image velocimetry (PIV) (Stanier, et al., 2015), to determine the failure and the corresponding scaling forces applied. This in turn was

compared with the predicted prototype behaviour and with other scaled models. The degree of agreement was then evaluated.

2 RMCC BEAM CENTRIFUGE SCALING LAWS AND GRAVITY FIELD

2.1 Scaling Laws

Converting prototypes to physical models requires understanding of scaling laws and the gravity field which both vary as a function of the rotational velocity of the centrifuge and radius of the body in motion. Equation 1 describes the relationship between the force applied to the sample within the cradle (N_g) as a function of the radius (r) and due the angular velocity ($\dot{\theta}$) (Madabhushi, 2015).

$$N_g = r \dot{\theta}^2 \quad [1]$$

One dimensional properties such as length are modeled in relation to the prototype as $1/N$, two dimensional properties such as area are scaled as $1/N^2$, and the three dimensional properties such as mass and volume as $1/N^3$ (Madabhushi, 2015). The dimensions of the centrifuge cradles are 180x300x100mm (height, y , width, x , depth, y) which, assuming a material unit weight of approximately 17kN/m^3 , allows the centrifuge to model prototypes of dimensions 54x30x90m, volume of $145,800\text{ m}^3$, and weight of 252.7 tonnes.

Despite its relatively small size (Figure 1) the centrifuge allows for a variety of testing. Table 1 provides the basic operating limits of the centrifuge.

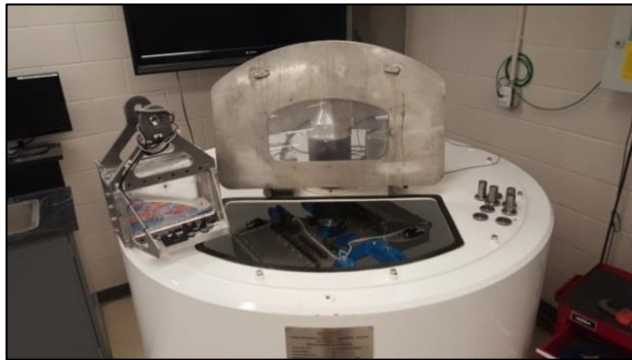


Figure 1 Broadbent Geotechnical Beam Centrifuge

Table 1. Operating Parameters (Broadbent, 2015)

| | |
|--------------------------|---------|
| Maximum rotational speed | 638 rpm |
| Maximum N^1 | 300^2 |
| Maximum payload | 90 kN |

¹ N is the ratio of the acc. relative to the acc. of gravity (9.81m/s^2)
²at 0.660 m radius

2.2 Gravity Field

Based on its physical dimensions, experiments conducted within the RMCC centrifuge require consideration of the variation in the gravity field over the depth of models. The

implication of the variation in the gravity field is developed based on relations for scaling models. The acceleration is relative to the effective radius and the sample's height is a significant percentage, 27%, of the effective radius and so the applied acceleration varies, at the maximum rotational speed, by 13% below and above the predicted value for the effective radius at the top and bottom of a 180mm model (Figure 2). As a result of this variation the calibration methods must employ methodology to consider the effect of effective radius on the results.

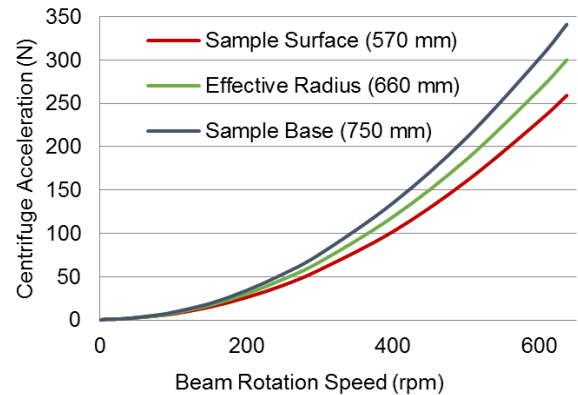


Figure 2 Gravity field as a result of changes in radius

3 CALIBRATION PHYSICAL MODEL METHODS

3.1 Slope Stability

Slope failure is a common and well known problem in geotechnical engineering. As a result its mechanics are well understood and provide an ideal structure to employ the modelling of models using a simple slope stability problem as the prototype.

3.1.1 Theory

Taylor Charts (Figure 3) are a method of determining the factor of safety (FoS) for simple undrained slopes of homogenous composition (Taylor, 1948).

A stability number (N_o) is a function of (Equation 2) the unit weight (γ), height of slope (H), and cohesion (c).

$$N_o = \frac{\gamma H}{c} \quad [2]$$

By calculating N_o , the allowable slope angle (i) at a F_s of 1.0 can then be read off of the chart for the appropriate slope failure geometry whether toe, deep, or slope.

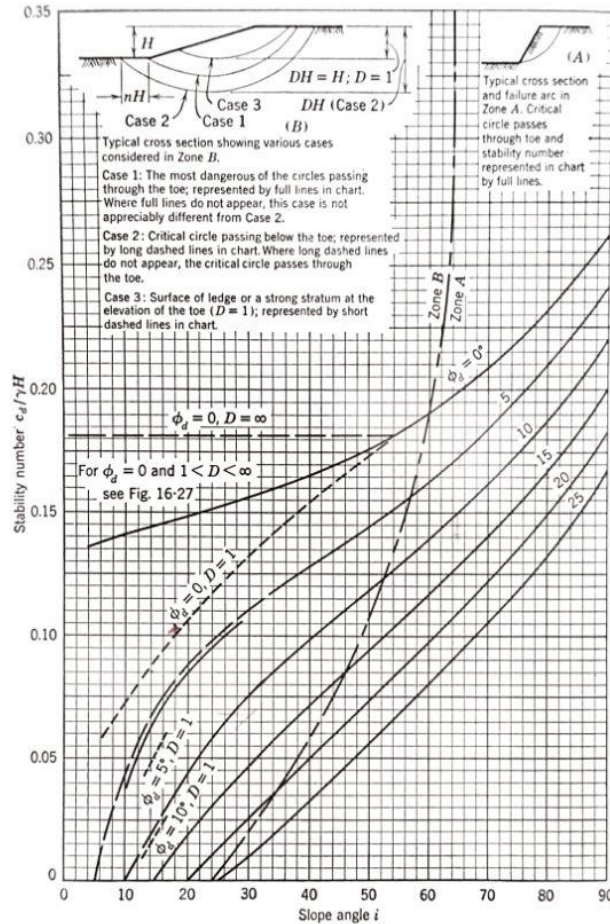


Figure 3 Taylor chart (Taylor, 1948)

3.1.2 Methodology

The physical model geometry was selected in order to achieve a 40° slope with a 150mm height, a 50mm standoff from the cradle's right boundary, and a 71mm run-out for the failure. An example physical model prior to testing is shown in Figure 4. The second model of models was selected at 2/3 proportion at 100mm height, 50mm standoff, and 131mm run-out.

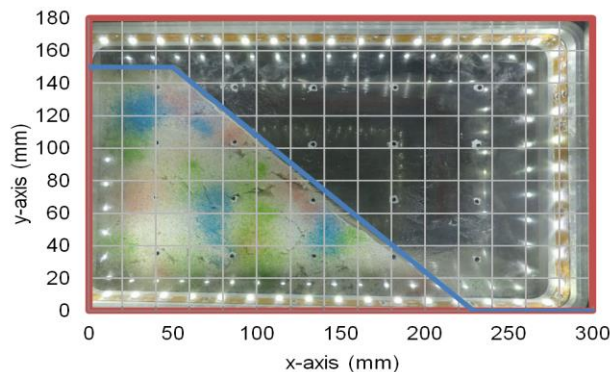


Figure 4 Slope geometry within centrifuge cradle for 150mm 40° slope

Using Equation 2, (Figure 3), and the previously mentioned geometry, the relationship between N_g and c was determined. In order to vary the kaolin material was mixed to a water content (w) with an associated estimated undrained c (Table 2).

Table 2. Slope Stability at 40°

| H (mm) | w (%) | Predicted c (kPa) | Predicted N_{failure} |
|--------|-------|---------------------|--------------------------------|
| 150 | 37.7 | 69 | 77 |
| 100 | 37.4 | 108 | 115 |
| 150 | 36.5 | 82 | 89 |
| 100 | 36.8 | 119 | 134 |
| 150 | 35.3 | 97 | 99 |
| 100 | 35.0 | 149 | 149 |

Unit weight of the soil was calculated from the theoretical density of the kaolin mix at each water content and confirmed by taking the mass of the model once constructed. From these values a predicted N_g for failure was calculated.

Kaolin clay mixed to the desired water content was compacted in lifts over the base plates in a box with the same dimensions as the interior of the cradle and cut to the required dimensions. The side of the cradle was removed and the model placed inside the cradle and side reattached ensuring the interface with the sides was well greased.

The model was placed in the centrifuge and experiments were recorded with GoPro HERO 4 HD digital cameras at a time-lapse of one frame per second. The centrifuge was set to a rapid stepped increase in rpm to the failure gravity level while noting the corresponding photo number and elapsed time for later evaluation of rpm at failure. Owing to the variation in the gravity field, the nominal N value for the centrifuge was adjusted to apply the actual N to the center of mass of the slope.

3.2 Bearing Capacity

The second prototype structure type selected to be modelled was a shallow foundation. This geotechnical structure is also well studied and the mechanics described by Terzaghi's (1967) bearing capacity equation. In order to be able to best observe the behaviour in the centrifuge, a strip footing with a theoretically infinite length was chosen for the verification tests.

3.2.1 Theory

Terzaghi's strip footing bearing capacity equation (Equation 3) describes the three components of bearing capacity (q). The first term is related to the soil's cohesion (c) and friction, the second to the stress from material above the foundation's applied load, and the third is related to the mass of the soil as a function of unit weight (γ).

$$q = cN_c + \gamma D_f N_q + \frac{1}{2} \gamma B N_\gamma \quad [3]$$

By loading the soil rapidly and placing the applied load at the surface of the soil the equation's second and third terms equal zero as N_y equals zero when the friction angle of the soil is zero and the second term goes to zero as D_f equals zero leaving the bearing capacity for undrained loading a function of c and the factor N_c which is constant at $2+\pi$. Thus the solution is well constrained as the applied g -level applies the vertical stress as a function of the initial mass of the strip foundation.

3.2.2 Methodology

The physical model was selected to capture the predicted behaviour. The model geometry was chosen in order to achieve a depth of at least two times the width of the 60mm strip footing width (B) to a 120mm depth, and 100mm long and a second smaller model at 1/2 the footing with ($B=30$ mm) at 60mm, 100mm respectively (Figure 5).

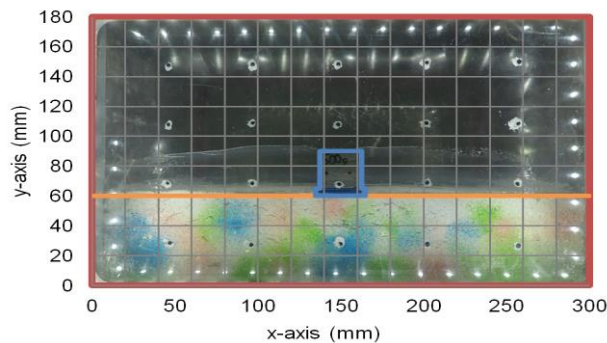


Figure 5 Footing geometry within centrifuge cradle for 30mm/500g footing

The experimental profile evaluated variations in the undrained shear strength of the foundation soil on the bearing capacity. Using Equation 3 and, as was done previously, by varying c by mixed to a known water content (w) with an associated estimated c (Table 3) the bearing capacity of the soil could be estimated. The applied load was known from the mass of the steel block (with the added mass to PLA 3D printed plastic footing) and the area of the footing. The applied load and the calculated bearing capacity at a FoS of 1.0 produced an N_g for failure.

Table 3 Strip Footing Bearing Capacity

| B (mm) | w (%) | Predicted c (kPa) | Predicted $N_{failure}$ |
|--------|-------|---------------------|-------------------------|
| 60 | 33.9 | 49 | 79 |
| 30 | 34.9 | 41 | 158 |
| 60 | 32.6 | 51 | 70 |
| 30 | 32.9 | 49 | 140 |
| 60 | 34.5 | 42 | 79 |
| 30 | 34.6 | 42 | 158 |

The same method of model construction and data collection was used as was done previously with the slope stability model.

Because the interface between the base of the footing and clay does not fall on the effective radius of the centrifuge the nominal N value for the centrifuge was adjusted to apply the predicted N to the surface of the clay sample.

3.2.3 Boundary Conditions

The boundary conditions of the soil specimen were fixed along the x and z axis by the side walls and Perspex observation window of the cradle. On the y axis the specimen was free at the surface and bound at the bottom of the cradle.

Silicon grease was used to reduce friction along the acrylic perspex to allow the soil to move freely along these surfaces. However, friction was increased along the bottom of the aluminium cradle to ensure the failure plane did not occur at the aluminium-soil interface. This was done by using serrated PLA 3D printed plates inserted at the bottom of the soil model. Figure 6 shows the effectiveness of using the friction plates. For the model using a soil-aluminium interface (Figure 6A) the failure surface impacts the boundary, which makes the model's failure mechanism invalid for the predicted failure. The slope model, which incorporates the frictional interface (Figure 6b) shows the failure surface located 2-3 cm above the base. Thus the boundary conditions were not impacting the physical model results. Both slope stability and bearing capacity experiments reported in this paper used the frictional interface.

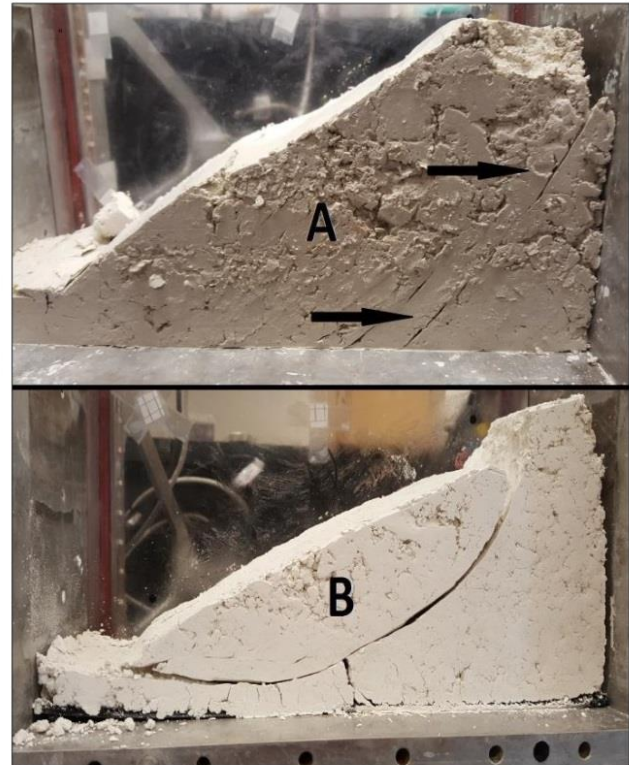


Figure 6 Effect of base friction insert plates; A – failure plane without plates, B – failure plane with plates.

| Predicted τ (kPa) |
|------------------------|
| 05 |
| 05 |
| 15 |
| 15 |
| 5 |
| 5 |

For the bearing capacity model, the depth of twice the width of the footing ensured that the failure surface was well removed from the lower fixed boundary. The width of the soil model relative to the width of the applied footing allowed for the failure surface to occur to either side of the footing without interference from the walls of the cradle.

4 ANALYSIS

4.1 Slope Stability

Undrained slope stability experiments were performed by constructing slope models at reduced scale and subjecting them to elevated g-levels until failure. The three pairs of tests were analyzed with PIV to establish the g-level at failure. Time-lapse digital imagery gathered of the models during testing was processed to identify the formation of shear surfaces. A typical test was analyzed using the following method. Firstly, for a 150mm slope, several patches (yellow boxes on Figures 7 and 8) were selected, which included some in the stable portion of the slope and others in the active segment of the slope failure. The output from PIV gives displacement of each patch in digital pixels. By plotting the displacement of patches versus g-level, the conditions at failure are interpreted.

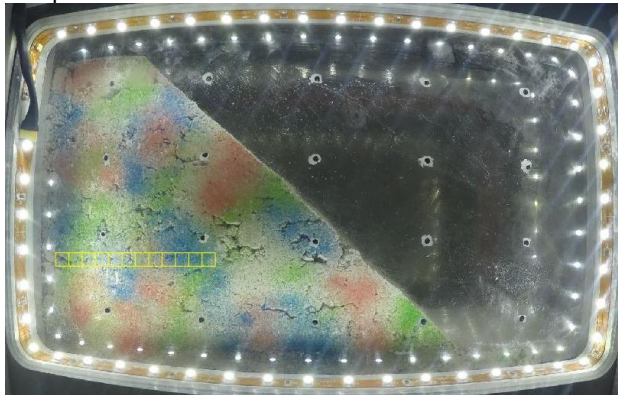


Figure 7 Patches for slope stability analysis

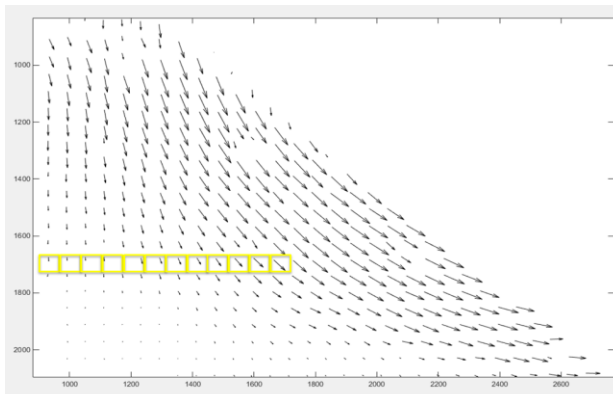


Figure 8 Patches for analysis over PIV displacement vectors

The analysis consists of correlating the N-path path (Figure 9) to the digital image history and plotting patch

displacement versus N-level. During centrifuge spin-up, settlement of the soil mass is anticipated due to elevated g-level. At incipient failure, the landslide is formed and the failure zone will accelerate and displace relative to soil within the stable zone. Displacement of two of the patches, one in the stable and one in the failed portion of the slope, is plotted in Figure 10. At N-levels less than 100, both patches move downward due to the increasing gravity field. As N-level is raised to greater than the 100, the patch inside the failure zone moves at an increasing rate. By fitting a line to the linear portion of the displacement versus N graph, the point of failure is interpreted. Comparison between patches located within the stable portion of the slope and the failure zone allows for isolation of settlements due to increased gravity field and shearing due to formation of the landslide. Thus the gravity level at failure is interpreted as 100 for this test and, once the gravity field correction is applied to it, is given the notation $N_{failure}$.

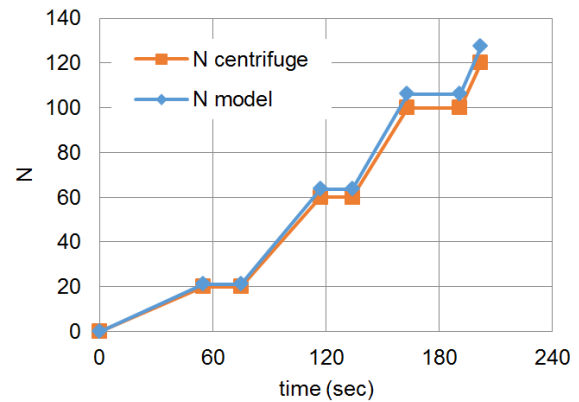


Figure 9 N-path during slope stability test

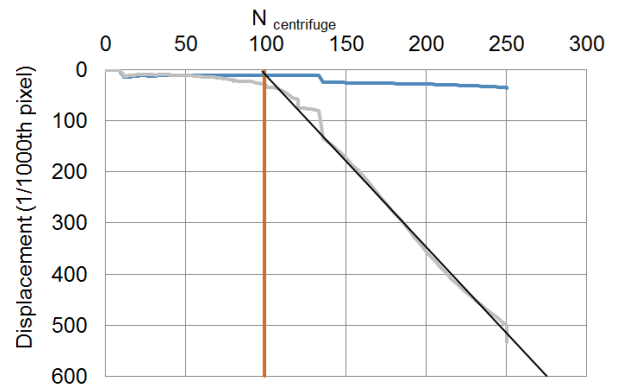


Figure 10 Patch displacement vs time with location of failure

A total of six undrained landslide experiments were performed with varied heights, compaction water content, and associated undrained shear strength. Experiments were analyzed in a similar manner as described here and Table 4 lists the observed gravity level at failure ($N_{failure}$) for each test.

Table 4 Summary of slope stability tests results

| H (mm) | w (%) | Observed $N_{failure}$ |
|--------|-------|------------------------|
|--------|-------|------------------------|

| | | |
|-----|------|-----|
| 150 | 37.7 | 73 |
| 100 | 37.4 | 108 |
| 150 | 36.5 | 83 |
| 100 | 36.8 | 115 |
| 150 | 35.3 | 111 |
| 100 | 35.0 | 154 |

4.2 Bearing Capacity

The bearing capacity tests were conducted with a similar method to the slope stability with some variation to accommodate the differences in the anticipated failure mechanism. An example model with a 60mm wide and mass=2000g shallow footing placed at the surface is shown in Figure 11 and a typical PIV analysis at failure is shown in Figure 12. Firstly, method for a typical test selected the patch mesh for a strip footing (Figure 11, 12). The mesh included patches both under the footing and adjacent to the footing.

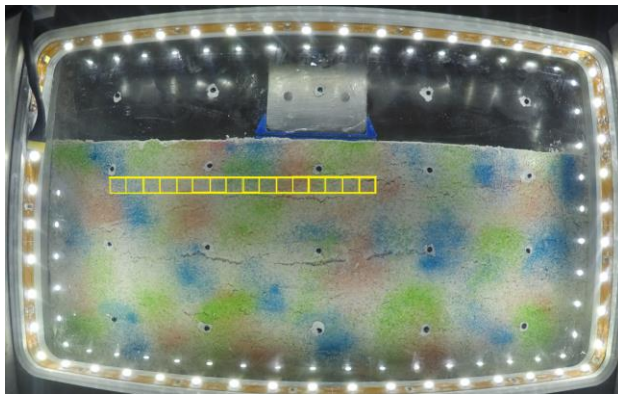


Figure 11 Patches for bearing capacity analysis

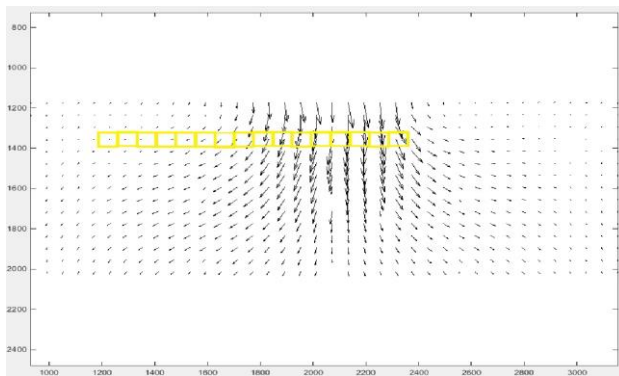


Figure 12 Patches for analysis over PIV displacement vectors

The g-level was increased throughout the test as plotted in Figure 13 for both the centrifuge nominal N and the N for the model (at the interface between the foundation and the soil). Two patches were selected; one under the footing and another in the adjacent shear zone. These patches were selected as they were anticipated to show differing movements during spinup and failure. The patch underneath the footing shows settlement and failure in as

the foundation sinks into the clay. The patch in the adjacent failure zone shows an initial settlement followed by an uplift caused by the displaced soil under the footing. The patches' relative displacement as a function of the applied N (Figure 14) allowed for the identification of N at failure.

The criteria for N of failure were the change in the rate of settlement for the first patch and the change in the direction of displacement (uplift vs. settlement) for the second patch. This N, when corrected for distance from nominal g-field, was taken as the $N_{failure}$.

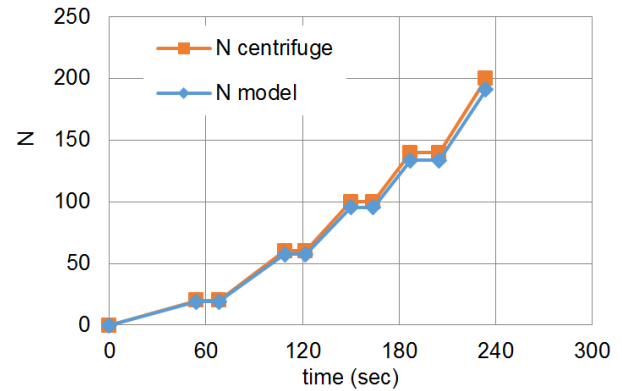


Figure 13 N-path during bearing capacity test

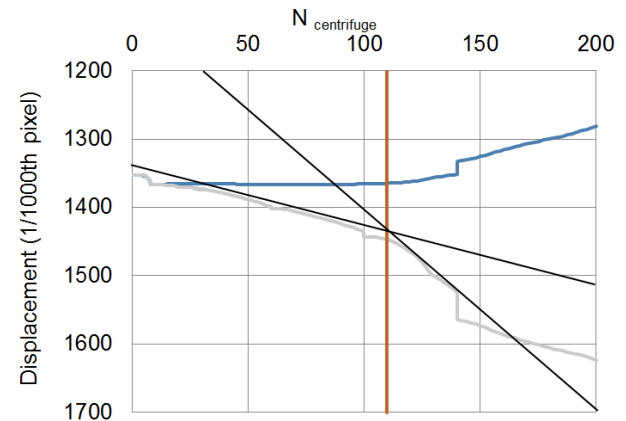


Figure 14 Patch displacement vs time with location of failure

Table 5 Summary of bearing capacity test results

| B (mm) | w (%) | Observed $N_{failure}$ |
|--------|-------|------------------------|
| 60 | 33.9 | 78 |
| 30 | 34.9 | 164 |
| 60 | 32.6 | 110 |
| 30 | 32.9 | 176 |
| 60 | 34.5 | 67 |
| 30 | 34.6 | 177 |

A total of six bearing capacity experiments were completed and summarized in Table 5. The experimental variables included footing width, compaction water

content and associated undrained shear strength. Table 5 shows the compiled data for the tests.

5 RESULTS

The data obtained for each prototype test series was evaluated in two ways. Firstly, the correlation between the two models and the ability to conduct the modelling of models was determined, and secondly the correlation with the analytical predictions using the respective theories for each prototypes behaviour was ascertained.

5.1 Slope Stability

Figure 15 shows the relationship between the 150mm and 100mm slope models. Based on the geometry of the models a ratio of N at failure for the 100 mm slope and 150 mm slope is theoretically 1.5. Therefore the comparative results shown in Figure 15 are accompanied by a 1:1.5 for theoretical comparison. The results compare within an average of 6% of the theoretical ratio.

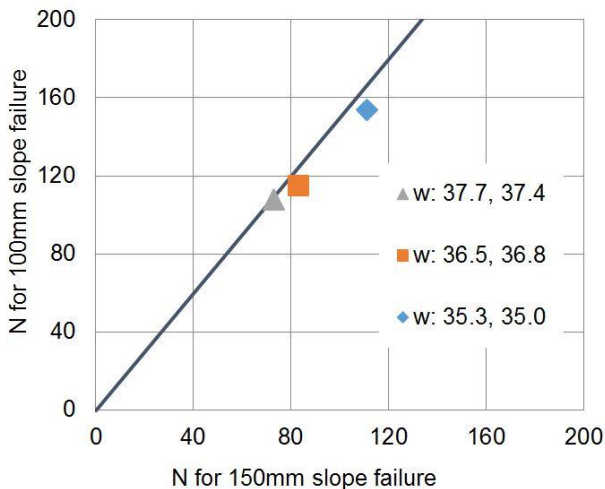


Figure 15 Slope stability modelling of models correlation

A second test is performed by comparing the data to an analytical model, which is the Taylor chart. Figure 16 plots the N observed at failure to the theoretical value. Also on the figure is a 1:1 line on which all data points should plot. The closed symbols are the 150mm slopes and the open symbols are the corresponding 100 mm tall slopes. Comparing the data to the 1:1 line shows the failures corresponded within an average range of 4% of the predicted values.

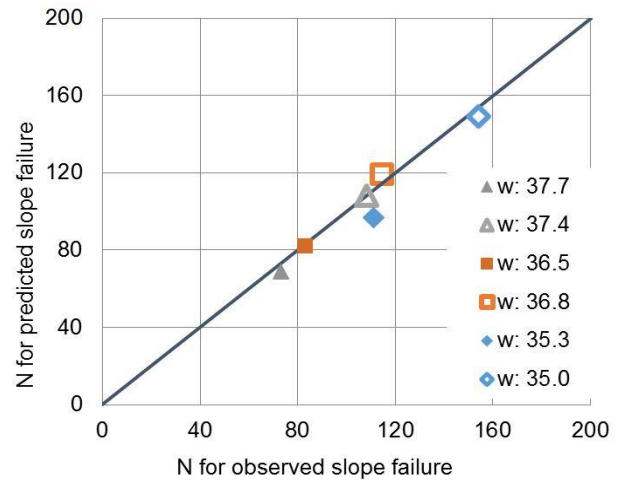


Figure 16 Observed slope stability correlation with theoretical prediction

5.2 Bearing Capacity

Figure 17 shows the correlation of $N_{failure}$ between the pairs of tests for both the $B=60mm$ ($m=2000g$) and $B=30mm$ ($m=500g$) models. Also on the figure is the theoretical line which is formed base on the geometry of the two experiments. A 1:2 ratio between the $B=30mm$ and $B=60mm$ is anticipated for models constructed at the same water content. The model of models results differ from the theory by an average of 16% for the bearing capacity test series, however, most of the difference is due to the differing water contents noted in Table 5. Kaolin's undrained shear strength changes 4.4 kPa (according to shear vane tests done) for every 1% of moisture content. Considering the differing moisture contents the model of models was considered successful.

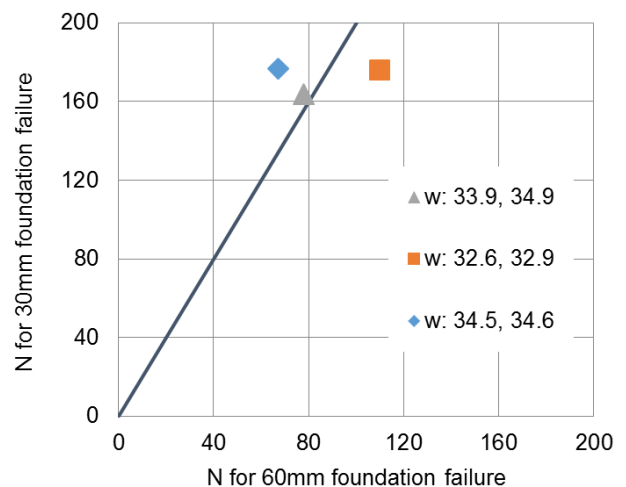


Figure 17 Bearing capacity modelling of models correlation

A better comparison in this case is to compare the failure g-level to the theoretical value given by Terzaghi's equation. Figure 18 plots the observed N-level at failure to the theoretical value with both 60mm footings (closed

symbols) and 30 mm footings (open symbols) shown. In this way, the physical model data only differs by an average of 10%.

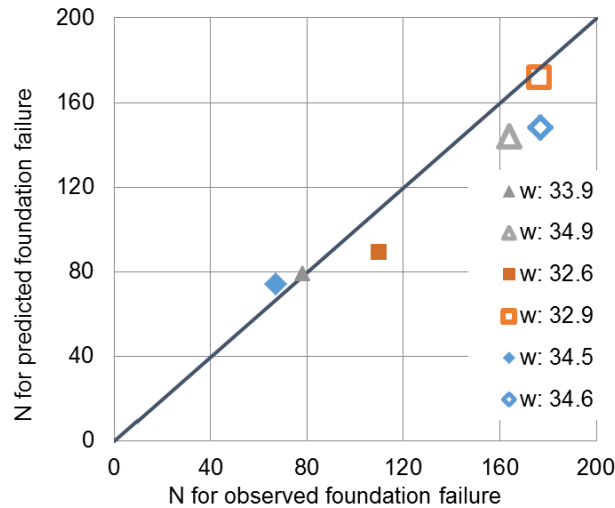


Figure 18 Observed bearing capacity correlation with theoretical prediction

The variation in the observed N at failure is likely a result in inconsistent behaviour of the foundations during failure. Variable rotation of the footing during the failure mechanism produced variation in the expected results.

6 CONCLUSION

The results obtained by modelling prototypes with two different scales to obtain proportional results demonstrates the desired ability to properly scale models. Both the slopes and the shallow foundations were able to be scaled using the techniques described produced consistent data in accordance with the scaling laws.

The models' behaviour was also consistent with the predicted analytical methods for both Taylor's slope stability charts and Terzaghi's bearing capacity equation.

These results produced confidence in the ability to not only scale between models but also to achieve modelling of prototypes using known analytical methods.

Any variations in the slope stability results were largely attributable to inconsistency in sample preparation and model construction. The sample soil was mixed and compacted in separate batches for each model. This produced some variation in the correlation between models.

In order to mitigate these variations in soil composition carefully calibrated soil samples that are prepared in consolidation boxes to the desired water contents will ensure consistent, precise, and accurate results.

The larger variations in the bearing capacity tests indicate that a new method for tests with similar geometry should be employed. For tests that are sensitive to variations in modes of failure the use of actuators to apply loads and improve repeatability of failure mechanics and results.

The described methods and results confirm RMCC's ability to employ this centrifuge in both teaching and

research. Knowledge gained in methodology and lessons learned from analysis of the results will continue to improve the accuracy of the testing methods to produce high quality modelling of a variety of geotechnical prototypes. This will improve RMCC's educational scope and range and value of future research projects.

ACKNOWLEDGEMENTS

The writers would like to acknowledge the contributions of the Department of National Defense, specifically 1 Engineer Support Unit and *Natural Sciences and Engineering Research Council* of Canada to the paper.

REFERENCES

- Bowles, J.E. 1968. *Foundation Analysis and Design*, McGraw-Hill, New York, NY, USA.
- Das, B.M. 2016. *Principles of Foundation Engineering*. 8th ed., Cengage Learning, Boston, MA, USA.
- Madabhushi, G. 2015. *Centrifuge Modelling for Civil Engineers*, CRC Press, Boca, Raton, FL, USA.
- Boadbent, Inc. 2015. *Broadbent Operating Manual*, Thomas Broadbent & Sons Ltd., Huddersfield, England.
- Stanier, S.A., Blaber, J., Take, W.A., and White, D.J. 2015. Improved image-based deformation measurement for geotechnical applications. *Canadian Geotechnical Journal*, 53(5): 727-739.
- Taylor, D.W. 1948. *Fundamentals of Soil Mechanics*, John Wiley & Sons, New York, NY, USA.
- Terzaghi, K. and Peck, R.B. 1967. *Soil Mechanics in Engineering Practice*, 2nd ed., John Wiley & Sons, New York, NY, USA.